Winter 2006

Deciphering the Signature of Magma Mixing: Examples from the Castle Creek Eruptive Period, Mount St. Helens, Washington

Seth Taylor Mattos
Central Washington University

DECIPHERING THE SIGNATURE OF MAGMA MIXING: EXAMPLES FROM THE CASTLE CREEK ERUPTIVE PERIOD, MOUNT ST. HELENS, WASHINGTON

A Thesis

Presented to

The Graduate Faculty

Central Washington University

In Partial Fulfillment

of the Requirements for the Degree

Master of Science

Geology

---

by

Seth Taylor Mattos

November 2006

CENTRAL WASHINGTON UNIVERSITY

Graduate Studies

We hereby approve the thesis of

Seth Taylor Mattos

Candidate for the degree of Master of Science

APPROVED FOR THE GRADUATE FACULTY

_____ _____

Dr. Wendy A. Bohrson, Committee Chair

_____ _____

Dr. Paul W.O. Hoskin

_____ _____

Dr. Michael A. Clynne

_____ _____

Associate Vice President of Graduate Studies

ABSTRACT

DECIPHERING THE SIGNATURE OF MAGMA MIXING: EXAMPLES FROM THE CASTLE CREEK ERUPTIVE PERIOD, MOUNT ST. HELENS, WASHINGTON

by

Seth Taylor Mattos

November 2006

Mount St. Helens (MSH) volcano in southwestern Washington has intermittently erupted dacitic products for the last 40,000 years. On limited occasions, the volcano has produced andesite lava flows, and during one short-lived period, basaltic lava flows. This time interval has been termed the Castle Creek eruptive period and occurred between approximately 2500 and 1700 years B.P. The Castle Creek period erupted dacite, andesite and basalt within this short span of time. Andesite and dacite eruptions dominate the first approximately 700 years of the period, and all basaltic units were erupted in approximately the last 100 years of the period. This is the only known occurrence of basaltic eruptive products at MSH, and yet these lava flows were a major contributor to the buildup of the modern stratocone associated with MSH. Three litho-stratigraphic units exist within the basalts of Castle Creek; from youngest to oldest they are Cave basalt, Precave basalt and North Flank basalt. Petrogenetic relations among these units provide insight into the nature of the subjacent magma chamber during Castle Creek time. Presented here are whole-rock major and trace element data compiled from both published and unpublished works, along with 17 new whole rock trace element

analyses and $^{87}Sr/^{86}Sr$ isotopic ratios, plus textural and compositional imaging integrated with feldspar crystal chemistry data collected by electron microprobe. Petrographic and quantitative petrographic analyses were performed on 5 samples of Castle Creek basalt. MELTS closed-system fractional crystallization simulations were also executed to model major element evolution during the Castle Creek eruptive period.

MELTS simulations reveal primitive Cave basalt can be related to most Precave basalts, andesite and dacite compositions of Castle Creek age through isobaric fractional crystallization. Simulations of North Flank basalt evolution reveal fractional crystallization is potentially a contributing process within the basalts but does not likely control North Flank composition. High initial abundances of K_2O and TiO_2 within the North Flank and data trends of those oxides prohibit a strict fractional crystallization relationship. Strontium isotopic compositions reveal fractional crystallization alone is not responsible for variation within the three basalt units, as evidenced by the relatively large range of $^{87}Sr/^{86}Sr$ ratios (approximately 0.7030-0.7034) and increasing $^{87}Sr/^{86}Sr$ with decreasing whole rock MgO contents. Feldspar analyses by electron microprobe reveal maximum plagioclase feldspar core compositions remain at near constant levels (approximately An_{80}) throughout an approximately 2 wt% change in whole rock MgO content. Best-fit MELTS simulations predict equilibrium plagioclase crystallization that occurs over this same interval should produce crystals with lower anorthite content (down to An_{52}). Crystal size distributions (CSD) suggest plagioclase feldspar from basalt samples had maximum average residence times between 30 and 60 years, well within the approximately 100-year timescale of basaltic magmatism at MSH. Low numbers of large phenocrysts among all samples, similar shapes of CSD plots and similar feldspar

compositions all suggest the basalts of Castle Creek time were exposed to a similar thermal regime while plagioclase was a stable phase.

Magmas of the Castle Creek eruptive period of Mount St. Helens were affected by a complex interplay of open-system magmatic processes. Preservation of distinct compositional characteristics between more primitive North Flank and Cave samples (e.g., K_2O) suggests that the magma reservoir system at MSH during Castle Creek time was sufficiently geometrically complex to effectively isolate discreet magma batches. Petrologic evidence, however, suggests interaction among more differentiated samples of all units (e.g., magma mixing) may have contributed to magmatic evolution throughout Castle Creek time, and may be responsible for creating some of the compositional diversity during that episode.

ACKNOWLEDGMENTS

First of all, I would like to thank my advisor, Dr. Wendy Bohrson. Wendy gave me the opportunity to work on a fascinating project and guided me through until the end. I am extremely grateful for her advising and her teaching as an undergraduate and a graduate student. I would also like to thank my other committee member here at Central, Dr. Paul Hoskin. Paul consistently provided practical solutions to impractical problems and constantly adjusted my focus during the course of the project. I thank him for all of his hard work. And to my outside committee member, Dr. Michael Clynne, I am greatly indebted. Dr. Clynne provided the foundation for this project and the preparation necessary to make it succeed. I would like to thank him for contributing his passion for Cascade volcanism.

Dr. Frank Ramos was not officially on the committee for this thesis, but contributed equally as much. I am grateful for Frank's passionate teaching on everything from to the fundaments of mass spectrometry to the details of isotopic systems. Allowing me into the lab granted me an opportunity very few students get. The Sr data generated for this thesis would not exist with the quality it does without him. I would also like to thank my wife Heather and my family for all of their support during the last two years. They were always encouraging and patiently provided everything I needed to finish the project. Many thanks go to the wonderful students of CWU's Geology Department for all of their help and patience. My office mate Ahnna deserves many thanks for guiding me through the writing process and simply putting up with me. Lastly I would like to acknowledge Central Washington University's Office of Graduate Studies and the National Science Foundation for providing the funding which made this thesis possible.

TABLE OF CONTENTS

TABLE OF CONTENTS (continued)

LIST OF TABLES

LIST OF FIGURES

LIST OF FIGURES (continued)

LIST OF APPENDICES

CHAPTER I

INTRODUCTION

Scope and Study Objective

The modern study of igneous petrology is centered on providing insight into a range of issues related to terrestrial magmatism. A significant proportion of this effort is aimed at further understanding processes of melt generation and transport and their associated timescales. Melt generation refers to any process that produces or allows production of molten material below Earth's surface, whereas transport refers to processes that promote movement of this molten material towards the surface. The timescales associated with each of these are variable and not well known. However, current hypotheses favor the operation of these processes over relatively short geologic timescales (e.g., Petford et al., 2000; Turner et al., 2003; Zellmer et al., 2003). Another significant focus of research in this field is understanding the dynamics and timescales of processes that contribute to compositional diversity in igneous rocks. Terrestrial silicate magmas span a range from relatively silica poor and magnesium rich (e.g., basalt) to silica rich and magnesium poor (e.g., rhyolite). The closed-system process of fractional crystallization, coupled with open-system magma chamber processes, such as assimilation and magma mixing, are often invoked as primary causes of this compositional variation among magmas. The effects of these processes are often revealed by collecting and investigating geochemical and isotopic data, along with petrographic and mineral-scale information (Spera and Bohrson, 2001; Dungan, 1987).

Volcanoes are an excellent subject for the investigation of open-system magmatic processes because volcanic products, such as lava flows, may be constrained stratigraphically by detailed field work, providing a relative eruptive timescale. Therefore, the processes that contribute to compositional variation in lavas can potentially be unraveled by investigating a series of stratigraphically oriented samples. The objective of this study is to characterize a suite of stratigraphically oriented lava flows erupted from Mount St. Helens (MSH) during Castle Creek time (2500-1700 years ago) using mineralogical, chemical and isotopic data. These data allow documentation of the signature of open-system processes which may have impacted the characteristics and composition of the lavas during magmatic evolution.

Previous work allowed me to develop hypotheses about the role of open-system processes in the evolution of the Castle Creek MSH magmas. By describing processes that modify magmas in crustal chambers, there is also potential to describe the source(s) of these magmas. This thesis also aims to provide constraints on the geometry of the magma reservoir system at Mount St. Helens during Castle Creek time. If all the lavas represented by this study are related by simple fractional crystallization, for example, then the data could support the conclusion that the magmas evolved in a simple, spatially continuous magma chamber. An alternative possibility, in which none of the lavas shows evidence of genetic relationship, might provide evidence for a complex, spatially fragmented reservoir system in which each discrete magma batch could evolve in relative isolation.

MSH is an ideal natural laboratory for a detailed petrological investigation. It lies in southwestern Washington State above an active subduction zone and is part of the Cascade volcanic arc. Over the last 300,000 years, MSH has been characterized by episodic explosive eruption and intermittent effusive activity that formed lava flows and domes. Explosive activity and dome building events of the past are similar to the May 18, 1980 eruption and the current (2004 and continuing) eruption, respectively. These events have historically involved dacite magma. Lava flows, however, span a more diverse compositional range, including andesite and, during one limited time period, basalt. Between approximately 2,500 and 1,700 years before the present, basaltic and basaltic andesite lava flows, along with more common andesite and dacite compositions, were erupted from MSH (Clynne et al., 2004). This time interval is termed the Castle Creek eruptive period. The basaltic lava flows from Castle Creek time are laterally discontinuous, and they apparently alternated with the eruption of dacite and andesite (Mullineaux and Crandell, 1981). The entire episode can be divided into five units: Cave basalt, Precave basalt, North Flank basalt, Castle Creek andesite and Castle Creek dacite. Eruption of a wide range of lava compositions at MSH during a short interval of time affords the unique opportunity to investigate open-system magma chamber processes. The small interval of time during which these eruptions occurred, and the rapid switches in erupted compositions, have many implications for the relative importance of closed versus open system processes and the geometry of the sub-volcanic magma reservoir.

Background

Open-System Magmatic Processes

Open system magma chamber processes are those that occur within magma chambers, over varying timescales, in a system open to chemical, mass and energy transfer (Spera and Bohrson, 2001). As previously mentioned, magma chamber processes are dominated by closed-system fractional crystallization (FC) and the open-system processes of crustal assimilation, magma recharge and magma mixing. Although a magma may undergo FC from the time it forms in its source region, crustal assimilation and magma recharge are thought to more commonly occur in shallow magma reservoirs.

Assimilation Fractional Crystallization (AFC)

Because magma in a crustal-level magma body is generally at a much higher temperature than the surrounding rock (termed wallrock), the principles of thermodynamics dictate that heat will flux from the magma to the wallrock until thermal equilibrium is reached. This is the driving force behind cooling and the subsequent crystallization of a magma body. Equilibrium crystallization allows the entire magma body to cool to a solid while retaining all of its original chemical components. This allows for solids that have precipitated to back-react with the liquid for the duration of cooling. Fractional crystallization is a cooling regime in which precipitated solids are separated from the remaining liquid and no longer partake in chemical reactions. Equilibrium crystallization and fractional crystallization have drastically different effects on the properties of a magma body; during equilibrium crystallization, the composition of

the crystal + melt system remains constant. In FC, because crystals are chemically isolated, the residual melt evolves, typically to more silicic compositions. The enthalpy exchange between magma and wallrock has been shown to deliver energy to and melt portions of the wallrock in a process known as anatexis. The anatectic melt so generated may subsequently be incorporated into the magma in a process known as assimilation. The effects of assimilation of anatectic melts into magma bodies have been recognized as important to petrogenesis and development of compositional diversity. The incorporation of anatectic melt may alter the composition of the magma residing in the magma chamber. Evidence for crustal contamination and assimilation includes mineralogical and petrographic data, such as disequilibrium phase assemblages, and disaggregated crustal xenoliths (e.g., Maury and Bizouard, 1974; McBirney et al., 1987; Rudnick et al., 1986). Ramos and Reid's (2005) study of $^{87}Sr/^{86}Sr$ ratios within phenocrysts from lavas erupted at Pisgah crater is an example of isotopic evidence that demonstrates clearly the effects of assimilation on crystal and magma chemistry. The combined effects of assimilation and fractional crystallization (AFC) were modeled by DePaolo (1981) in what became the first in a series of increasingly complex models describing AFC processes (e.g., DePaolo et al., 1992; Perry et al., 1993). The most recent algorithm describing AFC is the energy-constrained AFC model of Spera and Bohrson (2001).

Magma Mixing

Being that magmas are, at least in part, liquid, two or more discrete magmas coming into contact may mix, depending on various physical factors such as viscosity

and density. In the case of volcanic systems, where eruption and recharge of the system with fresh magma seem to be common (Spera and Bohrson, 2001; Knesel et al., 1999; Davidson and Tepley, 1997), mixing may indeed be a contributing process to compositional change. Magma mixing has been shown to occur along a continuum, ranging from formation of discrete mafic enclaves in a host magma body (e.g., Browne et al., 2006) to complete mixing of two distinct magmas to create a third hybrid magma (e.g., Clynne, 1999). Mixing magmas with contrasting viscosities and densities will result in less complete mixing, whereas magmas of similar viscosity and density may mix thoroughly (Sparks and Marshall, 1986). The mixing of two or more magmas will also have consequences for the mineral, chemical and isotopic composition of a magma.

Magma mixing has been proposed as a significant means of creating compositional diversity in igneous systems. For example, Eichelberger (1978) demonstrated how magma mixing may be fundamental in creating intermediate compositions in a system dominated by high and low silica end member magmas. The same work also eluded to how the mixing of a standing body of magma with a more mafic input from depth might work as a triggering mechanism for volcanic eruptions. This scenario has been demonstrated in other works such as Sparks et al. (1977), Clynne (1999), Watts et al. (1999), and Eichelberger and Izbekov (2000). If mixing is one of the triggers of an eruption, the composition of magmas involved influence the style in which the related volcanic center erupts. Mafic magma intruding into standing evolved magma often results in effusive eruptions (e.g., Clynne, 1999), while the opposite produces catastrophic eruptions (Eichelberger and Izbekov 2000).

The Cascadia Subduction Zone

Through much of Cenozoic time, the Cascadia margin of the Pacific Northwest has been a zone of convergence between North America and ocean plates of the Pacific basin (Atwater, 1970). Current plate velocities are 34 mm/yr for the Juan de Fuca-North America Plate boundary and 51 mm/yr for Pacific-North America Plate motion (Miller et al., 2002). The resulting N50˚E striking oblique subduction of the Juan de Fuca and former Farallon plates beneath North America is the cause of the vigorous magmatic and seismic activity in the region. A deformation front that exists roughly 100 km west of the Pacific Northwest coastline is considered the seaward edge of the Cascadia subduction zone. Inboard of the deformation front is a subduction complex composed of highly deformed marine sediments of mostly Pliocene to Miocene age (Snavely and Wells, 1996). The next major structural element is the Siletz terrane, a mafic igneous terrane which acts as the backstop to much of the subduction complex and the basement to much of the Cascadia forearc (Parsons et al., 1999). The Siletz terrane most likely represents an accreted ocean island chain of approximately Eocene age, which outcrops discontinuously from the southern tip of Vancouver Island in the north to central Oregon in the south (Duncan, 1982). In Washington, outcrops of the Siletz terrane are known as the Crescent Formation, while throughout Oregon they are referred to as the Siletz River Volcanics (Snavely et al., 1968). The Siletz terrane abuts Cascade Arc crust in the southern Washington Cascades, the location of the abutment being marked by the NNE-trending Mount St. Helens seismic zone and the west Rainier seismic zone. This is in

agreement with the postulation that the Siletz terrane focuses seismic deformation at its edges (Parsons et al., 1998)

The Cascade Volcanic Arc

The Cascade Range, extending from southern British Columbia, Canada, to northern California, USA, is the surface manifestation of the continental volcanic arc associated with Cascadia subduction. In southern Washington, the Quaternary expression of the volcanic arc lies 250 to 300 km east of the margin (Sherrod and Smith, 1990). Elsewhere in the Cascades, the volcanic front, as located by Guffanti and Weaver (1988), lies between 175 and 350 km east of the convergent margin. Mooney and Weaver (1989) estimate crustal thickness beneath the Cascades to be 40-45 km, in agreement with the seismic findings of Parsons et al. (1998). This thickness is generally considered to be constant along the north-south extent of the Cascade Range. The dip of the downgoing slab is a somewhat contested figure, with recent seismic velocity models placing the dip angle at about 15° below the southern Washington Cascades (Parsons et al., 1998). Michaelson and Weaver (1986) suggest that the steepest section of the slab dips >45°. This apparent discrepancy arises mainly because of geometric complexities within the subducting slab. Seismic velocity modeling by Michaelson and Weaver (1986) demonstrates that the slab dip-angle varies, depending on north-south position along the margin. The authors propose that the Juan de Fuca plate occurs as three segments with different dip angles in Washington and northern Oregon, with the slab dipping more steeply in the northern and southern segment than in the central segment. Due to the

proposed depth of the segmentation (approximately 45 km), the velocity model is unable to resolve the manner by which the change in dip angles are accommodated. However, Michaelson and Weaver (1987) infer that discrete tears in the slab accommodate the changing geometry.

Guffanti and Weaver (1988) divide the Cascades into six segments based on spatial, temporal and compositional distributions of approximately 4000 volcanic vents. These segments provide a framework for quick reference to any location in the Cascades. Segment 1 includes the southern British Columbia vents, Mount Baker and Glacier Peak of the Washington Cascades. Segment 2 extends from Mount Rainier in the north to Mount Hood in the south, including both Mount St. Helens and Mount Adams in between. Segment 3 covers the entire length of the remaining Oregon Cascades from Mount Jefferson to Mount McLoughlin. Segment 4 is limited to Mount Shasta and the Medicine Lake volcanic center in northern California. Segment 5 includes only Lassen Peak and associated volcanic vents. Lastly, segment 6 incorporates the WNW-ESE trend of the Oregon high lava plains, beginning in the east at Newberry volcanic center.

Mount St. Helens and Cascadia

Mount St. Helens is 50 km west of Mount Adams and the trend of the main volcanic arc (see Figure 1). Depending on the subduction zone geometry model invoked, the MSH edifice lies between 60 and 80 km above the surface of the downgoing slab (Parsons et al., 1998; Crosson and Owens, 1987; Michaelson and Weaver, 1986). Investigations into the structure of the subjacent crust and upper mantle beneath Mount

St. Helens have revealed a moderate degree of complexity. Weaver et al. (1987) investigated local crustal extension related to the St. Helens seismic zone, while Evarts et al. (1987) found the St. Helens seismic zone intersects other prominent crustal features including a number of Tertiary structures that define a broad NNE-trending zone and may be related to a regional weakening in the lithosphere (Evarts et al., 1987). This weakness in the lithosphere is interpreted as a controlling factor of the locus of magmatism in southern Washington. Mount St. Helens lies within this zone at the intersection of the NNW-striking St. Helens seismic zone and an ENE-trending alignment of Pleistocene silicic domes. The linear zone of silicic vents is probably controlled by a fault that has been interpreted from seismic records to occur directly beneath the volcano (Evarts et al., 1987).

Mount St. Helens (MSH) has erupted a wide range of compositions during the last 40000 years of eruptive activity. Lavas sampled at the surface reveal a range in SiO_2 contents between 49 and 70 wt % (Smith and Leeman, 1993). The eruptive history of the last 40 kyr has been divided into four stages and further subdivided into six named eruptive periods based on tephra chronology (Table 1). The Spirit Lake stage ranges from the present to 2,500 years B.P. and contains the Goat Rocks, Kalama, Sugar Bowl and Castle Creek periods. From 2,500 years B.P. to 40,000 years B.P. are the Pine Creek and Smith Creek eruptive periods, proceeded by the Swift Creek, Cougar and Ape Canyon stages (Mullineaux and Crandell, 1981). The striking fact about the compositional range erupted at Mount St. Helens is that the first 35,000 years of history are dominated by high-silica magmatism (Mullineaux and Crandell, 1981). It is not until the Castle Creek

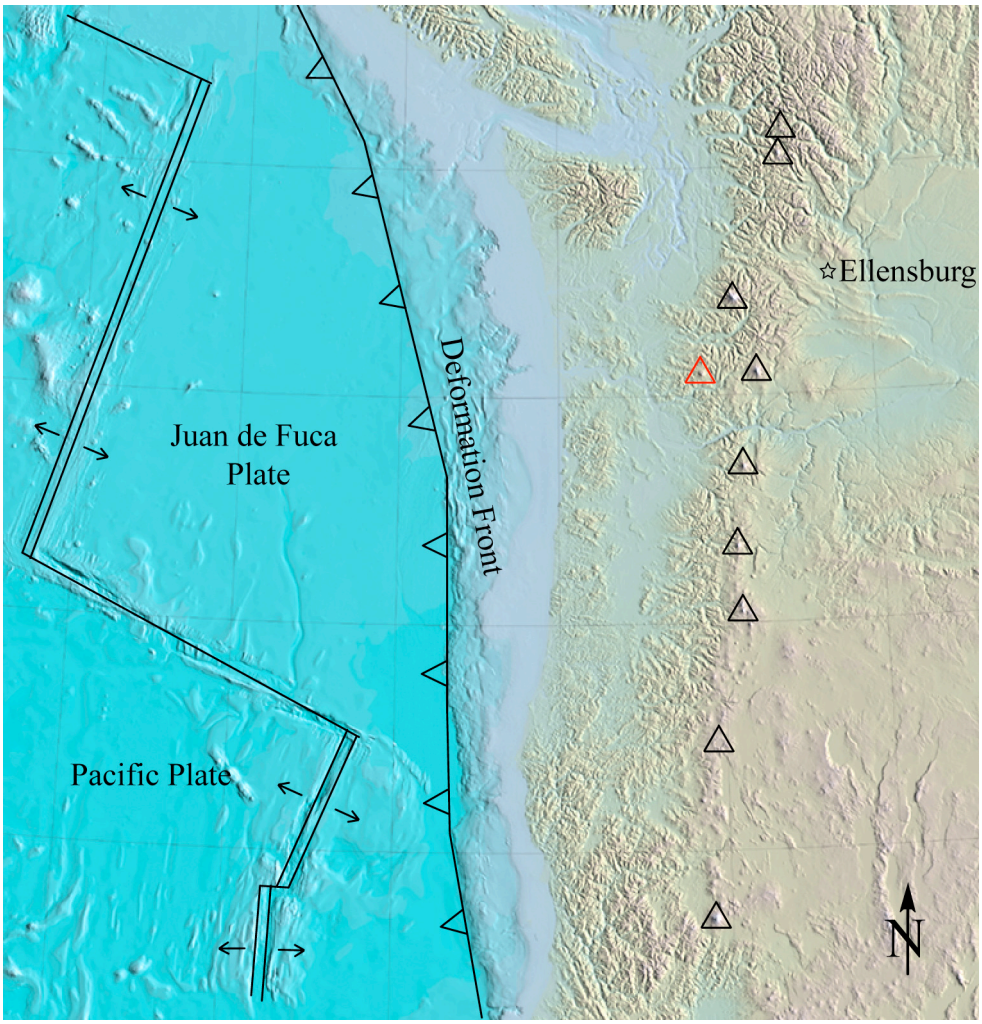

Figure 1. Tectonic and physiographic features of the northwestern United States. Mount St. Helens is indicated by red triangle. Figure modified after Haugerud (2004).

period that andesitic and basaltic compositions are erupted (along with dacite). Mafic volcanism alternates rapidly with dacite eruptions during Castle Creek time and marks the buildup of the single, large cone associated with modern Mount St. Helens. Mafic volcanism abruptly ceases around 1700 years B.P. (Clynne et al., 2004) and gives way to the Sugar Bowl period, which was dominated by the building of an augite-hornblende dacite dome at the northern base of the cone (Mullineaux and Crandell, 1981). After a

TABLE 1. SUMMARY OF ERUPTIVE HISTORY AT MOUNT ST. HELENS

Stage	Period	Approximate age* (years before 1950)	Eruptive products
	Goat Rocks	150-100	Dome
			lava flow
	Kalama	450-350	Pyroclastic flows
			Dome
			Lava flows
Spirit Lake			
	Sugar Bowl	1150	Dome, pyroclastic flows
	Castle Creek	2500-1700	Lava flows, Pyroclastic flows
	Pine Creek	3000-2700	Pyroclastic flows and domes
	Smith Creek	4000-3300	Pyroclastic flows
Swift Creek		13000-8000	Pyroclastic flows and domes
Cougar		20000-18000	Pyroclastic flows and domes
			Few lava flows
Ape Canyon		40000-35000	Pyroclastic flows

* Approximate ages from tephra chronology as compiled by Mullineaux and Crandell (1981).

short pause in activity, the edifice commenced eruption of andesite and dacite once again during the Kalama period, but erupted no basalt. Subsequent to the Kalama period, dacite once again dominates, including the eruption of May 18, 1980 and the current dome-building event initiated in October of 2004.

CHAPTER II

METHODS

The data collected for this thesis are from a number of analytical techniques ranging from petrography to micro-analytical techniques. In this section the techniques of this thesis will be described, including details of sample preparation.

Whole-Rock Powders

The term "whole-rock" sample typically refers to a hand sample size rock that can be used for a variety of chemical analyses. The entire rock is ground into a fine powder in a series of steps to ensure analysis of a homogeneous product. In this study, whole-rock powders were made by grinding in either a tungsten carbide, steel or aluminum shatterbox, or an agate ball mill. Samples were prepared primarily at Washington State University, but also at the sample preparation facilities at the Unites States geological Survey (USGS) Denver office. The selection of different media for grinding was based on the types of analyses the powder was created for. Powders created strictly for trace element analyses, for example, are typically ground in steel to prevent contamination by such elements as Co and Ta.

Whole-Rock Major Element Chemistry

Major element data for Castle Creek period basalts were compiled from unpublished datasets of M. Clynne, R. Hoblitt, J. Pallister, USGS; J. Gardner, University of Texas at Austin; Halliday et al. (1983); and Smith and Leeman (1993). New whole-rock major element analyses produced for this study were analyzed by X-ray

fluorescence (XRF) at Washington State University. XRF powders were weighed out in 3.5 to 3.505 g increments. Approximately 7.0 g of dilithium tetraborate ($Li_2B_4O_7$) were then added as a flux, resulting in a 1:2 ratio of sample to flux measured to within 0.002 g. The entire mixture was then thoroughly homogenized in a sample shaker, poured into graphite crucibles and fused into a glass bead in a muffle furnace at approximately 1000 °C for 5 minutes. The resulting glass beads were allowed to cool and then ground once again in a tungsten carbide shatterbox. The powdered samples were then fused a second time at 1000 °C, allowed to cool, and then polished into a bead on diamond lap wheels in final preparation for XRF analysis. Analyses were performed on a ThermoARL Advant'XP+ sequential X-ray fluorescence spectrometer in the Washington State University geoanalytical facilities. All analyses were performed with a rhodium target run at 50 kV accelerating voltage and 50 mA current. Two standard beads (BCR-P and GSP-1) are used as internal standards, and are run between every 28 unknown samples. Oxidation state of iron is typically ignored in whole rock samples. Iron values as determined by this technique are assumed to be FeO, and all analyses are normalized to 100% on a volatile free basis.

Whole-Rock Trace Element Chemistry

Whole-rock trace element data were compiled from the aforementioned list of published and unpublished works. New trace element analyses for this study were collected at Washington State University by inductively coupled plasma mass spectrometry (ICP-MS). Splits of sample powders used for major element analyses were

prepared for trace element analysis. Powders were weighed in 2 to 2.005 g increments, with an additional approximately 2 g of $Li_2B_4O_7$ added as flux to result in a mixture ratio of 1:1 measured to within 0.0010 g. The dry mixture was then thoroughly homogenized in a sample shaker and loaded into graphite crucibles. The mixture was then fused into a glass bead at 1000 °C and allowed to cool. The glass bead was re-ground into a powder in a steel shatterbox. 250 mg of this powder is dissolved on a hotplate at 110 °C, using 6 ml hydrofluoric acid (HF), 2 ml nitric acid (HNO_3), and 2 ml perchloric acid ($HClO_4$) in an open Teflon vial. The sample is evaporated to dryness. An additional evaporation with 2 ml $HClO_4$ at 165 °C to convert insoluble fluorides to soluble perchlorates follows. 3 ml HNO_3, 8 drops H_2O_2, 5 drops of HF and an internal standard of indium, rhenium, and ruthenium are added to the sample, which is then diluted up to 60 ml final volume. The resulting solution was analyzed on the HP 4500+ Quadrapole ICP-MS in the Washington State University geoanalytical facilities. While instrumental uncertainty typically lies between 1-4%, uncertainty varies with each element and reaches a maximum of approximately 9%. Analyses of U and Th are the most uncertain, while most rare earth element (REE) analyses are between 1-3%.

Whole-Rock Strontium Isotopic Analysis

The 17 samples that compose the new major and trace element data set were also analyzed for Sr isotopic composition. Powdered samples were prepared in Central Washington University's clean lab facilities for analysis by thermal ionization mass spectrometry (TIMS). Approximately 100 g of whole-rock powder was weighed out and

placed in 20 ml Teflon vessels. Powders were digested in a mixture of concentrated nitric acid (HNO_3) and concentrated hydrofluoric acid (HF) in a sealed Teflon vessel at 200 °C for 24 hours. After 24 hours of digestion time, any remaining fluid was evaporated on a hot plate. Concentrated HNO_3 was added to the remaining solids, and the process was repeated. The third and final stage of dissolution used 12 N Hydrochloric acid (HCl) to dissolve remaining solids. Upon completion of the digestion process, the sample was thoroughly evaporated on a hot plate. Prior to drying, each sample was visually inspected to ensure complete dissolution. Addition of 1 ml of 2.5 N HCl remobilized the contents as a solution, which was then split as two equal aliquots.

A 0.5 ml aliquot of each sample was loaded into 22 ml glass columns containing cation exchange resin and elution medium of 2.5 N HCl. This process was used to isolate Sr based on known rates of cation exchange for the particular resin used. 2.5 N HCl was added in six steps: 0.5 ml, 2 ml, 6 ml, 3 ml, 6 ml, and 6 ml. An aliquot of pure Sr was collected during the second 6 ml wash. Rare earth elements were collected in a 10 ml wash of 6 N HCl after 2.5 N HCl additions were complete. Sr samples were loaded onto rhenium filaments on cathodian beads in a solution of TaO_2 and 5% phosphoric acid. Analyses were performed on a VG Isotopes sector 54 run in dynamic mode, with 5 collectors sequentially analyzing masses 88 through 84 and reporting the average for each mass. Reported ratios are the mean of 150 of such sequences. Error is reported as standard 2σ error.

Petrography

Petrographic descriptions were accomplished through the use of a Nikon E600 polarizing microscope and standard 27 by 46 mm, 30 μm petrographic sections. Visual estimation techniques were used to approximate modal percentages of mineral phases found within the section. Maximum and average sizes were found for representative phenocrysts of each phase present in the sample through the use of a stage micrometer. Crystal features such as textures, twinning and zoning found were described.

Quantitative Petrography

In addition to collection of standard petrographic data, quantitative petrographic data was collected in the form of plagioclase crystal size distributions (CSDs). CSD data can be assessed by examining a plot of the natural log of nucleation density (number of crystals per volume) versus major axis crystal length, and are controlled by equation 1:

$$\ln n = \ln n_0 - L/G\tau \qquad (1)$$

where n is nucleation density, n_0 is initial nucleation density, G is growth rate in mm per second, and τ is average residence time. The equation is easily rearranged to solve for average residence time or growth rate. If the average crystal residence time is not known (very precisely), then a growth rate must be assumed. In this study, growth rates were assigned to plagioclase based on the results of experimental petrology studies. Further discussion on the assignment of growth rates is found in chapter 4. Equation 2 is used to solve for average residence time and assumes the following form:

$$\tau = (-1/G)m \qquad (2)$$

where τ is time, G equals the growth rate and m is equal to the slope of the data array, in a plot of nucleation density versus length, as defined by linear least squares regression.

In this study CSD data were gathered from digital X-ray element distribution maps of entire polished sections with the aid of imaging software. X-ray element distribution maps were generated via the Cameca SX-50 electron microprobe at Oregon State University for Al, Ca, Mg, and K. In the case of plagioclase CSDs, the Al map was used. Images were loaded into National Institute of Health (NIH) ImageJ version 1.33u. ImageJ was written in Java by Wayne Rasband, NIH, Bethesda, Maryland, and can be found at http://rsb.info.nih.gov/ij. The threshold command sets a user defined range within grayscale. This process, performed on element distribution maps, effectively isolates plagioclase crystals from all other phases and features found within the image of the polished section. Measurements are performed via the measure tool within NIH ImageJ. ImageJ was written in Java by Wayne Rasband, NIH, Bethesda, Maryland, and can be found at http://rsb.info.nih.gov/ij. For all crystals falling within the range of grayscale defined by the threshold, this tool fits an ellipse to the individual crystal, measures a major axis length, a minor axis length, area of the ellipse and counts each crystal. Data gathered by the measure command in ImageJ are first reduced in Kaleidegraph where raw crystal length data and crystal numbers are binned, thus creating numbers of crystals per size fraction. These data are imported into Excel where a series of calculations are done. The difference between each bin size is calculated, thus creating column dL. Numbers of crystals are divided by the area of the polished section they were measured from, creating a column of number of crystals per area. This column is raised

to the 3/2 power to reconcile the two-dimensional nature of CSDs, thus creating number of crystals per volume. A running sum is applied to this column, from which the number/volume column is subtracted, creating column dN. This column is divided by column dL, creating column n. The natural log of column n is then taken. CSD plots are created by plotting length (mm) on the x-axis and the natural log of nucleation density (n) on the y-axis. Excel was used to calculate linear least squares regressions for each data array.

Nomarski Differential Interference Contrast Microscopy

Microscopy was conducted on the plagioclase phenocryst population to document the textural variations evident in Castle Creek lavas. Nomarski differential interference contrast (NDIC) microscopy is a reflected light beam-splitting technique in which the reference beam is sheared by a minuscule amount producing a monochromatic shadow-cast image. Plagioclase crystals in 150 μm polished sections are etched with flouroboric (HBF_4) acid for 25 seconds. HBF_4 differentially etches plagioclase crystals according to An content, creating micro-topography readily visible with the NDIC technique because of the shadow cast effect.

Electron Microprobe Analysis

Electron microprobe analyses were completed on feldspar crystals found within 5 of the basaltic samples. The JEOL 733 superprobe at the University of Washington's Department of Earth and Space Sciences was used. Relevant instrument settings include 3-micron spot size, accelerating voltage of 15 kV and a current of 30 mA. Cross

comparison of NDIC with back-scattered electron (BSE) imagery taken during analyses provided the best means of picking analysis locations. NDIC imagery was used to pre-assess textural discontinuities and plan sampling location priorities, while BSE imagery often provided a fine tuning of the analysis location. On some occasions, compositional variations not seen with the NDIC technique were identifiable with BSE imaging. BSE imaging also provided the most accurate means of recording analysis locations on each individual feldspar. Thirty-nine crystals were analyzed from the five samples. Analysis locations included cores and rims for most samples; in some case points intermediate between these were also analyzed.

The MELTS Algorithm

The evolution of the melts that produced the Cave, Precave and North Flank basalts was modeled with the computer-based thermodynamic phase equilibria model known as MELTS (Ghiorso and Sack, 1995; Asimow and Ghiorso, 1998). MELTS calculates equilibrium phase relationships based on thermodynamics with system constraints provided by initial input parameters. Evolution scenarios for user-defined magma bodies can be modeled with MELTS as a series of steps in temperature and pressure, temperature and volume, enthalpy and pressure, or entropy and pressure. Isenthalpic, isentropic or isochoric scenarios can be utilized as well. Equilibrium may also be calculated in systems open to oxygen transfer at a fixed oxygen fugacity. This allows simulations to proceed at a specified oxygen buffer for the duration of the model run. Water is included as a component in the liquid phase and as a separate pure phase,

and the effect of water on phase equilibria is included in the model (Ghiorso and Sack, 1995). Models produced by this study were held at isobaric conditions while temperature of the system was incrementally reduced from above calculated liquidi to approximately 800 °C. Each scenario ran under fractional crystallization conditions, and input parameters regarding initial chemical composition were taken from whole-rock data. Initial sensitivity testing was conducted by varying pressure, water content and oxygen fugacity (fO_2) of the system while holding other parameters constant.

CHAPTER III

RESULTS

Petrography

Among the samples examined for this study, basalts erupted during the Castle Creek period are petrographically similar. One sample from the Cave basalt (SC99-302), 2 from the Precave basalt (SC99-301, SC98-271), and 2 samples from the North Flank basalt (W95-60B, SC02-527) were examined in detail. The samples are intergranular, holocrystalline lavas with phenocrysts of plagioclase feldspar, olivine, pyroxene, and an opaque phase(s). The groundmass of all samples is composed primarily of plagioclase and pyroxene. Because of the large percentage of plagioclase in the groundmass, most samples are composed of upwards of 50% plagioclase crystals in total. Table 2 summarizes petrographic information.

Plagioclase is the most abundant phase in all samples examined and exhibits a wide range in crystal size (Table 2). As a groundmass phase, the mineral occurs primarily as euhedral tabular laths slightly elongated parallel to the crystallographic a-axis. Large plagioclase phenocrysts are more variable in morphology, including a range from partially resorbed anhedral crystals to euhedral, tabular laths. Partially resorbed plagioclase crystals usually display dusty cores or sieve textures in the central areas of the crystal. These zones are often rich with inclusions, some of which are glass and others of which are opaque phase(s). The lavas range between porphyritic and seriate textures where plagioclase is concerned; Cave basalt being the most porphyritic while others tend towards seriate.

TABLE 2. SUMMARY OF CASTLE CREEK BASALT PETROGRAPHY

Sample	SC99-302	SC99-301	SC98-271	W95-60B	SC02-527
Unit	Cave	Precave	Precave	North Flank	North Flank
Plagioclase	35%	50%	30%	40%	45%
Size (μm)	3000–75	2000–75	2000–50	1600–25	2000–75
Olivine	10%	10%	10%	20%	15%
Size (μm)	1000–250	500	1000–100	2000–200	1000–150
Pyroxene	5%	5%	3%	5%	2%
Size (μm)	<50	<50	<50	100–50	150–50
Opaque(s)	5%	5%	5%	5%	5%
Size (μm)	<50	100-25	<25	<25	<25
Vesicles	20%	20%	0%	5%	10%
Size (μm)	6000–500	6000–300	-	<200	-
Groundmass	25%	10%	52%	25%	23%

Olivine phenocrysts make up between 5 and 15 modal percent, the lower percentages belonging to Cave and Precave rocks. Like plagioclase, olivine is also quite variable in size. Phenocrysts were estimated to be as large as 2 mm and as small as 150 μm. North Flank samples have both higher proportions of olivine and larger olivine crystal sizes. Most olivine grains are slightly green in plane-polarized light (PPL) and some display poor cleavage at ~90°. Olivine is often reacted or altered, some crystals displaying a highly skeletonized texture. Embayments in skeletonized olivine from North Flank basalts contain plagioclase. Rust to honey-colored alteration is visible in PPL and is common along fractures or margins of olivine grains; the altered regions are probably iddingsite. The occurrence of pyroxene in these samples is quite varied. Most commonly, pyroxene is a small (25–100 μm), groundmass phase that fills interstices,

occurring as clouds of interlocking anhedral crystals. In Precave sample SC99-301, pyroxene textures vary between interstitial and oikiocrystic, and crystals reach slightly larger sizes (200 μm) compared to other samples. In North Flank sample SC02-527, pyroxene occurs as a phenocryst phase, but in a very low modal percentage (<1%). The small anhedral interstitial pyroxenes found in the groundmass of most samples could not be identified further than most appear to be clinopyroxene. Phenocrystic pyroxene in sample SC02-527 appears to be clinopyroxene as well.

Opaque phases are typically equant, euhedral to subhedral grains varying in size between 25 and 100 μm and comprising between 5 and 10 modal percent of the sample. Based on morphology and reflected light techniques, the dominant opaque phase is tentatively identified as magnetite.

Crystal Size Distributions

Plagioclase crystal size distributions for 5 samples of Castle Creek age basalt yield similar results. All CSD plots contain two distinguishable data arrays. These are divided into the phenocryst array and the microphenocryst array. Phenocryst sizes are defined as 475 to 2500 μm and above. Microphenocryst sizes range from the lower limit of measurement to 475 μm. These size divisions are the end members for all samples. Size categories vary with each sample; details of these divisions may be found in Table 3. Slope and intercept data, gathered through linear least squares regression, encompass a range of values. Phenocryst arrays have slopes between –0.49 and –1.66 with a mean of –0.99. Phenocryst intercepts vary between –0.91 and –1.78 with a mean of –1.40.

TABLE 3. SLOPE AND INTERCEPT VALUES FOR PLAGIOCLASE CSDS

Microphenocrysts

Sample	Slope	y-intercept	R^2	Size range (μm)	Core An	Rim An
SC99-302	–18.00	7.79	0.96	0–475	79.3	74.3
SC99-301	–10.23	6.10	0.94	0–580	69.0	62.7
SC99-271	–17.15	6.70	0.98	0–410	77.8	45.9
W95-60B	–15.64	6.95	0.90	0–540	74.9	74.1
SC02-527	–18.95	7.29	0.97	0–510	80.8	70.2

Phenocrysts

Sample	slope	y-intercept	R^2	Size range (μm)	Core An	Rim An
SC99-302	–1.66	–1.14	0.90	590–1800	77.7	72.3
SC99-301	–0.85	–0.91	0.24	640–2300	77.5	67.5
SC99-271	–0.49	–1.78	0.23	475–2400	81.7	74.9
W95-60B	–0.86	–1.40	0.22	570–2300	78.7	59.7
SC02-527	–1.09	–1.78	0.64	600–2500	66.2	75.3

Microphenocryst data arrays have slope and intercept values between –10.23 and –18.95 and 6.10 and 7.79, respectively. Mean slope value for microphenocryst arrays is –16.0 with an intercept mean of 6.97. R^2 values for phenocryst regressions are as good as 0.90 and as poor as 0.22. Regression of microphenocryst data yielded R^2 values between 0.90 and 0.98.

The poor fit to the phenocryst data probably arises from the low number of larger crystals found within a given sample space, as discussed by Gualda (2006). Counting statistics for CSD measurements are available in Table 4. Furthermore, most CSDs show a large scattering of data within the lowest size categories of phenocryst data, which may be natural or an artifact of the CSD methods employed by this study.

Nomarski differential Interference Contrast Microscopy

Nomarski images of plagioclase phenocrysts and microphenocrysts among the 5 samples reveal an array of textural features. The most common feature is alternating

TABLE 4. PLAGIOCLASE CSD MEASUREMENT DATA

Sample	Unit	Number of crystals counted			
		0–100 μm	101–500 μm	501–3500 μm	Total
SC99-302	Cave	1133	629	17	1779
SC99-301	Precave	505	420	43	968
SC98-271	Precave	458	256	16	730
W95-60B	North Flank	1016	1550	44	2610
SC02-527	North Flank	1785	284	31	2100

high and low relief. This type of zoning is found throughout the samples. Areas of high and low relief within crystals vary in width from a few μm to tens of μm. Some crystals are composed of zones that have very consistent width; others show radical variation. Large phenocrysts typically show more variation in zone width and relief than microphenocrysts. However, plagioclase in Cave basalt sample SC99-302 has similar, consistent zone widths and relief amplitudes throughout the available size range. Alternatively, Precave sample SC98-271 has large variations in zone width and relief amplitude within large phenocrysts, whereas microphenocrysts have low relief, and small, consistent zone widths. The type of zoning within these samples is controlled by anorthite/albite composition and is typically referred to as oscillatory zoning. Anderson (1983) demonstrated the NDIC technique was able to resolve compositional zones down to about the 1% An level.

Plagioclase phenocrysts with sieve textures are found throughout the 5 samples of Castle Creek basalt. The abundance of such crystals varies with sample. Cave sample SC99-302 has the fewest sieve-textured crystals, while Precave and North Flank samples have a greater abundance. As discussed in the petrography section, these textures occur most commonly within the center of the crystal. Larger plagioclase phenocrysts in

sample SC02-527 sometimes contain resorption haloes at some intermediate distance between core and rim. Regardless of the position of sieve textures within the crystal, immediately adjacent areas typically display oscillatory zoning.

Electron Microprobe Analyses

Electron microprobe (EMP) analyses were collected on 39 crystals in the 5 samples. Results are shown in Tables 5, 6 and 7. Data are reported as wt% oxide on a non-normalized basis. Anorthite, albite and orthoclase contents are reported as molar percentages. Core Anorthite contents for all samples range from An_{58-89}, with an average of 76.5 ± 6.7. Rim analyses for all samples resulted in anorthite contents between An_{46} and An_{80}, with an average of 69.2 ± 11.7.

BSE images were acquired of each plagioclase crystal analyzed in order to provide accurate locations of analyses. BSE images also provide an additional means of visualizing spatial compositional changes within an individual crystal, and when used in conjunction with NDIC imagery, provide a complete detailed image of spatial compositional relationships. In some instances, BSE imagery reveals compositional changes that were not resolvable with the NDIC technique. However, in the majority of cases, complex regions visible with NDIC appeared as simple regions (i.e., single shade of gray) in the BSE images. Figures 2-6 illustrate the locations of EMP analyses from 5 crystals on the NDIC and BSE images. Appendices 1 through 5 provide the complete set of BSE and NDIC images, along with EMP spot locations, produced by this study.

TABLE 5. FELDSPAR CORE ANALYSES BY ELECTRON MICROPROBE

		wt% Oxide							Mol %		
Sample	L (mm)	SiO_2	Al_2O_3	FeO	CaO	Na_2O	K_2O	Total	An	Ab	Or
Cave basalts											
302-1a	2.36	51.25	29.99	0.42	13.28	3.88	0.13	98.94	76.8	22.4	0.7
302-3a	2.63	52.32	29.74	0.39	13.02	3.96	0.12	99.56	76.1	23.2	0.7
302-5a	2.68	52.16	29.60	0.41	13.01	3.88	0.11	99.17	76.5	22.8	0.7
302-11a	0.30	51.23	30.13	0.43	13.84	3.53	0.09	99.25	79.3	20.2	0.5
302-12a	1.30	49.59	31.13	0.39	14.76	3.09	0.10	99.06	82.2	17.2	0.5
302-10a	1.32	52.05	30.00	0.46	13.28	3.76	0.07	99.62	77.6	22.0	0.4
302-8a	1.93	51.40	29.55	0.38	13.32	3.88	0.09	98.63	77.0	22.4	0.5
Precave basalts											
301-10a	1.21	48.77	30.61	0.48	13.97	3.18	0.10	97.11	81.0	18.4	0.6
301-8a	1.13	51.47	28.68	0.35	11.58	4.54	0.13	96.75	71.3	27.9	0.8
301-12a	1.20	52.57	29.24	0.57	12.44	4.18	0.14	99.14	74.2	24.9	0.8
301-6a	0.91	50.46	29.58	0.49	12.89	3.93	0.08	97.43	76.3	23.3	0.5
301-7a	1.24	49.63	31.08	0.41	14.44	3.06	0.09	98.71	82.1	17.4	0.5
301-2a	1.69	50.08	31.03	0.43	14.36	2.99	0.07	98.97	82.4	17.2	0.4
301-3a	2.03	52.38	29.51	0.56	12.55	4.04	0.13	99.17	75.1	24.2	0.8
301-11a	0.60	50.80	30.29	0.48	13.75	3.40	0.09	98.81	79.8	19.7	0.5
301-gm	0.13	56.54	25.98	0.84	8.95	6.01	0.41	98.73	58.3	39.1	2.6
271-10a	1.98	52.06	29.69	0.43	12.82	4.18	0.15	99.33	74.8	24.4	0.9
271-1a	1.57	51.46	30.16	0.62	13.72	3.61	0.11	99.68	78.7	20.7	0.6
271-3a	1.53	52.03	29.71	0.59	13.18	3.76	0.13	99.40	77.2	22.0	0.7
271-16a	0.27	51.20	29.77	0.60	13.33	3.70	0.11	98.72	77.8	21.6	0.7
271-15a	1.06	49.25	31.56	0.53	15.27	2.75	0.06	99.42	84.5	15.2	0.3
271-5a	0.97	47.49	33.00	0.45	16.70	2.03	0.06	99.74	88.9	10.8	0.3
271-6a	0.85	48.63	31.99	0.62	15.55	2.43	0.07	99.29	86.2	13.5	0.4
North Flank basalts											
60b-12a	1.25	49.84	31.15	0.49	14.18	2.95	0.14	98.75	82.1	17.1	0.8
60b-13a	0.65	50.28	31.21	0.55	13.89	3.24	0.16	99.32	80.3	18.7	0.9
60b-4a	1.94	55.10	27.54	0.43	12.00	5.61	0.23	100.91	67.3	31.4	1.3
60b-6a	1.23	49.74	31.17	0.55	14.35	3.03	0.17	99.01	81.8	17.3	1.0
60b-gm	0.29	52.91	29.17	0.59	11.85	4.32	0.31	99.15	71.9	26.2	1.9
60b-10a	0.46	51.06	30.69	0.48	13.65	3.34	0.18	99.41	79.5	19.5	1.0
60b-2a	0.62	49.83	30.61	0.49	13.96	3.01	0.14	98.04	81.6	17.6	0.8
60b-16a	0.35	52.46	29.30	0.52	12.16	4.21	0.24	98.88	73.2	25.3	1.5
60b-14a	1.20	50.99	30.34	0.51	13.46	3.44	0.16	98.89	78.9	20.2	0.9
527-9a	0.82	55.43	27.56	0.49	10.34	5.40	0.24	99.46	64.7	33.8	1.5
527-10a	0.60	54.61	27.71	0.62	11.21	5.17	0.18	99.49	67.7	31.2	1.1
527-2a	2.13	54.25	28.56	0.57	11.58	4.77	0.12	99.86	70.3	29.0	0.8
527-14a	0.69	56.86	26.52	0.42	9.24	6.25	0.21	99.51	58.8	39.8	1.4
527-15a	0.83	54.44	28.19	0.50	11.35	4.84	0.19	99.52	69.3	29.6	1.2
527-17a	0.42	50.42	30.96	0.49	14.57	3.12	0.07	99.63	82.0	17.6	0.4
527-18a	0.48	50.71	30.56	0.55	14.02	3.49	0.10	99.43	79.6	19.8	0.6
Avg	1.15	51.6	29.8	0.5	13.1	3.8	0.1	99.1	76.5	22.7	0.8
StDev	0.68	2.14	1.45	0.09	1.58	0.94	0.07	0.74	6.7	6.4	0.5

TABLE 6. FELDSPAR RIM ANALYSES BY ELECTRON MICROPROBE

		wt% Oxide							Mol %		
Sample	L (mm)	SiO_2	Al_2O_3	FeO	CaO	Na_2O	K_2O	Total	An	Ab	Or
Cave basalts											
302-1c	2.36	52.58	29.48	0.52	12.90	4.20	0.12	99.81	74.9	24.4	0.7
302-3c	2.63	52.85	28.80	0.66	12.20	4.46	0.14	99.12	72.6	26.5	0.9
302-5c	2.68	52.86	28.82	0.63	12.35	4.45	0.13	99.23	73.0	26.3	0.8
302-11b	0.30	52.44	29.45	0.81	12.51	4.19	0.14	99.54	74.3	24.9	0.8
302-12c	1.30	57.25	25.70	0.85	8.97	6.16	0.32	99.25	58.1	39.9	2.1
302-10d	1.32	51.90	29.96	0.41	13.37	3.77	0.10	99.52	77.5	21.9	0.6
302-8b	1.93	51.35	29.89	0.42	13.45	3.79	0.11	99.01	77.5	21.9	0.6
Precave basalts											
301-10c	1.21	55.09	27.52	0.89	10.54	5.22	0.25	99.52	65.8	32.6	1.6
301-8c	1.13	52.06	28.58	0.54	11.63	4.56	0.19	97.56	71.0	27.8	1.2
301-12c	1.20	54.01	28.37	0.58	11.20	4.77	0.21	99.14	69.2	29.5	1.3
301-6b	0.91	53.29	28.68	0.56	11.89	4.46	0.19	99.07	71.9	27.0	1.1
301-7b	1.24	55.94	26.91	0.73	9.89	5.42	0.28	99.18	63.5	34.8	1.8
301-2c	1.69	57.16	26.56	0.78	9.02	5.83	0.32	99.68	59.5	38.4	2.1
301-3b	2.03	53.63	28.70	0.56	11.91	4.51	0.17	99.48	71.8	27.2	1.0
301-11c	0.60	54.63	27.53	0.69	10.78	5.05	0.24	98.92	67.1	31.4	1.5
301-gm	0.13	56.54	25.98	0.84	8.95	6.01	0.41	98.73	58.3	39.1	2.6
271-10e	1.98	51.85	29.87	0.60	13.14	3.86	0.11	99.42	76.8	22.6	0.6
271-1a	1.57	51.46	30.16	0.62	13.72	3.61	0.11	99.68	78.7	20.7	0.6
271-3b	1.53	51.59	30.24	0.59	13.52	3.73	0.12	99.80	77.8	21.5	0.7
271-16b	0.27	60.45	24.33	0.93	6.69	7.16	0.73	100.30	45.9	49.1	5.0
271-15c	1.06	55.03	27.60	0.72	10.79	5.17	0.22	99.53	66.7	32.0	1.4
271-5b	0.97	53.36	29.22	0.70	12.31	4.44	0.21	100.25	72.6	26.2	1.3
271-6b	0.85	51.78	29.63	0.61	13.26	3.85	0.14	99.26	76.9	22.3	0.8
North Flank basalts											
60b-12b	1.25	53.75	28.76	0.61	11.53	4.60	0.28	99.53	70.3	28.0	1.7
60b-13d	0.65	65.30	20.63	0.48	1.99	7.36	4.43	100.19	14.5	53.4	32.1
60b-4c	1.94	57.66	26.09	0.82	8.17	6.39	0.58	99.70	54.0	42.2	3.8
60b-6b2	1.23	52.41	29.07	0.68	12.00	4.36	0.25	98.77	72.2	26.3	1.5
60b-gm	0.29	52.91	29.17	0.59	11.85	4.32	0.31	99.15	71.9	26.2	1.9
60b-10b	0.46	53.94	28.71	0.61	11.34	4.54	0.29	99.43	70.2	28.1	1.8
60b-2b	0.62	52.99	28.95	0.60	11.71	4.38	0.26	98.89	71.6	26.8	1.6
60b-16b	0.35	50.34	30.97	0.63	13.75	3.20	0.18	99.06	80.3	18.7	1.0
60b-14b	1.20	52.04	29.84	0.50	12.61	3.87	0.19	99.04	75.7	23.2	1.1
527-9c	0.82	50.93	30.02	0.53	13.48	3.66	0.11	98.73	78.2	21.2	0.6
527-10b	0.60	52.68	29.09	0.69	12.60	4.31	0.15	99.52	73.8	25.3	0.9
527-2d	2.13	51.70	30.02	0.55	13.59	3.80	0.09	99.74	77.8	21.7	0.5
527-14b	0.69	54.64	27.59	0.68	11.03	5.02	0.21	99.16	67.8	30.9	1.3
527-15b	0.83	33.10	30.73	0.56	13.82	3.57	0.11	81.89	79.0	20.4	0.6
527-17b	0.42	55.36	27.50	0.71	10.55	5.34	0.24	99.71	65.4	33.1	1.5
527-18b	0.48	52.51	29.22	0.66	12.87	4.15	0.15	99.56	74.9	24.2	0.9
Avg	1.15	53.4	28.4	0.6	11.5	4.7	0.3	98.9	69.2	28.7	2.2
StDev	0.68	4.37	1.95	0.12	2.30	0.97	0.69	2.84	11.7	7.8	5.0

TABLE 7. FELDSPAR INTERMEDIATE ANALYSES BY ELECTRON MICROPROBE

		wt% Oxide							Mol %		
Sample	L (mm)	SiO_2	Al_2O_3	FeO	CaO	Na_2O	K_2O	Total	An	Ab	Or
Cave basalts											
302-1b	2.36	52.24	29.68	0.42	13.26	3.95	0.08	99.63	76.7	22.8	0.5
302-3b	2.63	50.90	30.15	0.40	13.71	3.65	0.10	98.90	78.5	20.9	0.6
302-5b	2.68	49.39	31.28	0.42	14.87	2.84	0.05	98.85	83.8	16.0	0.3
302-12b	1.30	52.38	29.39	0.40	13.01	3.93	0.13	99.24	76.2	23.0	0.8
302-10b	1.32	51.29	29.79	0.44	13.53	3.67	0.11	98.82	78.2	21.2	0.6
302-10c	1.32	52.01	29.75	0.41	13.29	3.77	0.10	99.33	77.5	22.0	0.6
Precave basalts											
301-10b	1.21	48.23	31.98	0.44	15.08	2.63	0.07	98.42	84.8	14.8	0.4
301-8b	1.13	50.81	30.02	0.50	13.36	3.52	0.12	98.34	78.6	20.7	0.7
301-12b	1.20	48.73	29.98	0.66	13.38	3.48	0.10	96.33	78.9	20.5	0.6
301-2b	1.69	49.81	31.28	0.47	14.12	3.04	0.08	98.81	81.9	17.6	0.5
301-11b	0.60	49.37	31.64	0.45	14.77	2.76	0.06	99.05	84.0	15.7	0.3
271-10b	1.98	54.04	28.51	0.32	11.64	4.79	0.10	99.41	70.4	29.0	0.6
271-10c	1.98	50.49	30.92	0.41	14.37	3.30	0.07	99.56	81.0	18.6	0.4
271-10d	1.98	54.95	27.85	0.52	10.86	5.17	0.14	99.50	67.2	32.0	0.9
271-15b	1.06	50.31	30.79	0.54	14.27	3.38	0.09	99.39	80.5	19.1	0.5
North Flank basalts											
60b-13b	0.65	50.16	31.27	0.54	14.45	2.98	0.14	99.54	82.2	17.0	0.8
60b-13c	0.65	51.67	30.11	0.51	13.17	3.69	0.17	99.32	77.3	21.7	1.0
60b-4b	1.94	49.16	32.01	0.48	15.06	2.59	0.08	99.38	84.9	14.6	0.4
527-9b	0.82	54.39	28.49	0.51	11.52	4.78	0.17	99.87	69.9	29.0	1.1
527-2b	2.13	54.50	28.17	0.34	11.34	5.10	0.14	99.60	68.4	30.8	0.9
527-2c	2.13	52.92	29.08	0.51	12.62	4.24	0.08	99.45	74.5	25.0	0.5
Avg	1.56	51.32	30.10	0.46	13.41	3.68	0.10	99.08	77.9	21.5	0.6
StDev	0.65	1.99	1.24	0.08	1.25	0.78	0.03	0.75	5.3	5.2	0.2

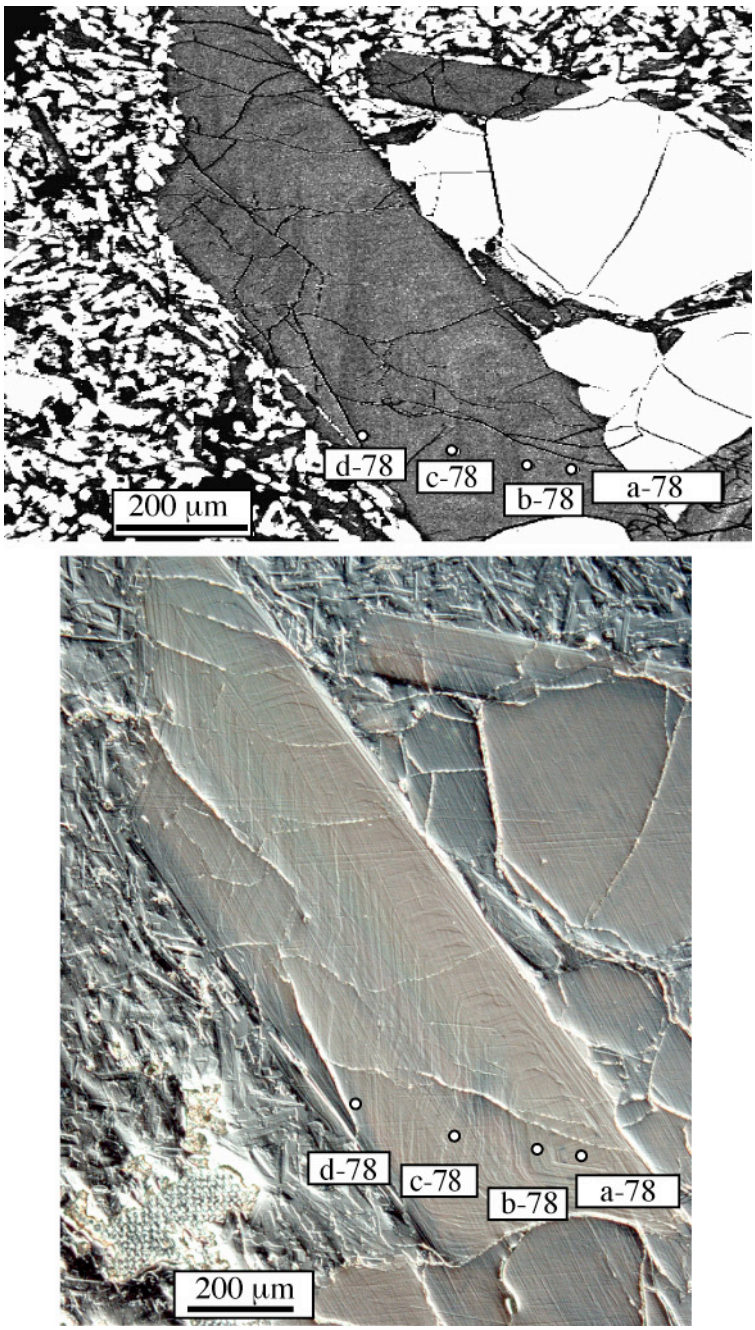

Figure 2. Location of EMP analyses of plagioclase crystal 302-10 from Cave sample SC99-302. Upper is back-scattered electron image, lower is NDIC optical image. Letters reference analysis name for each crystal.

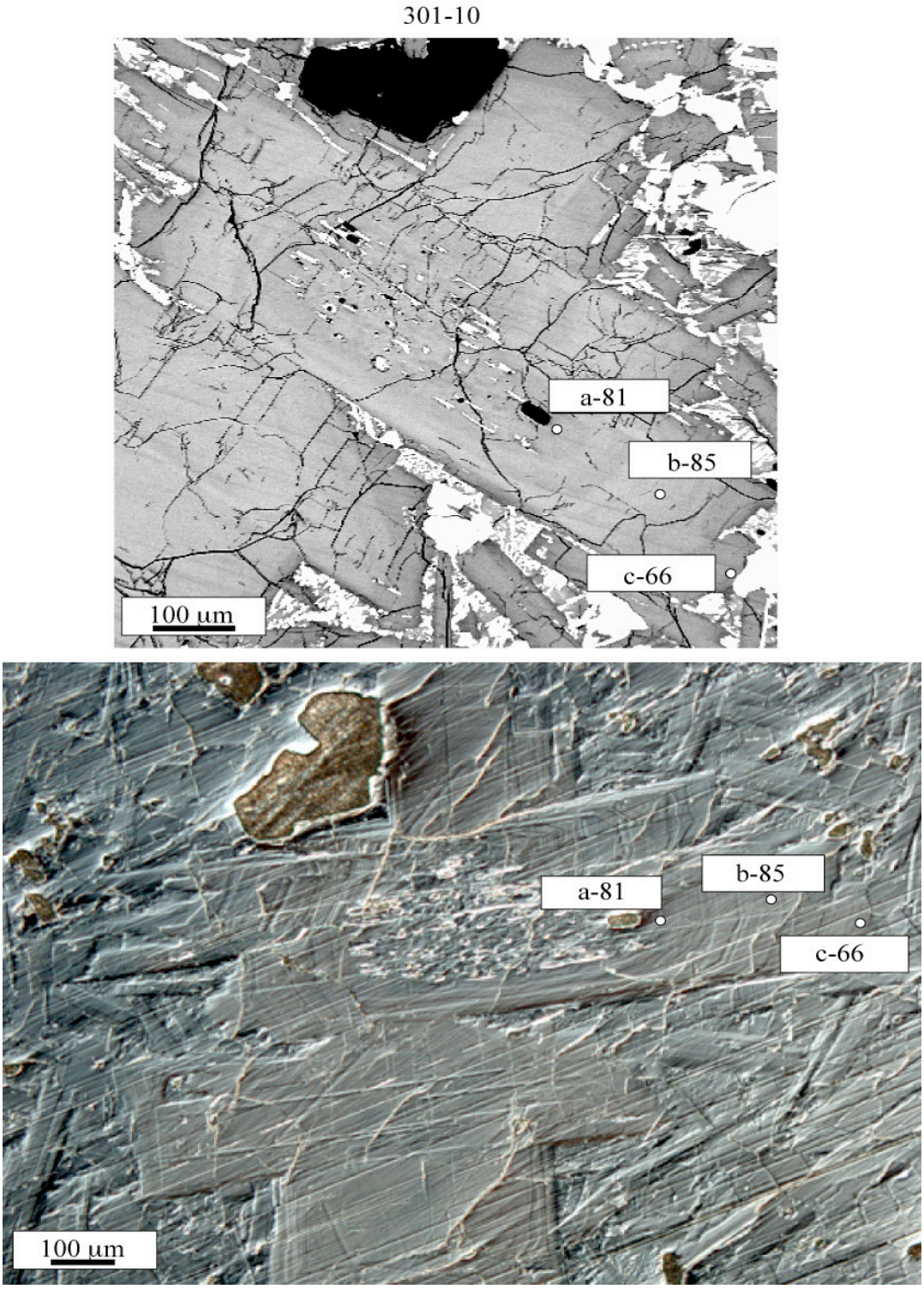

Figure 3. Location of EMP analysis of plagioclase crystal 301-10 from Precave sample SC99-301. Upper is back-scattered electron image, lower is NDIC optical image.

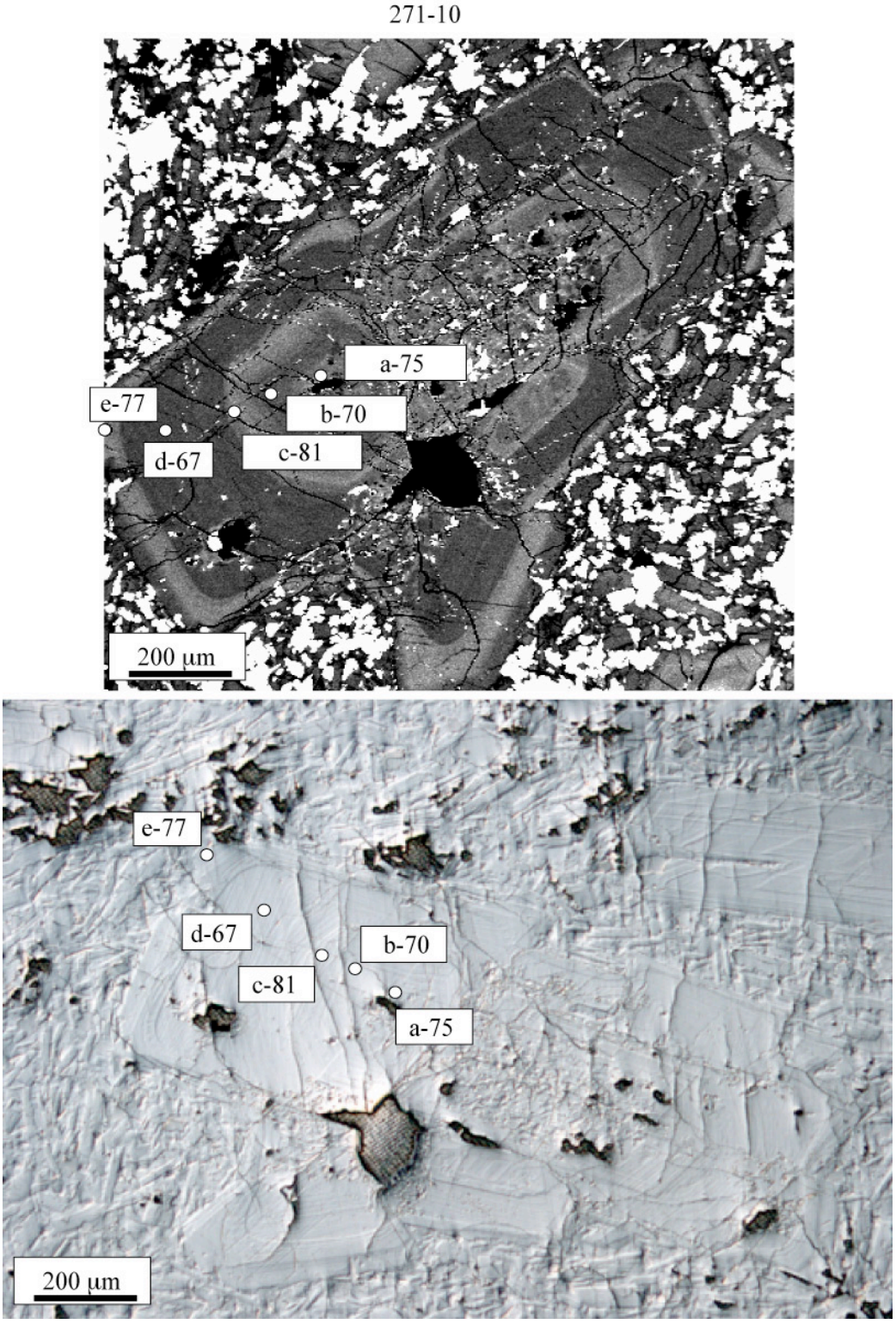

Figure 4. Location of EMP analysis of plagioclase crystal 271-10 from Precave basalt sample SC98-271. Upper is back-scattered electron image, lower is NDIC optical image.

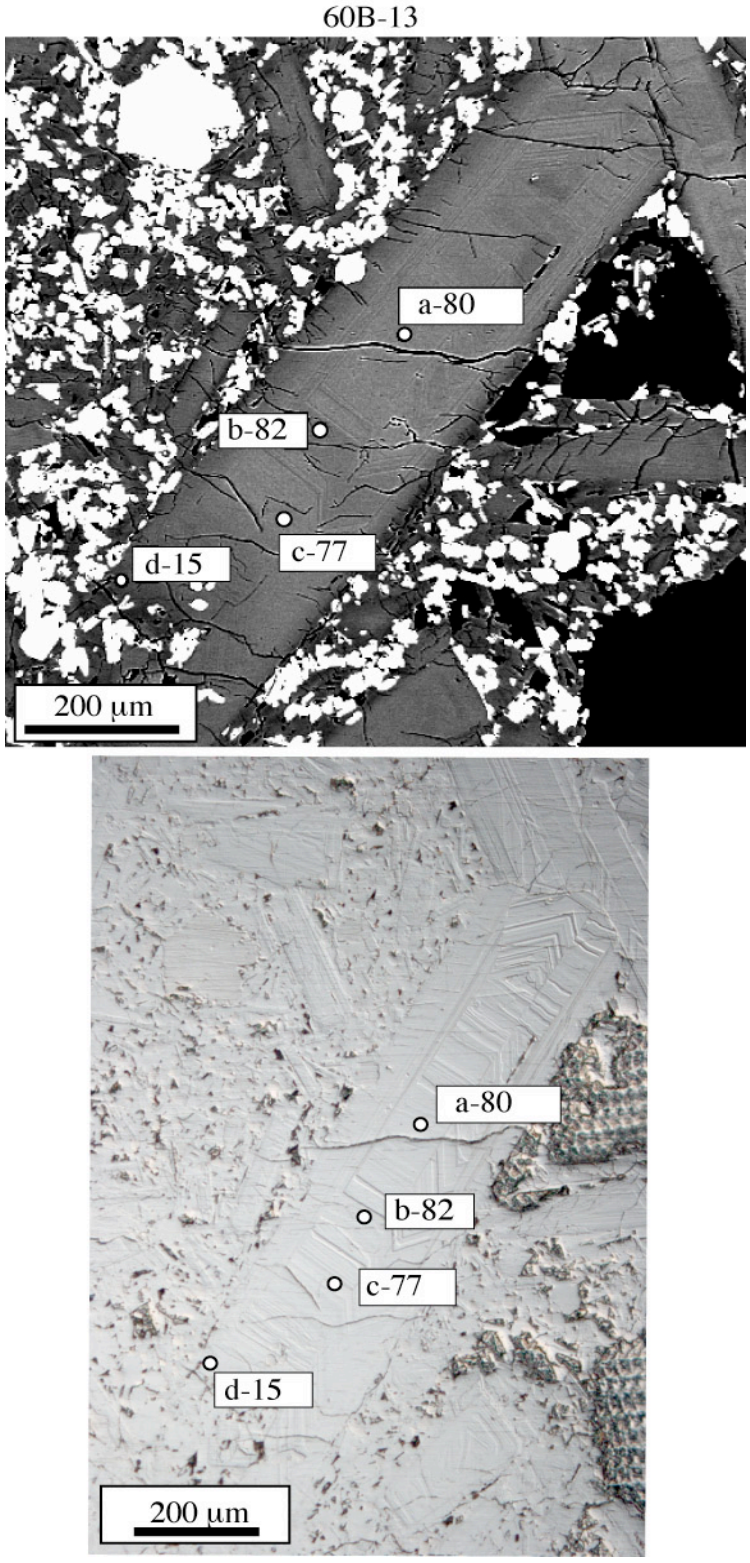

Figure 5. Location of EMP analysis of plagioclase crystal 60B-13 from North Flank basalt sample W95-60B. Upper is back-scattered electron image, lower is NDIC optical image.

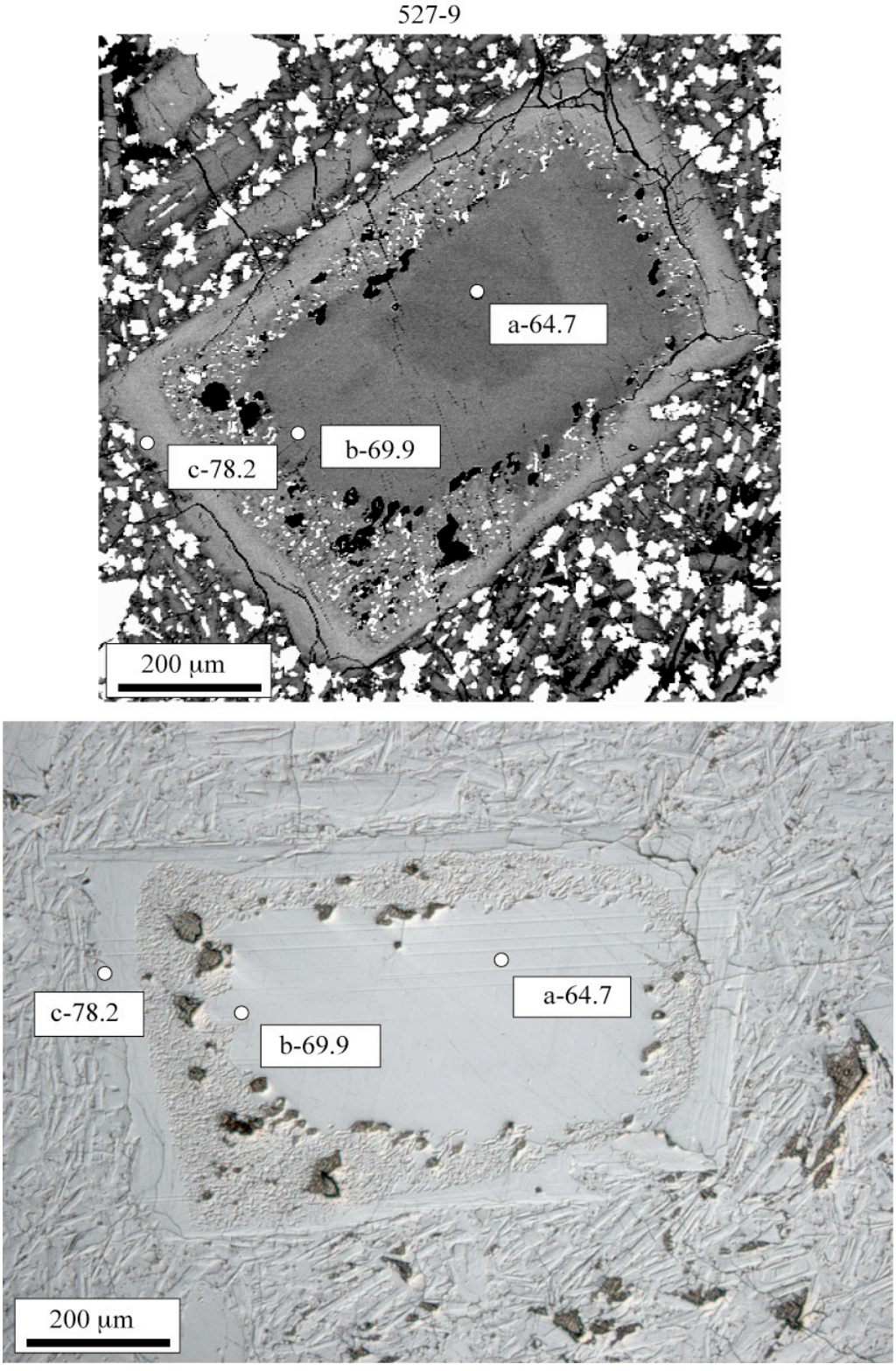

Figure 6. ocation of EMP analyses of plagioclase crystal 527-9 from North Flank sample SC02-527. Upper is back-scattered electron image, lower is NDIC optical image.

Whole-Rock Chemistry

Whole-rock major and trace element chemistry for 86 samples of Castle Creek eruptive products were either compiled or collected for this thesis. Seventeen samples were analyzed for this study, 26 were taken from unpublished works of J. Gardner, 6 from unpublished works of R. Hoblitt, 1 from Halliday et al. (1983), 19 from unpublished works of J. Pallister, and the remaining 17 from the work of Smith and Leeman (1993). Unpublished data were provided by M. Clynne. Whole-rock major and trace element data are available in Tables 8 and 9, respectively.

Oxide-oxide variation diagrams are plotted for all major elements and select trace elements with MgO concentration in wt% on the x-axis and appear in Figures 7 through 13. The five groups of eruptive products addressed in this study (Cave basalt, Precave basalt, North Flank basalt, Castle Creek andesite, Castle Creek dacite) are chemically distinguishable in most diagrams.

Cave basalt forms a limited clustering of data points between 6 and 7 wt% Mg. Precave basalt data, in many instances, form a compositionally intermediate field between the Cave basalt and the North Flank basalt. Cave basalt MgO values are roughly between 5 and 6.5 wt% MgO, and MgO-oxide trends have a variety of geometric relationships with respect to the other two basalt fields. TiO_2 versus MgO, for example, displays a nearly horizontal linear relationship between Cave and Precave data points while maintaining a nearly orthogonal relationship with North Flank data. North Flank data span an MgO range between 4.5 and 7.5 wt %. Compared to Cave basalt samples with comparable MgO, North Flank samples are typically enriched in other oxides and

TABLE 8. CASTLE CREEK WHOLE-ROCK MAJOR ELEMENT CHEMISTRY BY XRF (WT% OXIDE)

Sample	SiO_2	Al_2O_3	MgO	FeO*	CaO	Na_2O	TiO_2	K_2O	P_2O_5	Total
Cave basalts										
SC99-302	50.18	17.16	6.95	9.99	9.64	3.47	1.50	0.49	0.22	99.60
SC99-300	50.37	17.15	6.32	10.16	9.76	3.46	1.59	0.57	0.23	99.61
P85827-2	50.12	17.30	6.63	10.33	9.97	3.36	1.60	0.51	0.20	85.02
P85827-3	50.12	17.24	6.91	10.06	9.88	3.38	1.51	0.49	0.19	84.78
P85827-4	50.16	17.21	6.90	9.96	9.94	3.33	1.50	0.49	0.19	84.68
H85-10	50.34	17.14	6.46	10.14	9.93	3.30	1.55	0.55	0.20	99.61
P85827-1	50.52	16.64	6.29	10.49	9.68	3.43	1.68	0.64	0.23	99.60
H79-3-1	50.62	17.31	6.35	9.81	9.57	3.47	1.60	0.66	0.22	99.61
DS-27	48.57	17.47	6.57	11.56	9.58	3.65	1.47	0.56	0.15	99.58
L82-56	51.17	-	6.17	-	-	-	1.55	0.65	-	59.54
Precave basalts										
W99-178	51.19	17.21	6.15	9.62	9.33	3.59	1.60	0.70	0.25	99.64
SC99-301	51.28	17.04	6.01	9.74	9.35	3.62	1.62	0.70	0.27	99.63
SC98-271	52.26	17.15	5.48	9.35	8.88	3.70	1.69	0.85	0.28	99.64
W01-212	53.63	16.63	6.09	8.68	7.65	3.92	1.61	1.07	0.38	99.66
SC04-683	54.05	17.17	6.16	8.34	8.18	3.88	1.44	1.03	0.27	100.52
G850826-1	52.43	16.88	5.43	9.35	9.01	3.72	1.69	0.86	0.28	99.65
P90-42	52.61	17.00	5.34	9.14	8.87	3.77	1.70	0.90	0.30	99.63
P794-3B	52.75	-	6.16	-	-	-	1.67	0.97	-	61.55
P90-40	52.78	17.03	5.18	9.10	8.79	3.84	1.70	0.92	0.33	99.67
P90-8B	53.01	16.90	5.52	8.94	8.51	3.80	1.69	0.96	0.33	99.66
P90-8C	53.01	17.03	5.19	9.03	8.61	3.81	1.71	0.95	0.32	99.66
P90-8A	53.06	16.82	5.52	8.92	8.53	3.86	1.68	0.95	0.32	99.66
H85-11-2	53.07	16.82	5.47	9.01	8.55	3.76	1.69	0.96	0.32	99.65
P90-23	53.20	16.53	6.29	8.87	7.90	3.85	1.62	1.04	0.35	99.65
H85-11-1	53.25	17.18	4.92	8.88	8.73	3.75	1.72	0.93	0.31	99.67
H85-15	53.32	16.77	5.68	8.88	8.28	3.78	1.65	1.01	0.29	99.66
L82-40	53.57	16.53	6.13	8.88	7.67	3.90	1.61	1.05	0.32	99.66
L82-41A	53.58	16.63	6.04	8.88	7.70	3.86	1.62	1.04	0.30	99.65
P794-3A	52.93	-	6.17	-	-	-	1.66	0.96	-	61.72
P794-3C	52.94	-	6.17	-	-	-	1.65	1.00	-	61.76
North Flank Basalts										
W95-60B	49.76	16.62	7.40	9.25	8.85	3.79	2.09	1.40	0.50	99.66
SC03-636	51.62	17.14	6.73	8.85	8.42	3.74	1.77	1.00	0.39	99.66
SC02-509	51.67	17.36	6.31	8.55	8.54	3.94	1.74	1.16	0.42	99.69
SC04-639	51.76	16.95	6.77	9.08	8.30	3.70	1.75	0.97	0.38	99.66
SC03-635	52.28	17.63	6.09	8.58	8.32	3.88	1.57	0.99	0.33	99.67

TABLE 8. (continued)

Sample	SiO_2	Al_2O_3	MgO	FeO*	CaO	Na_2O	TiO_2	K_2O	P_2O_5	Total
North Flank Basalts										
SC02-527	52.48	17.93	5.78	8.42	8.24	4.01	1.51	0.98	0.32	99.67
W00-197	52.81	16.93	6.16	8.99	8.20	3.57	1.68	1.00	0.32	99.66
W02-230	53.39	17.22	6.06	8.41	8.10	3.74	1.44	1.02	0.29	99.67
SC04-664	55.01	16.97	4.96	8.31	7.78	4.02	1.49	1.03	0.26	99.84
SC04-701	49.40	16.38	6.61	8.18	8.18	3.78	1.63	1.08	0.35	95.59
DS-5	49.29	16.88	7.16	10.02	8.70	3.89	2.00	1.26	0.44	99.64
DS-6	49.91	16.83	6.61	10.02	8.62	3.88	2.04	1.31	0.41	99.63
DS-9	48.93	16.67	6.67	11.01	8.71	3.78	2.10	1.36	0.37	99.60
DS-7	49.95	16.26	6.83	10.42	8.54	3.90	1.98	1.34	0.38	99.60
G850817-1	50.01	16.77	6.89	9.61	9.03	3.64	2.01	1.24	0.42	99.62
G850817-2	50.02	16.64	7.01	9.60	8.96	3.73	2.02	1.24	0.42	99.64
H85-5-1	50.03	16.68	6.82	9.11	9.08	3.81	2.16	1.45	0.51	99.65
DS-77	50.93	17.64	6.16	9.94	7.98	4.22	1.56	0.97	0.25	99.65
MSH6-8	51.37	17.09	6.65	8.76	8.69	3.90	1.74	1.09	0.38	99.67
L82-63	51.38	17.17	6.77	8.91	8.37	3.80	1.83	1.09	0.33	99.65
P793-2	51.41	17.04	6.74	8.78	8.65	3.82	1.72	1.11	0.39	99.66
MSH6-4	51.45	17.15	6.71	8.85	8.63	3.77	1.71	1.05	0.35	99.67
G850816-2	51.48	17.03	6.64	8.72	8.66	3.88	1.74	1.12	0.39	99.66
MSH6-6	51.52	17.04	6.65	8.80	8.66	3.81	1.73	1.08	0.37	99.66
MSH6-7	51.54	17.08	6.57	8.76	8.67	3.84	1.74	1.10	0.38	99.68
P793-4A	51.57	17.12	6.44	8.86	8.64	3.89	1.71	1.07	0.36	99.66
G850819-1	51.64	16.98	6.63	8.77	8.60	3.81	1.74	1.12	0.38	99.67
G850813-1	51.70	17.07	6.50	8.70	8.61	3.83	1.75	1.13	0.38	99.67
DS-4	51.72	17.72	6.18	8.43	8.29	4.24	1.73	1.17	0.20	99.68
P793-4B	51.95	-	6.30	-	-	-	1.68	1.05	-	60.98
DS-71	52.07	18.32	5.20	9.42	7.99	4.25	1.23	0.95	0.25	99.68
P793-4C	52.11	17.34	5.90	8.73	8.59	3.93	1.68	1.05	0.34	99.67
DS-78	52.14	17.28	5.88	9.56	7.93	4.03	1.54	1.00	0.29	99.65
P793-4D	52.23	17.21	6.04	8.81	8.46	3.88	1.66	1.04	0.33	99.66
P793-4E	52.24	17.11	6.08	8.82	8.44	3.96	1.65	1.03	0.33	99.66
DS-76	52.39	18.21	5.15	9.31	7.70	4.27	1.40	1.02	0.20	99.65
DS-72	52.95	18.33	5.46	8.14	7.96	4.26	1.43	0.99	0.17	99.69
DS-74	53.62	18.69	4.46	8.55	7.37	4.42	1.30	1.04	0.25	99.70

TABLE 8. (continued)

Sample	SiO_2	Al_2O_3	MgO	FeO*	CaO	Na_2O	TiO_2	K_2O	P_2O_5	Total
Castle Creek andesites (Steps, Loowit, W-74)										
G850823-2	56.18	16.80	5.18	7.65	7.63	3.82	1.18	1.03	0.23	99.70
G850813-2	56.57	17.29	4.39	7.46	7.32	4.03	1.27	1.13	0.26	99.72
G850816-1	56.70	17.17	4.45	7.43	7.28	4.02	1.26	1.14	0.27	99.72
G850819-2	57.21	17.07	4.15	7.48	6.98	4.01	1.31	1.21	0.29	99.71
G850823-1	60.85	17.08	2.64	6.41	5.86	4.26	1.05	1.36	0.25	99.76
MSH6-2	62.19	16.66	1.92	6.40	5.31	4.52	1.09	1.46	0.21	99.76
MSH6-11	57.16	16.69	3.47	8.34	6.89	4.28	1.48	1.12	0.26	99.69
G850825-1	59.09	16.60	2.33	7.78	6.08	4.65	1.54	1.32	0.31	99.70
Castle Creek dacites										
SHH-20	62.87	17.57	2.19	4.81	5.26	4.68	0.76	1.46	0.21	99.81
MSH6-16	64.30	16.65	1.98	4.98	4.83	4.42	0.81	1.64	0.20	99.81
MSH6-10	64.64	16.31	1.49	5.49	4.48	4.66	0.79	1.69	0.22	99.77
MSH6-12	64.75	16.24	1.49	5.51	4.45	4.64	0.77	1.70	0.22	99.77
MSH6-15	64.99	16.32	1.44	5.23	4.46	4.70	0.74	1.70	0.22	99.80
MSH6-14	65.31	17.01	1.81	4.26	4.68	4.41	0.68	1.52	0.15	99.83
MSH6-1	65.41	16.88	1.75	4.19	4.64	4.61	0.67	1.55	0.15	99.85
MSH6-5	65.41	16.96	1.74	4.18	4.63	4.56	0.68	1.55	0.14	99.85
MSH6-3	65.63	16.89	1.71	4.15	4.58	4.53	0.67	1.56	0.14	99.86

elements. For example, North Flank sample SC02-509 contains 6.31 wt% MgO, comparable to sample SC99-300 of the Cave basalt which has 6.32 wt% MgO. In contrast, Sample SC02-509 contains 1.16 wt% K_2O and 588 ppm Sr, whereas SC99-300 has 0.57 wt% K_2O and 319 ppm Sr. While this alone distinguishes Cave samples from North Flank samples in many cases, the North Flank data also manifest trends that show decreasing concentrations of incompatible elements with decreasing MgO. For example, abundances of K_2O decrease with decreasing values of MgO. This trend holds true for incompatible trace elements as well. Andesite data from the Castle Creek eruptive period form a data array that bridges the compositional gap between basalts and dacites in

TABLE 9. CASTLE CREEK WHOLE-ROCK TRACE ELEMENT ANALYSES BY ICP-MS (PPM)

	Cave basalt						
	SC99-302	SC99-300	P85827-2	P85827-3	P85827-4	H85-10	P85827-1
Cs	0.35	0.39	0.31	0.35	0.37	0.37	0.40
Rb	9.43	10.52	10.40	8.97	9.59	10.70	13.30
Sr	332.04	319.09	334.00	346.00	360.00	343.00	349.00
Ba	115.11	134.45	106.00	118.00	113.00	120.00	138.00
Pr	2.63	2.88	-	-	-	-	-
Dy	4.89	5.32	-	-	-	-	-
Ho	0.99	1.08	-	-	-	-	-
Er	2.66	2.94	-	-	-	-	-
Hf	2.92	3.09	2.76	2.67	2.74	2.88	2.99
Zr	112.90	118.97	115.00	114.00	111.00	109.00	130.00
Ta	0.48	0.57	0.48	0.47	0.46	0.53	0.59
Nb	7.42	8.99	10.00	10.00	15.00	10.00	10.00
Y	26.02	28.23	25.00	22.00	26.00	26.00	28.00
Th	0.97	1.09	0.84	0.85	0.83	0.86	1.05
U	0.35	0.41	0.31	0.39	0.05	0.39	0.42
Pb	1.92	2.14	-	-	-	-	-
La	8.68	9.78	8.15	7.91	7.78	8.36	9.48
Ce	19.60	21.70	19.80	20.00	19.30	21.00	23.70
Nd	12.76	13.85	13.00	11.50	12.80	13.60	14.00
Sm	3.86	4.23	3.73	3.74	3.74	3.75	4.16
Eu	1.41	1.50	1.34	1.30	1.30	1.30	1.38
Gd	4.59	4.95	4.51	4.32	4.42	4.48	4.92
Tb	0.78	0.84	0.71	0.70	0.68	0.71	0.75
Tm	0.38	0.42	0.38	0.38	0.39	0.39	0.40
Yb	2.29	2.54	2.32	2.36	2.26	2.44	2.47
Lu	0.35	0.40	0.34	0.34	0.34	0.35	0.37

TABLE 9. (continued)

	P90-8A	H85-11-2	P90-23	H85-11-1	H85-15	L82-40	L82-41A	H79-3-1
Cs	0.42	0.58	0.69	0.55	0.78	-	0.57	0.46
Rb	18.80	17.50	19.90	19.40	23.80	22.00	22.00	14.70
Sr	459.00	477.00	469.00	462.00	501.00	476.00	468.00	340.00
Ba	261.00	228.00	290.00	231.00	223.00	-	-	161.00
Pr	-	-	-	-	-	-	-	-
Dy	-	-	-	-	-	-	-	-
Ho	-	-	-	-	-	-	-	-
Er	-	-	-	-	-	-	-	-
Hf	4.12	3.98	4.12	4.01	3.69		4.20	3.07
Zr	192.00	141.00	185.00	135.00	153.00	181.00	178.00	120.00
Ta	1.09	1.03	1.18	1.01	0.93		0.95	0.61
Nb	-	19.00	-	18.00	15.00	18.00	18.00	10.00
Y	-	27.00	-	23.00	27.00	28.00	26.00	22.00
Th	1.89	1.72	1.97	1.82	1.75	-	2.10	1.15
U	0.65	0.62	0.81	0.62	0.71	-	-	0.05
Pb	-	-	-	-	-	7.00	10.00	-
La	16.60	14.90	17.30	14.90	13.50	-	15.60	10.10
Ce	40.30	34.70	41.80	34.40	34.00	-	37.00	24.30
Nd	22.20	20.30	22.70	20.40	18.90	-		14.50
Sm	5.32	4.99	5.42	5.17	4.83	-	4.83	3.77
Eu	1.68	1.61	1.66	1.69	1.52	-	1.53	1.31
Gd	5.55	5.40	5.21	5.18	5.10	-		4.20
Tb	0.78	0.80	0.74	0.85	0.76	-	0.82	0.66
Tm	0.39	0.39	0.38	0.42	0.36	-	-	0.41
Yb	2.53	2.35	2.34	2.51	2.15	-	2.23	2.45
Lu	0.37	0.35	0.35	0.39	0.31	-	0.34	0.39

TABLE 9. (continued)

	Precave basalt							
	DS-27	L82-56	W99-178	SC99-301	SC98-271	W01-212	SC04-683	G850826-1
Cs	0.36	0.38	0.50	0.48	0.59	0.73	0.62	0.51
Rb	11.00	15.00	13.70	13.58	16.48	21.26	18.20	17.80
Sr	321.00	363.00	366.47	359.22	407.29	480.58	442.08	419.00
Ba	118.00	-	171.73	170.70	209.19	272.66	245.19	202.00
Pr	-	-	3.38	3.36	3.86	4.47	4.41	-
Dy	-	-	5.38	5.33	5.47	5.13	5.32	-
Ho	-	-	1.10	1.10	1.10	1.00	1.06	-
Er	-	-	2.87	2.90	2.89	2.60	2.78	-
Hf	3.00	3.20	3.54	3.49	3.87	4.22	4.17	3.44
Zr	132.00	139.00	133.85	132.09	148.71	163.17	156.79	140.00
Ta	0.57	0.56	0.70	0.71	0.85	1.10	1.03	0.82
Nb	8.70	11.00	11.06	10.96	13.31	17.52	15.63	14.00
Y	23.00	27.00	28.60	28.35	28.77	26.34	27.29	27.00
Th	0.94	1.40	1.41	1.38	1.72	2.21	1.91	1.52
U	-	-	0.52	0.49	0.59	0.78	0.70	0.57
Pb	5.00	6.00	2.74	2.71	3.27	4.13	3.68	-
La	8.10	10.20	11.91	11.86	14.19	17.44	16.49	13.00
Ce	21.10	25.00	25.91	25.66	30.23	36.11	34.60	29.10
Nd	-	-	15.73	15.50	17.84	19.95	19.78	16.80
Sm	3.51	4.02	4.57	4.55	5.00	5.27	5.29	4.68
Eu	1.29	1.32	1.57	1.58	1.69	1.75	1.74	1.52
Gd	-	-	5.19	5.15	5.33	5.30	5.43	4.98
Tb	0.69	0.77	0.87	0.87	0.90	0.86	0.89	0.78
Tm	-	-	0.43	0.42	0.42	0.36	0.40	0.41
Yb	2.35	2.41	2.53	2.49	2.52	2.20	2.36	2.38
Lu	0.33	0.38	0.40	0.39	0.39	0.34	0.37	0.36

TABLE 9. (continued)

	P90-42	P794-3B	P90-40	P90-8B	P90-8C	P794-3A	P794-3C
Cs	0.60	0.60	0.57	0.64	0.64	0.62	0.69
Rb	17.80	20.70	21.00	20.90	18.70	19.70	26.00
Sr	374.00	456.00	457.00	448.00	430.00	446.00	464.00
Ba	231.00	244.00	241.00	258.00	249.00	266.00	281.00
Pr	-	-	-	-	-	-	-
Dy	-	-	-	-	-	-	-
Ho	-	-	-	-	-	-	-
Er	-	-	-	-	-	-	-
Hf	4.02	4.32	3.92	4.13	4.16	4.19	4.27
Zr	162.00	146.00	164.00	175.00	193.00	179.00	179.00
Ta	0.97	1.18	0.99	1.09	1.08	1.16	1.23
Nb	-	-	-	-	-	-	-
Y	-	-	-	-	-	-	-
Th	1.69	1.98	1.73	1.83	1.85	1.90	2.02
U	0.63	0.88	0.67	0.76	0.74	0.67	0.76
Pb	-	-	-	-	-	-	-
La	15.60	17.50	15.40	16.70	16.40	17.20	17.90
Ce	37.50	41.80	37.30	40.40	41.30	41.00	45.40
Nd	20.70	22.80	20.90	22.10	22.00	21.90	22.50
Sm	5.13	5.82	5.05	5.31	5.47	5.55	5.76
Eu	1.65	1.74	1.59	1.68	1.67	1.73	1.75
Gd	5.44	5.89	5.26	5.25	5.33	5.81	5.99
Tb	0.81	0.85	0.80	0.80	0.80	0.83	0.88
Tm	0.42	0.41	0.44	0.40	0.43	-	0.44
Yb	2.60	2.63	2.67	2.51	2.66	2.45	2.61
Lu	0.39	0.37	0.39	0.38	0.39	0.35	0.37

TABLE 9. (continued)

	North Flank basalts							
	W95-60B	SC03-636	SC02-509	SC04-639	SC03-635	SC02-527	W00-197	W02-230
Cs	0.62	0.40	0.44	0.45	0.62	0.58	0.73	0.82
Rb	24.09	17.10	22.15	16.80	20.32	20.13	19.27	19.19
Sr	659.84	547.32	587.69	516.18	543.68	536.82	489.33	476.11
Ba	330.24	262.84	278.20	255.62	223.34	217.84	221.48	208.28
Pr	5.84	4.51	5.00	4.36	4.05	3.90	4.00	3.64
Dy	5.10	4.61	4.82	4.79	4.57	4.23	5.06	4.55
Ho	1.01	0.88	0.93	0.92	0.90	0.86	0.99	0.91
Er	2.56	2.17	2.43	2.34	2.32	2.20	2.61	2.40
Hf	4.53	3.77	4.10	3.84	3.71	3.56	3.89	3.64
Zr	191.69	149.12	167.75	149.31	149.92	140.91	155.64	148.05
Ta	2.20	1.37	1.32	1.26	0.91	0.79	0.97	0.78
Nb	34.28	21.36	20.60	19.47	13.76	12.25	15.15	11.75
Y	26.25	22.48	24.67	23.75	23.47	22.06	25.87	23.54
Th	2.84	1.94	2.33	1.89	1.85	1.79	1.90	1.84
U	0.93	0.61	0.76	0.62	0.67	0.68	0.73	0.73
Pb	2.85	2.81	3.35	2.97	3.42	3.64	3.76	3.92
La	24.62	18.01	20.13	17.20	15.51	14.69	15.24	13.90
Ce	48.78	36.76	40.91	35.30	32.66	31.14	32.01	29.07
Nd	24.96	20.05	21.96	19.69	18.12	17.28	18.15	16.04
Sm	5.97	5.18	5.43	5.21	4.73	4.46	4.90	4.35
Eu	2.02	1.77	1.83	1.75	1.62	1.57	1.66	1.50
Gd	5.77	5.08	5.31	5.29	4.77	4.68	5.09	4.63
Tb	0.89	0.81	0.82	0.82	0.76	0.73	0.84	0.76
Tm	0.36	0.31	0.33	0.32	0.33	0.31	0.36	0.34
Yb	2.12	1.80	1.98	1.93	1.95	1.92	2.25	2.06
Lu	0.33	0.27	0.31	0.29	0.31	0.30	0.34	0.33

TABLE 9. (continued)

	SC04-664	SC04-701	DS-5	DS-6	DS-9	DS-7	G850817-1	G850817-2
Cs	0.96	0.52	0.18	0.25	0.61	0.60	0.30	0.25
Rb	22.12	22.00	27.00	25.00	24.00	27.00	19.00	18.60
Sr	456.22	613.59	589.00	620.00	590.00	577.00	605.00	594.00
Ba	232.69	267.41	272.00	316.00	312.00	319.00	240.00	254.00
Pr	3.75	4.81	-	-	-	-	-	-
Dy	4.86	4.71	-	-	-	-	-	-
Ho	0.97	0.91	-	-	-	-	-	-
Er	2.54	2.36	-	-	-	-	-	-
Hf	3.85	4.00	4.30	4.30	4.50	4.40	3.92	3.99
Zr	147.84	165.30	207.00	203.00	200.00	203.00	148.00	170.00
Ta	0.74	1.26	2.30	2.35	2.13	2.07	1.57	1.65
Nb	11.02	19.51	-	32.70	28.50	-	27.00	25.00
Y	25.21	24.18	-	34.90	26.20	-	27.00	25.00
Th	1.86	2.17	2.60	2.47	2.26	2.22	1.95	2.02
U	0.76	0.73	-	-	-	0.59	0.67	0.66
Pb	4.64	3.16	-	5.00	8.00	-	-	-
La	14.00	19.09	22.70	21.20	19.80	19.80	19.00	19.20
Ce	29.58	39.29	47.50	45.30	45.70	44.20	40.10	41.50
Nd	16.95	21.14	-	-	-	-	20.30	21.60
Sm	4.70	5.25	5.85	5.53	5.25	5.30	4.75	5.20
Eu	1.57	1.80	1.85	1.79	1.80	1.74	1.69	1.73
Gd	4.92	5.06	-	-	-	-	5.34	5.58
Tb	0.80	0.80	0.77	0.74	0.78	0.73	0.77	0.77
Tm	0.37	0.33	-	-	-	-	-	0.37
Yb	2.22	1.99	2.20	2.11	2.20	2.08	2.18	2.23
Lu	0.35	0.31	0.31	0.33	0.30	0.33	0.33	0.33

TABLE 9. (continued)

	H85-5-1	DS-77	MSH6-8	L82-63	P793-2	MSH6-4	G850816-2	MSH6-6
Cs	0.50	-	0.55	-	0.55	0.64	0.54	0.56
Rb	24.70	-	22.50	20.00	23.90	23.70	23.50	23.00
Sr	681.00	493.00	562.00	574.00	557.00	598.00	609.00	560.00
Ba	316.00	221.00	270.00	-	284.00	241.00	272.00	250.00
Pr	-	-	-	-	-	-	-	-
Dy	-	-	-	-	-	-	-	-
Ho	-	-	-	-	-	-	-	-
Er	-	-	-	-	-	-	-	-
Hf	4.10		4.01		3.98	3.97	3.80	3.86
Zr	170.00	170.00	190.00	176.00	181.00	182.00	150.00	185.00
Ta	2.09	-	1.35		1.34	1.25	1.31	1.19
Nb	35.00	-	20.00	24.00	-	20.00	22.00	20.00
Y	23.00	-	22.00	21.00	-	27.00	22.00	22.00
Th	2.50	-	2.17	-	2.14	2.06	2.15	2.02
U	0.75	-	0.60	-	0.73	0.84	0.70	0.78
Pb	-	-		8.00	-	-	-	-
La	22.30	-	18.60	-	18.50	17.40	18.10	17.60
Ce	48.30	-	44.80	-	44.70	41.50	40.00	41.40
Nd	24.60	-	22.60	-	24.40	21.70	20.30	22.50
Sm	5.65	-	5.13	-	5.42	4.91	4.99	4.79
Eu	1.85	-	1.72	-	1.72	1.69	1.64	1.62
Gd	5.53	-	5.11	-	5.22	5.17	4.92	4.83
Tb	0.80	-	0.76	-	0.72	0.76	0.73	0.69
Tm	0.36	-	0.36	-	0.35	0.36		0.34
Yb	2.10	-	2.17	-	2.01	2.12	1.93	2.06
Lu	0.30	-	0.32	-	0.30	0.31	0.28	0.27

TABLE 9. (continued)

	MSH6-7	P793-4A	G850819-1	G850813-1	DS-4	P793-4B	DS-71	P793-4C
Cs	0.42	0.65	0.46	0.48	0.56	0.69	0.46	0.77
Rb	23.00	26.60	22.60	24.30	25.00	24.70	19.00	25.90
Sr	516.00	658.00	597.00	605.00	581.00	585.00	511.00	676.00
Ba	263.00	288.00	255.00	283.00	275.00	247.00	216.00	285.00
Pr	-	-	-	-	-	-	-	-
Dy	-	-	-	-	-	-	-	-
Ho	-	-	-	-	-	-	-	-
Er	-	-	-	-	-	-	-	-
Hf	3.82	4.35	3.74	3.79	4.10	3.97	3.60	4.48
Zr	187.00	183.00	143.00	140.00	188.00	158.00	156.00	174.00
Ta	1.20	1.33	1.25	1.25	1.41	1.08	0.80	1.29
Nb	20.00	-	22.00	18.00	21.80	-	-	-
Y	20.00	-	27.00	21.00	17.50	-	-	-
Th	2.09	2.23	2.11	2.08	2.05	1.93	1.54	2.18
U	0.79	0.98	0.72	0.69	0.61	0.79	0.26	1.03
Pb	-	-	-	-	10.00	-	-	-
La	17.90	18.80	17.90	17.70	10.80	16.50	10.00	18.40
Ce	38.90	45.70	38.60	39.20	26.30	39.10	24.40	44.90
Nd	22.80	24.30	21.10	20.40	-	21.80	-	24.30
Sm	4.83	5.88	4.93	4.75	3.31	5.21	3.24	6.00
Eu	1.63	1.76	1.58	1.60	1.36	1.62	1.26	1.80
Gd	4.88	5.38	4.77	4.93	-	4.79	-	5.50
Tb	0.73	0.81	0.71	0.69	0.59	0.73	0.48	0.83
Tm	0.36	0.38	0.34	0.34	-	0.37	-	-
Yb	2.14	2.30	2.04	1.98	1.69	2.13	1.68	2.40
Lu	0.27	0.32	0.30	0.28	0.25	0.31	0.25	0.34

TABLE 9. (continued)

							CCA	
	DS-78	P793-4D	P793-4E	DS-76	DS-72	DS-74	L82-55	G850823-2
Cs	0.58	0.76	0.59	0.57	0.31	0.51	0.38	0.71
Rb	21.00	27.60	22.40	25.00	23.00	25.00	24.00	20.10
Sr	514.00	678.00	500.00	527.00	528.00	518.00	594.00	465.00
Ba	262.00	285.00	236.00	226.00	225.00	244.00	-	244.00
Pr	-	-	-	-	-	-	-	-
Dy	-	-	-	-	-	-	-	-
Ho	-	-	-	-	-	-	-	-
Er	-	-	-	-	-	-	-	-
Hf	3.90	4.47	3.84	3.60	3.10	3.50	3.70	3.26
Zr	178.00	180.00	163.00	165.00	154.00	153.00	162.00	145.00
Ta	0.96	1.23	1.02	0.80	0.67	0.66	0.86	0.59
Nb	-	-	-	-	12.50	-	17.00	<10
Y	-	-	-	-	21.30	-	16.00	20.00
Th	1.84	2.19	1.83	1.66	1.36	1.64	2.40	1.83
U		0.94	0.82	0.78	0.75	0.94	-	0.71
Pb	-	-	-	-	8.00	-	8.00	-
La	14.30	18.10	16.10	10.90	11.30	10.50	12.40	12.20
Ce	34.90	45.10	39.90	26.70	26.80	24.80	28.00	27.10
Nd	-	24.20	21.30	-	-	-	-	14.70
Sm	4.43	6.04	5.17	3.00	3.42	4.17	3.48	3.68
Eu	1.52	1.80	1.62	1.30	1.21	1.25	1.25	1.23
Gd	-	6.07	4.63	-	-	-	-	3.54
Tb	0.62	0.89	0.72	0.56	0.49	0.48	0.52	0.58
Tm	-	0.43	-	-	-	-	-	0.31
Yb	2.10	2.44	2.19	1.70	1.61	1.68	1.46	1.87
Lu	0.31	0.35	0.32	0.24	0.25	0.24	0.23	0.28

TABLE 9. (continued)

	G850813-2	G850816-1	G850819-2	G850823-1	MSH6-2	MSH6-11	G850825-1	SHH-20
Cs	0.56	0.86	0.43	1.49	1.85	1.13	1.20	2.35
Rb	<10	23.90	24.80	33.10	36.60	26.30	29.20	38.00
Sr	509.00	501.00	504.00	486.00	428.00	416.00	419.00	477.00
Ba	284.00	269.00	298.00	338.00	338.00	256.00	305.00	396.00
Pr	-	-	-	-	-	-	-	-
Dy	-	-	-	-	-	-	-	-
Ho	-	-	-	-	-	-	-	-
Er	-	-	-	-	-	-	-	-
Hf	3.69	3.65	3.70	4.18	4.26	4.05	4.51	4.10
Zr	141.00	141.00	129.00	153.00	164.00	163.00	182.00	150.00
Ta	0.79	0.76	0.80	0.71	0.65	0.74	0.93	1.10
Nb	15.00	11.00	<10	12.00	10.00	12.00	12.00	9.00
Y	26.00	21.00	19.00	20.00	22.00	24.00	27.00	16.00
Th	2.11	2.11	2.26	2.74	2.83	2.05	2.45	3.90
U	0.82	0.76	0.85	1.08	1.12	0.62	0.92	-
Pb	-	-	-	-	-	-	-	-
La	15.10	15.00	16.40	16.20	15.30	13.90	15.80	17.90
Ce	34.10	33.30	34.10	37.10	35.60	34.00	38.40	30.00
Nd	18.10	17.30	17.50	18.90	19.60	20.30	20.60	13.90
Sm	4.15	4.14	4.21	4.25	4.31	4.40	5.25	2.93
Eu	1.34	1.36	1.33	1.32	1.35	1.50	1.66	1.18
Gd	4.25	4.24	3.89	4.17	4.49	4.63	5.65	-
Tb	0.64	0.63	0.65	0.65	0.70	0.74	0.85	0.68
Tm	0.34	0.31	0.29	0.32	0.38	0.42	0.42	-
Yb	2.00	1.76	1.89	1.84	2.23	2.59	2.58	1.40
Lu	0.28	0.29	0.28	0.27	0.33	0.36	0.38	0.22

TABLE 9. (continued)

Castle Creek dacites								
	MSH6-16	MSH6-10	MSH6-12	MSH6-15	MSH6-14	MSH6-1	MSH6-5	MSH6-3
Cs	1.25	2.33	1.05	2.26	2.14	2.26	2.30	2.34
Rb	46.40	45.70	45.10	46.20	43.60	42.90	45.40	44.80
Sr	470.00	412.00	421.00	388.00	442.00	457.00	442.00	464.00
Ba	423.00	429.00	410.00	400.00	403.00	396.00	390.00	425.00
Pr	-	-	-	-	-	-	-	-
Dy	-	-	-	-	-	-	-	-
Ho	-	-	-	-	-	-	-	-
Er	-	-	-	-	-	-	-	-
Hf	4.55	5.24	5.19	4.92	3.38	3.43	3.42	3.52
Zr	174.00	219.00	202.00	204.00	126.00	133.00	125.00	134.00
Ta	0.74	0.74	0.75	0.69	0.47	0.47	0.45	0.49
Nb	10.00	10.00	12.00	10.00	< 10	< 10	< 10	< 10
Y	18.00	26.00	26.00	25.00	14.00	14.00	15.00	14.00
Th	3.55	3.40	3.39	3.29	2.87	3.00	2.99	3.04
U	1.33	1.41	1.54	1.34	1.32	1.47	1.40	1.33
Pb	-	-	-	-	-	-	-	-
La	18.00	17.40	18.10	17.00	13.40	13.10	13.00	13.30
Ce	40.90	41.90	44.40	40.30	29.30	30.40	28.30	29.90
Nd	20.60	22.50	23.50	21.20	14.70	14.70	15.30	15.60
Sm	4.13	4.87	5.18	4.69	3.05	3.16	3.07	3.14
Eu	1.21	1.44	1.42	1.33	0.95	0.94	0.94	0.98
Gd	4.34	5.09	5.46	4.98	2.91	3.08	3.01	3.10
Tb	0.63	0.81	0.84	0.77	0.45	0.44	0.44	0.45
Tm	0.31	0.45	0.43	0.42	0.22	0.23	0.23	0.23
Yb	1.93	2.77	2.55	2.51	1.37	1.41	1.36	1.43
Lu	0.28	0.38	0.39	0.37	0.20	0.20	0.20	0.21

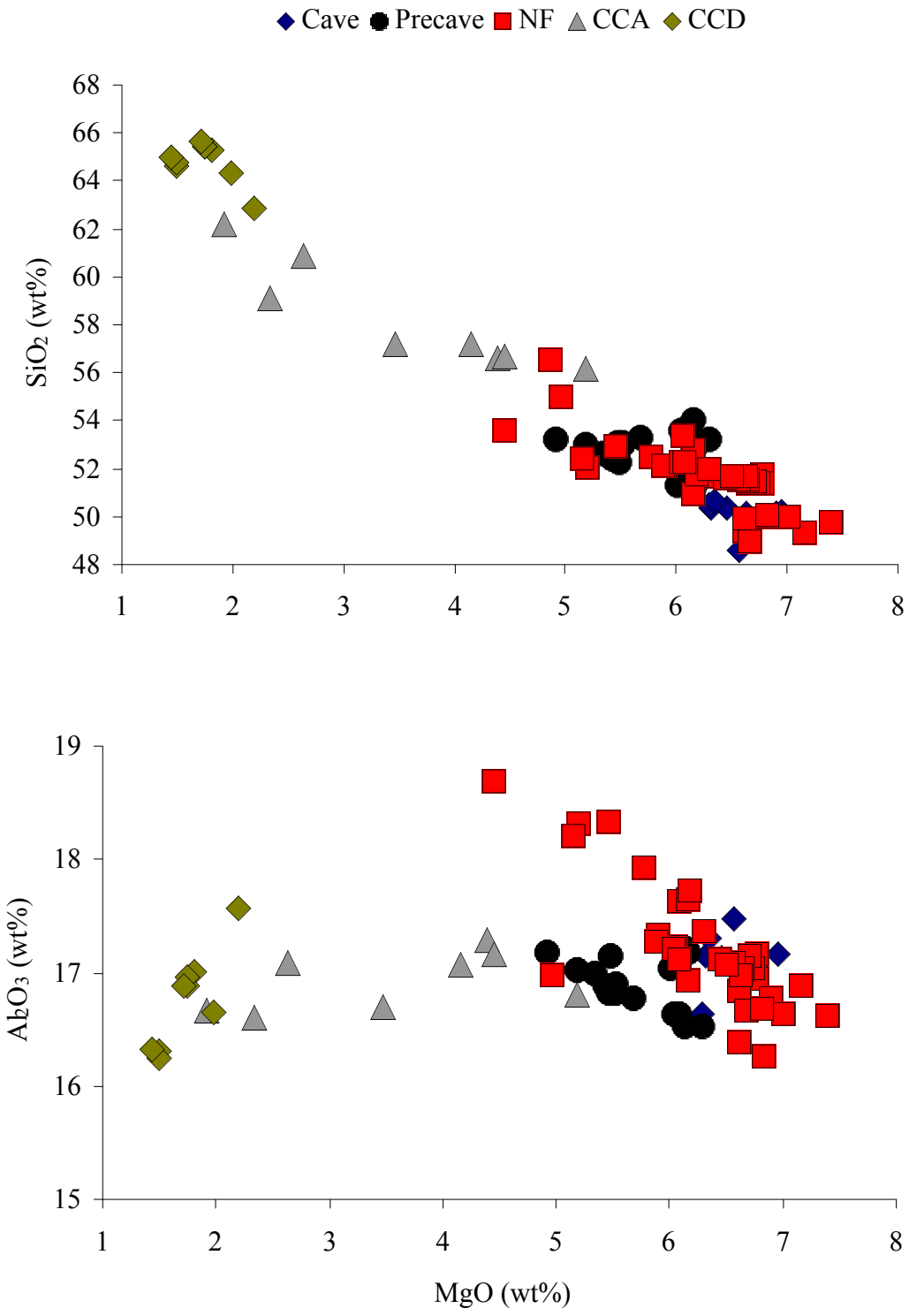

Figure 7. Whole-rock major element variation diagrams. Labels are as follows: NF = North flank basalt; CCA = andesites of Castle Creek; CCD = dacites of Castle Creek.

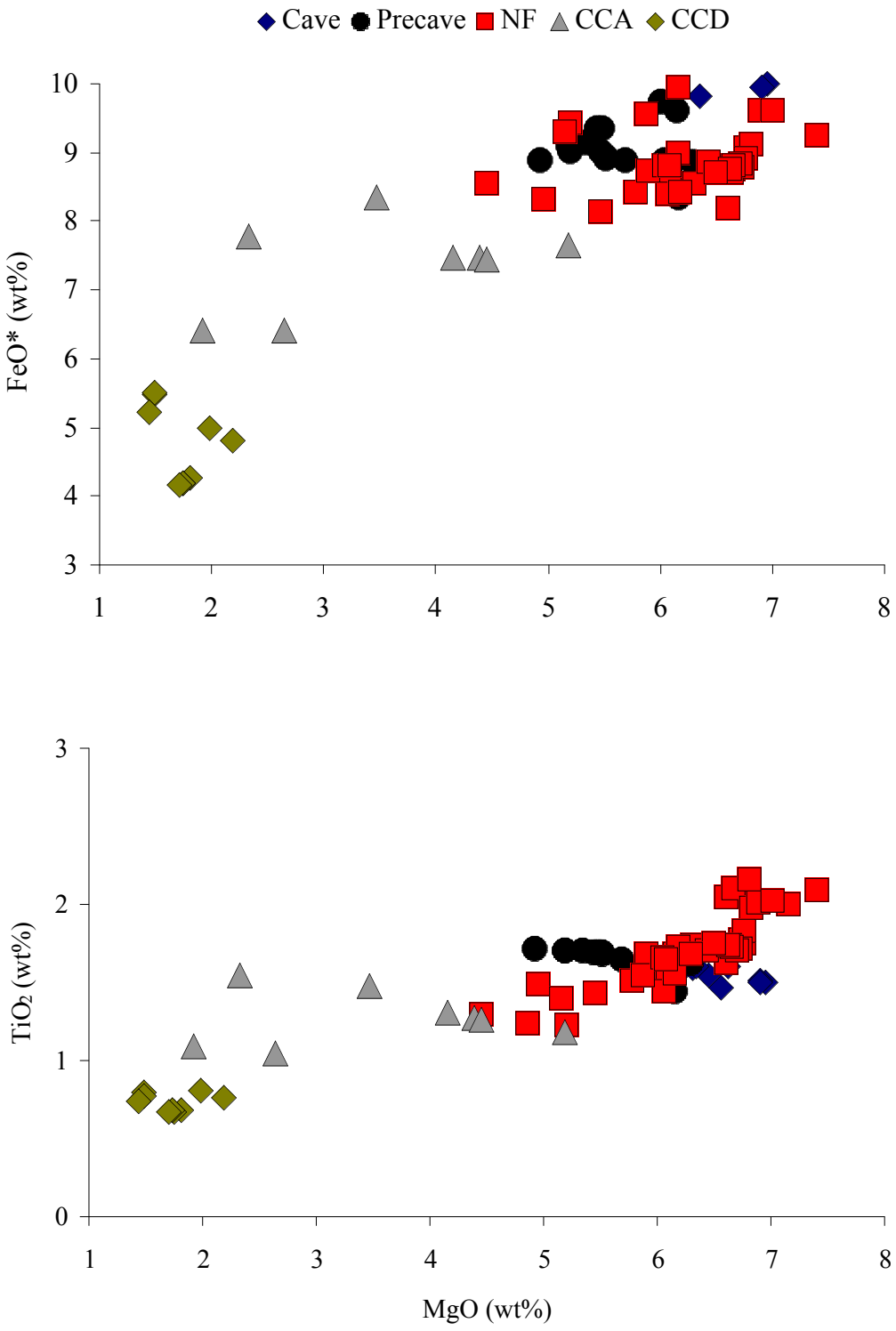

Figure 8. Whole-rock major element variation diagrams. Labels are as follows: NF = North flank basalt; CCA = andesites of Castle Creek; CCD = dacites of Castle Creek.

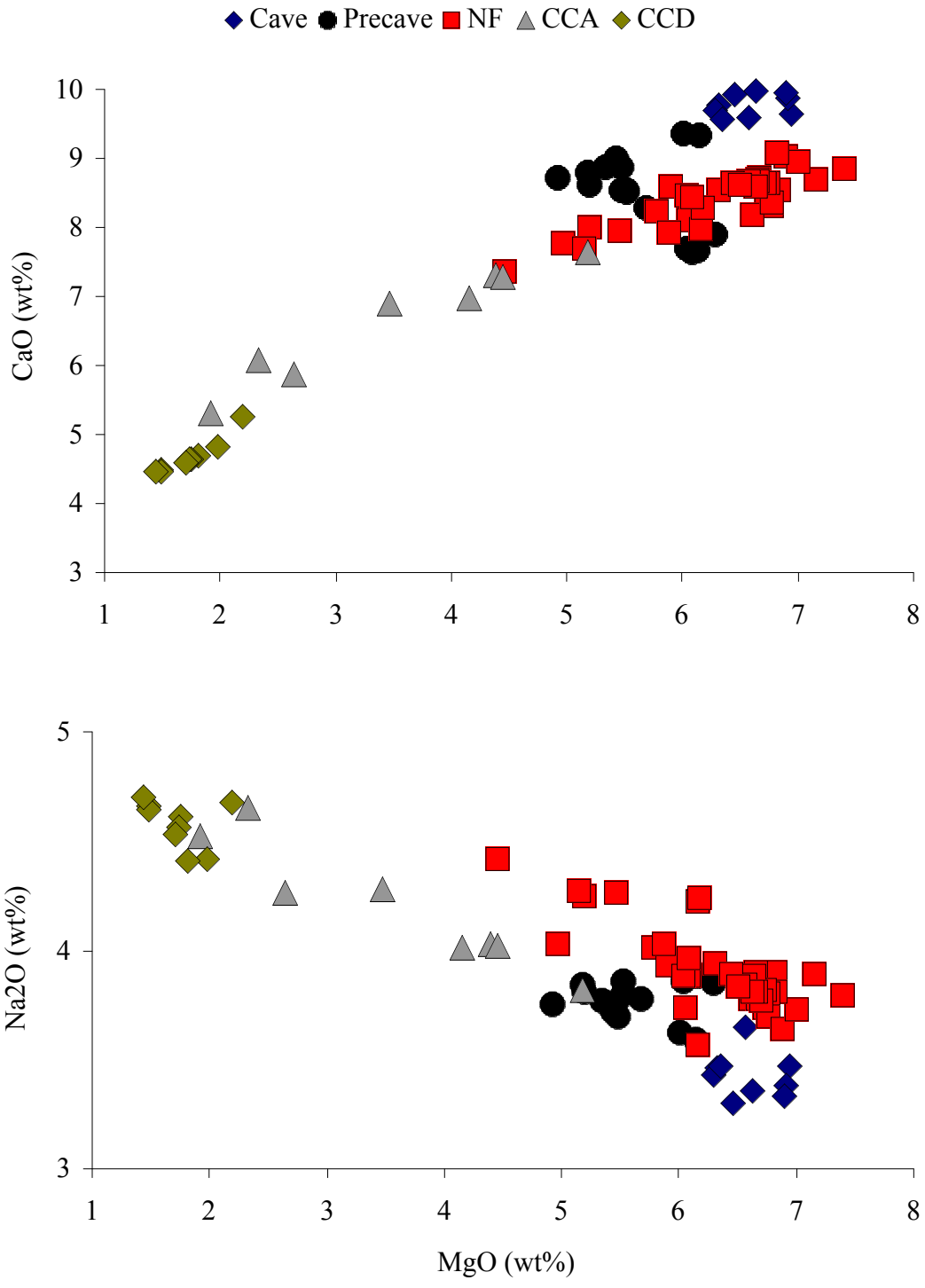

Figure 9. Whole-rock major element variation diagrams. Labels are as follows: NF = North flank basalt; CCA = andesites of Castle Creek; CCD = dacites of Castle Creek.

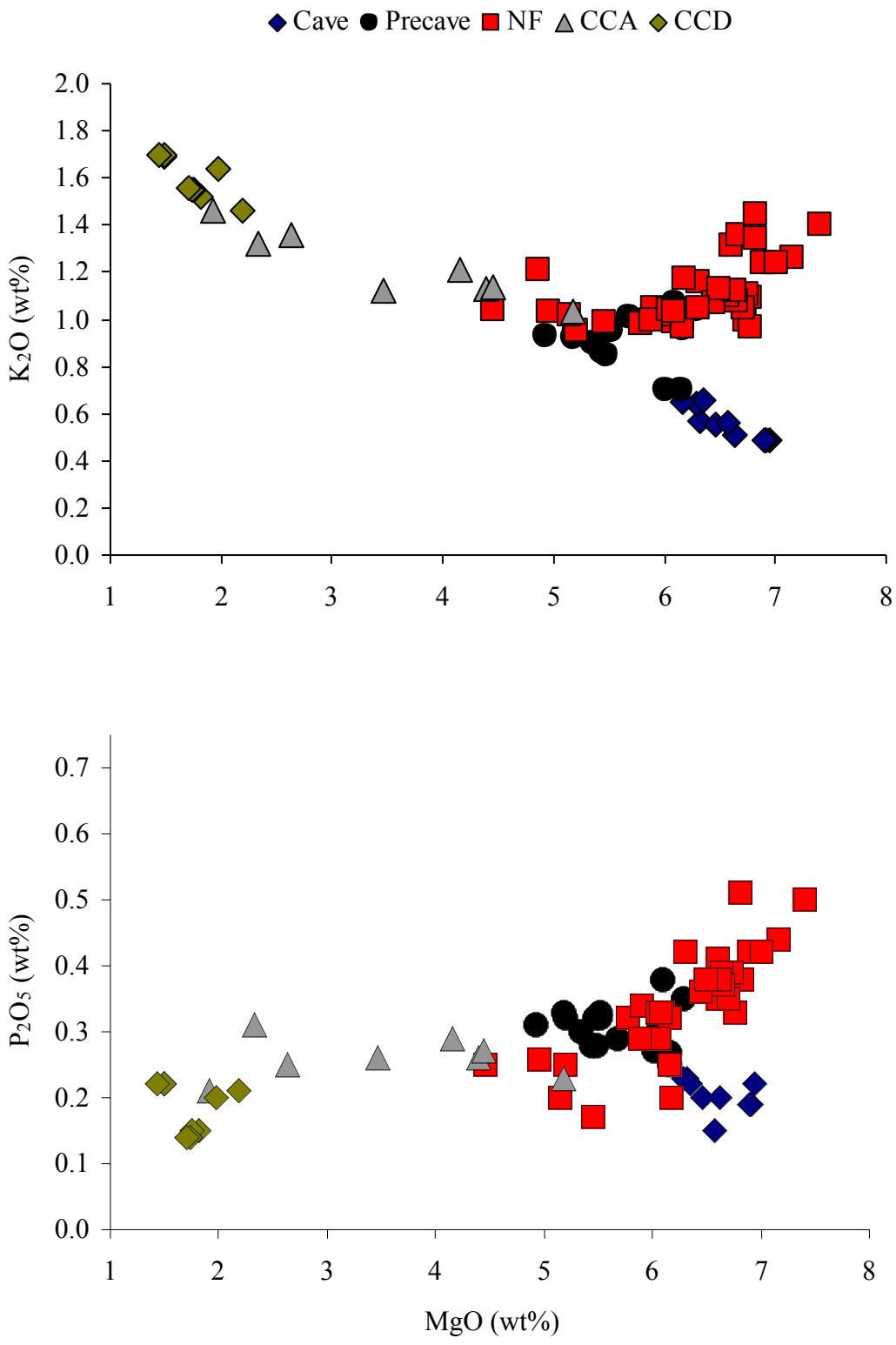

Figure 10. Whole-rock major element variation diagrams. Labels are as follows: NF = North flank basalt; CCA = andesites of Castle Creek; CCD = dacites of Castle Creek

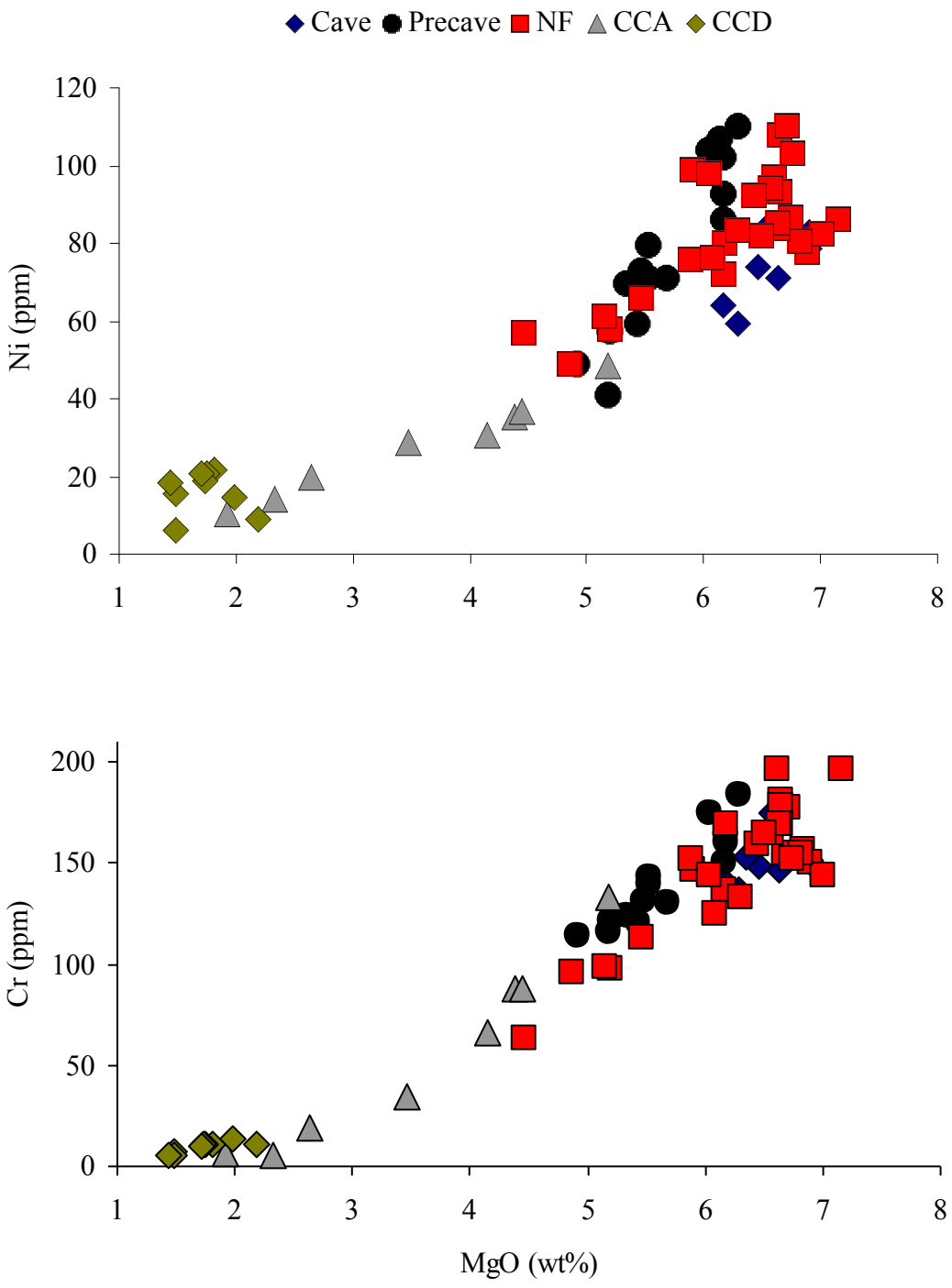

Figure 11. Whole-rock trace element variation diagrams. Labels are as follows: NF = North flank basalt; CCA = andesites of Castle Creek; CCD = dacites of Castle Creek. Note: Ni and Cr plots do not incorporate data collected by the present study, as those elements were not analyzed for.

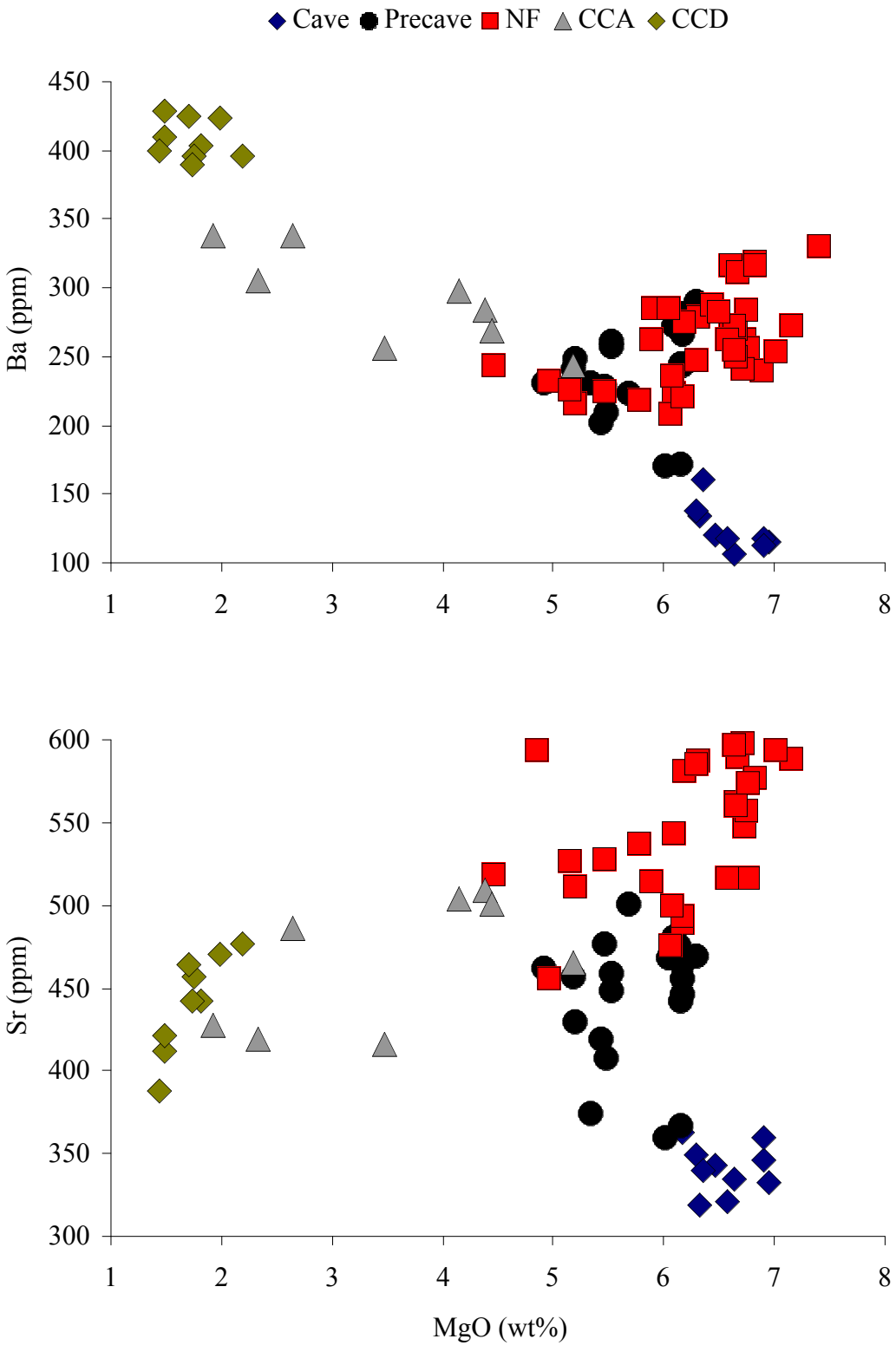

Figure 12. Whole-rock trace element variation diagrams. Labels are as follows: NF = North flank basalt; CCA = andesites of Castle Creek; CCD = dacites of Castle Creek.

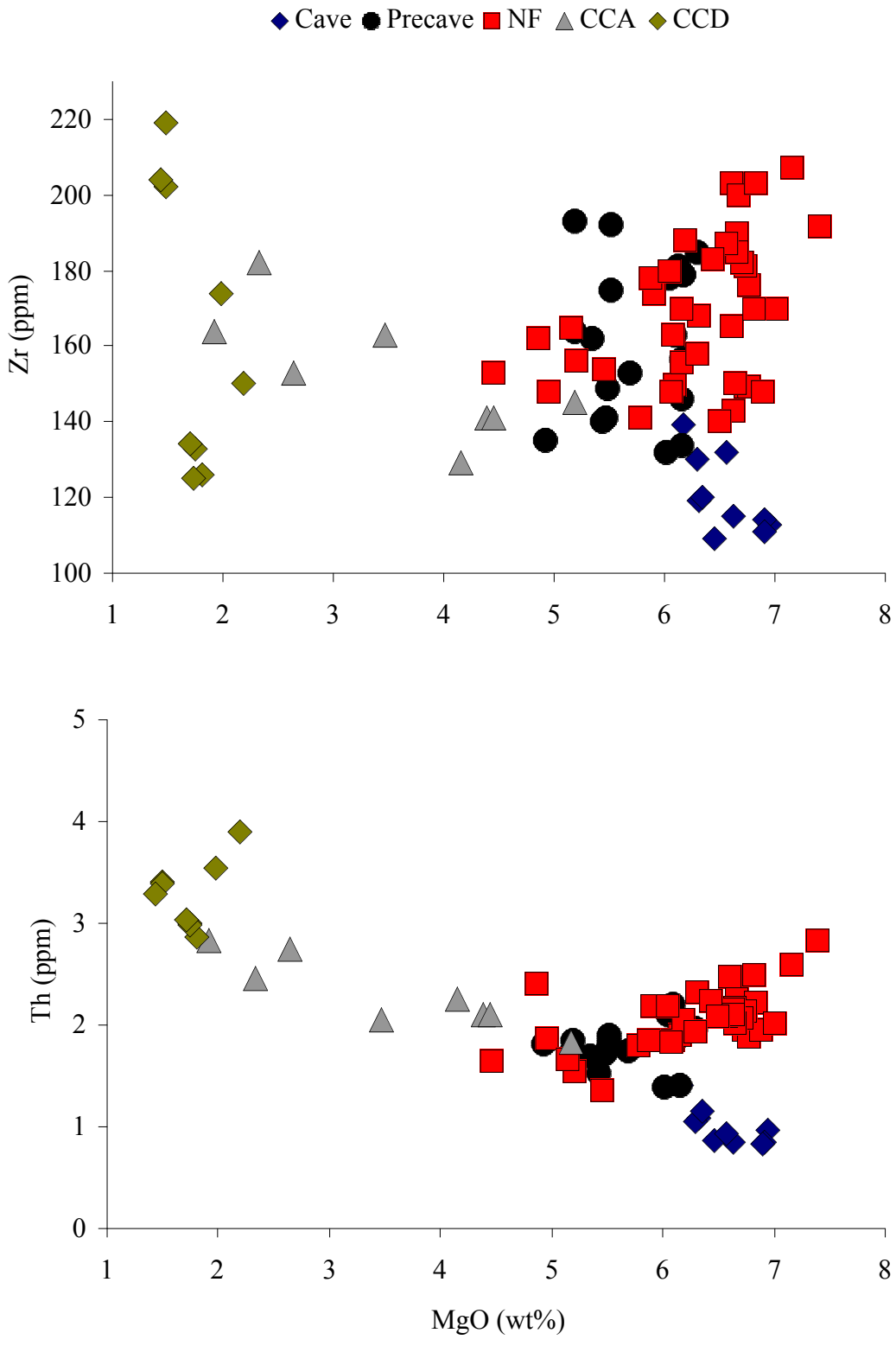

Figure 13. Whole-rock trace element variation diagrams. Labels are as follows: NF = North flank basalt; CCA = andesites of Castle Creek; CCD = dacites of Castle Creek.

almost all cases. Andesite data fall between 2 and 5 wt% MgO and exhibit negative trends for compatible elements and positive trends for incompatible elements. Dacites of Castle Creek affinity span a limited range of MgO (1.5-2.5 wt%) and form a small cluster of data points. Dacite trace element concentrations (e.g., Lu, Nd Ce, Y, Yb, Zr) typically display a range of concentrations. For example, Zr concentration varies between approximately 120 and 220 ppm over the 1 wt% range in MgO.

MELTS Modeling Results

The best fit closed-system fractional crystallization model of Cave and Precave evolution was run at isobaric conditions (2 kbar) with oxygen fugacity fixed 1 log unit above the quartz-fayalite-magnetite buffer. Initial liquid composition used in the model was the whole-rock composition of Cave sample SC99-302 (see Table 10) plus 1 wt% H_2O. The calculated liquidus temperature of this system was 1172.5 $^{\circ}$C. In the simulation, the system was cooled from above its liquidus temperature to approximately 850 $^{\circ}$C. The predicted equilibrium phase assemblage fractionated from this system (in order of decreasing temperature) was olivine, feldspar, clinopyroxene, orthopyroxene, spinel and apatite. Approximately 82% of the initial liquid was fractionated as solids during the course of the simulation. Plagioclase feldspar is the dominant equilibrium phase, making up approximately 44% of the fractionated mass. Calcic plagioclase (An_{77}) saturates and begins crystallizing at the 1156 $^{\circ}$C temperature step and reaches sodic compositions (An_{26}) by the 852 $^{\circ}$C temperature step. A list of equilibrium phase compositions and their liquidus temperatures and compositions is available in Table 11.

TABLE 10. PARENTAL COMPOSITIONS USED IN MELTS SIMULATIONS (WT% OXIDE)

	Cave/Precave		North Flank	
Sample	SC99-302	Normalized	W95-60B	Normalized
SiO_2	50.18	49.68	49.76	49.23
Al_2O_3	17.16	16.99	16.62	16.44
MgO	6.95	6.88	7.40	7.32
FeO*	9.99	10.13	9.25	9.57
CaO	9.64	9.54	8.85	8.75
Na_2O	3.47	3.44	3.79	3.75
TiO_2	1.50	1.49	2.09	2.07
K_2O	0.49	0.49	1.40	1.39
P_2O_5	0.22	0.22	0.50	0.49
H_2O	1.00	0.99	1.00	0.99
Total	99.60	99.84	99.66	100.00

Based on the observation that samples of North Flank lavas with comparable MgO to Cave lavas have very different concentrations of other major elements, a separate MELTS model was attempted for the NF data. The best-fit model used an initial liquid composition of North Flank whole-rock sample W95-60B plus 1 wt% H_2O. Evolution was once again modeled as a series of steps in temperature in an isobaric, closed-system fractional crystallization scenario. Pressure was fixed at 2.5 kbar and oxygen fugacity was fixed along the quartz-fayalite-magnetite buffer plus 3 log units. The calculated liquidus temperature of the system was 1189.8 ºC. The simulation was run from approximately 1190 °C to 800 ºC, at which point approximately 85% of the liquid had been fractionated as a solid. The equilibrium phase assemblage for this system consisted of (in order of decreasing temperature) olivine, plagioclase feldspar, clinopyroxene, orthopyroxene, spinel, apatite, biotite and sanidine. A complete list of the equilibrium phase assemblage, along with liquidus temperatures and phase compositions, can be found in Table 11. Plagioclase feldspar, clinopyroxene and spinel make up the bulk

TABLE 11. LIQUIDUS TEMPERATURES, PROPORTIONS AND COMPOSITIONS FOR MELTS MINERAL ASSEMBLAGE

	Cave/Precave model			North Flank model		
Phase	T (°C)	Mass (g)	Composition*	T (°C)	Mass (g)	Composition*
Clinopyroxene	1133	19.39	Di_{44}	1169	22.18	Di_{55}
Orthopyroxene	1109	7.63	CEn_{97}	1112	7.80	CEn_{99}
Spinel	1097	9.64	Mt_{65}	1160	10.68	Mt_{76}
Olivine	1170	4.42	Fo_{82}	1175	0.56	Fo_{90}
Feldspar	1156	43.87	$An_{26–77}$	1127	36.60	$An_{14–65}$
Apatite	972	2.06	-	1052	1.33	-
Ilmenite	-	-	-	851	0.19	-
Biotite	-	-	-	893	0.53	-
Sanidine	-	-	-	905	6.60	Or_{52}
System pressure (bar)	2000.0			2500.0		
System liquidus (ºC)	1172.5			1189.8		
Model final T (ºC)	852.5			800.0		
% fractionation	81.6			84.7		

*Compositional abbreviations: Di, diopside; CEn, clinoenstatite; Mt, magnetite; Fo, forsterite; An, anorthite

of solids fractionated from the North Flank parental basalt. Clinopyroxene makes up about 22% of fractionated solids in the simulation, coming on the liquidus at the 1169 °C temperature step. Plagioclase accounts for approximately 37% of solids, and begins fractionating at the 1127 °C temperature step with a composition of An_{65}. Figures 14 and 15 show an example of sensitivity testing with the MELTS algorithm. In this case, a best fit solution for the oxygen fugacity buffer is tested.

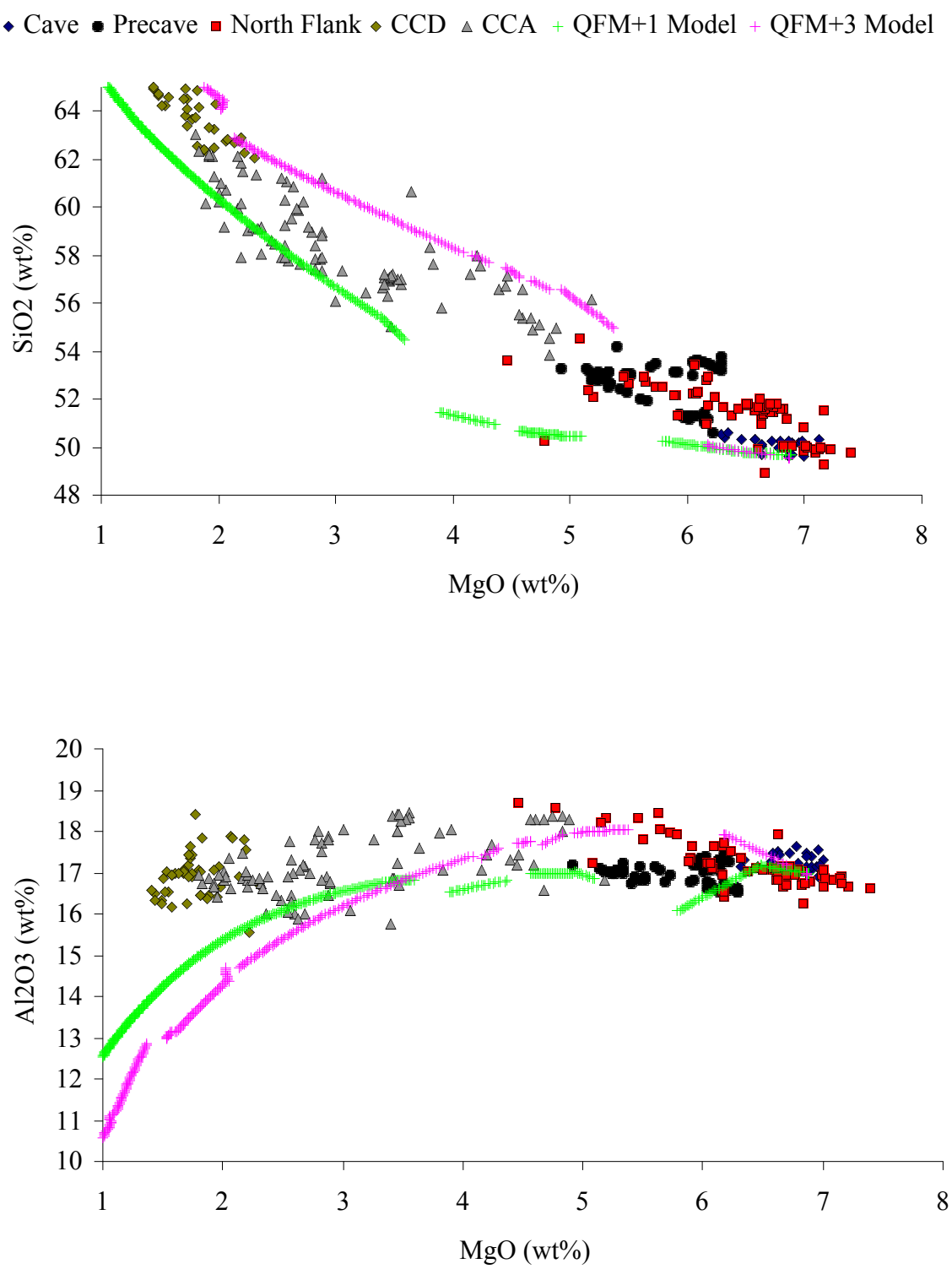

Figure 14. Results of MELTS sensitivity testing with oxygen fugacity buffers as the variable.

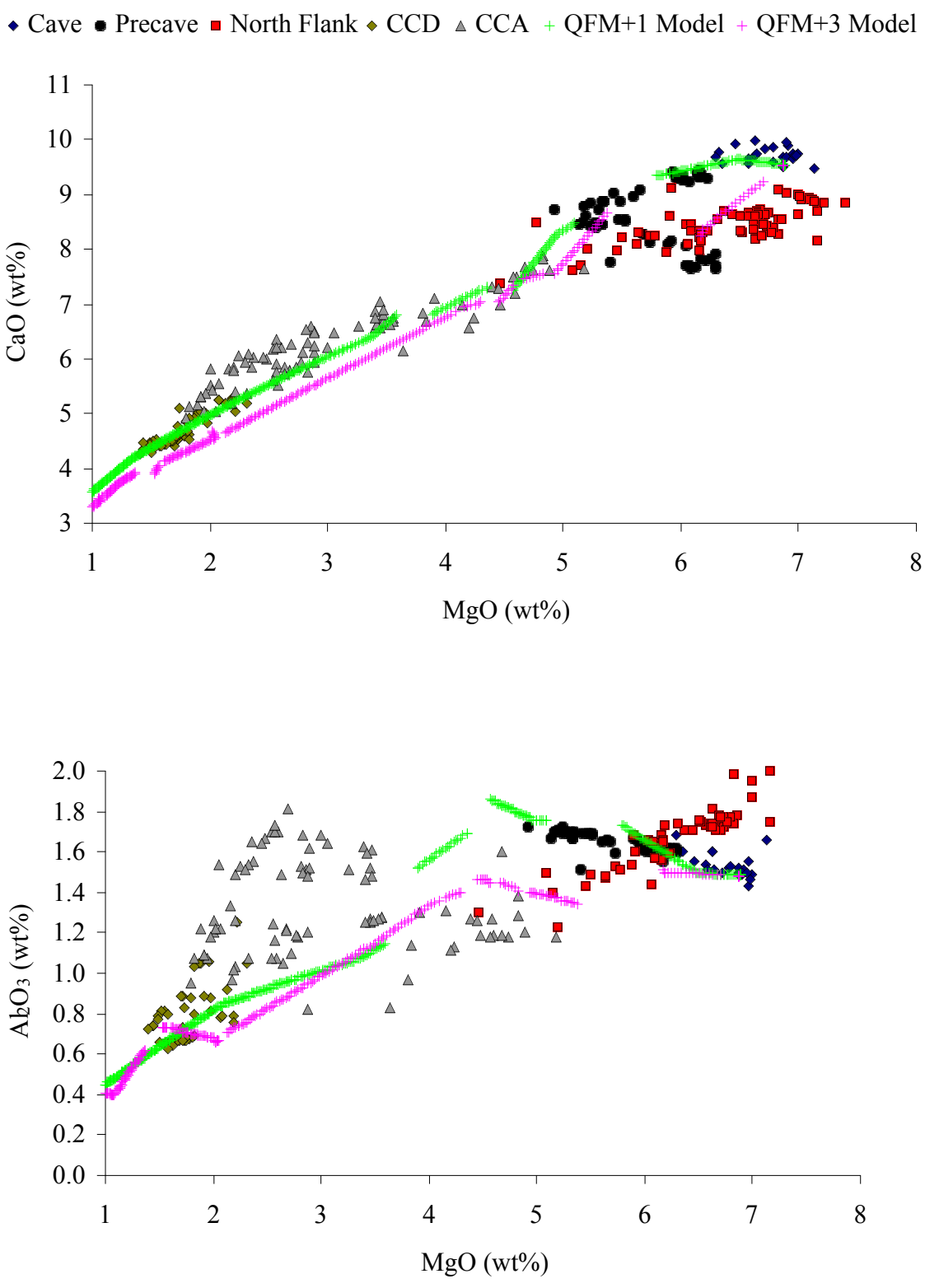

Figure 15. Results of MELTS sensitivity testing with oxygen fugacity buffers as the variable.

Strontium Isotopic Compositions

$^{87}Sr/^{86}Sr$ isotopic compositions of basalts from Castle Creek are available in Table 12. $^{87}Sr/^{86}Sr$ values for basalts range between 0.70303 and 0.70334. Figure 16 shows a plot of $^{87}Sr/^{86}Sr$ versus MgO and $^{87}Sr/^{86}Sr$ versus Sr concentration. The MgO versus $^{87}Sr/^{86}Sr$ diagram exhibits a trend for Cave and Precave analyses that is generally decreasing in MgO while increasing in $^{87}Sr/^{86}Sr$. The North Flank trend reveals similar behavior, with some data even overlapping with the Cave and Precave trend. Two North Flank data points (SC03-636, SC03-639) sit off of the main trend with high MgO values and the highest $^{87}Sr/^{86}Sr$ values. The same can be said for two data points within the Precave array (W01-212, SC04-683) that display the same behavior relative to the remainder of the Cave-Precave array.

TABLE 12. WHOLE-ROCK SR ISOTOPIC COMPOSITIONS BY TIMS

Sample	SiO_2 (wt%)	MgO (wt%)	K_2O (wt%)	Sr (ppm)	$^{87}Sr/^{86}Sr$	2σ error
SC99-302	50.18	6.95	0.49	332	0.703026	±0.00002
SC99-300	50.37	6.32	0.57	319	0.703114	±0.00001
W99-178	51.19	6.15	0.70	367	0.703206	±0.00001
SC99-301	51.28	6.01	0.70	359	0.703193	±0.000008
SC98-271	52.26	5.48	0.85	407	0.703286	±0.00001
W01-212	53.63	6.09	1.07	481	0.703350	±0.000015
SC04-683	54.05	6.16	1.03	442	0.703339	±0.00001
W95-60B	49.76	7.40	1.40	660	0.702974	±0.000009
SC03-636	51.62	6.73	1.00	547	0.703297	±0.00001
SC02-509	51.67	6.31	1.16	588	0.703086	±0.00001
SC03-639	51.76	6.77	0.97	516	0.703320	±0.00001
SC03-635	52.28	6.09	0.99	544	0.703105	±0.000008
SC02-527	52.48	5.78	0.98	537	0.703141	±0.000011
W00-197	52.81	6.16	1.00	489	0.703107	±0.00001
W02-230	53.39	6.06	1.02	476	0.703028	±0.00001
SC04-664	55.01	4.96	1.03	456	0.703234	±0.000011
SC04-701	49.40	6.61	1.08	614	0.703043	±0.000008

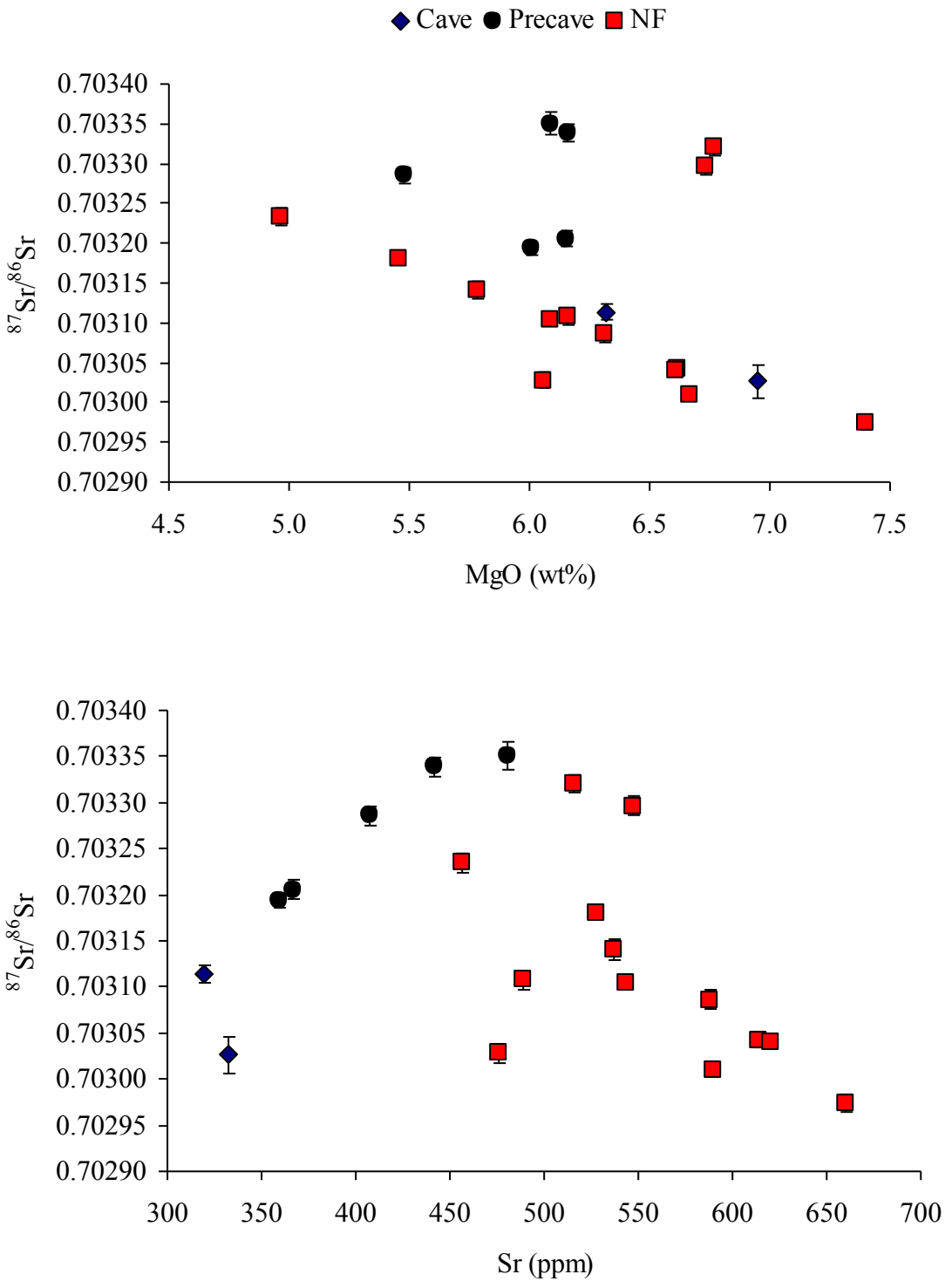

Figure 16. $^{87}Sr/^{86}Sr$ Isotopic compositions. NF = North Flank basalt.

CHAPTER IV

DISCUSSION

As previously argued, understanding the role of open-system processes in volcanic systems is a fundamental part of igneous petrology. Discussed in this chapter are the roles that magma chamber processes such as assimilation, fractional crystallization and magma mixing may have played in the MSH magma reservoir system during the Castle Creek eruptive period. The discussion of these processes and their impacts on basaltic volcanism at MSH is based on varying interpretations of data presented in the results section of this thesis. The following discussion takes special care to not limit alternative hypotheses when possible. Due to the laterally discontinuous nature of these lava flows, knowledge of stratigraphic position of individual flows is limited. Furthermore, a large portion of the geochemical data used for this study comes from unpublished works, further complicating the task of placing samples in stratigraphic order. For the sake of discussion, chemical and other trends examined in this chapter are considered from as many perspectives as is possible. This approach leaves more options open for discussion. Supporting evidence then, such as isotopic ratios, mineral chemistry or petrography, is bestowed the task of refuting or supporting each hypothesis in turn.

Fractional Crystallization

As indicated by whole rock major and trace element data, fractional crystallization most likely played a role in the evolution of Castle Creek age magma. Trends that display decreasing MgO with simultaneously increasing incompatible

elements likely reflect fractional crystallization processes. Interpretation of whole rock major element data, coupled with observations of the minerals present in the lavas, generates qualitative hypotheses regarding fractional crystallization processes. MELTS simulations add quantitative constraints to these hypotheses. MELTS models produced by this study approximate Cave and Precave observed major element trends with isobaric fractional crystallization. A separate MELTS simulation was executed for North Flank data because the data trends are not qualitatively consistent with a model of fractional crystallization involving typical basaltic phases. No single MELTS model was able to replicate observed values for all three basalt units simultaneously due to vast differences in initial composition. Two separate starting compositions were used (sample SC99-302 for Cave basalt, sample W95-60B for North Flank). Initial conditions were similar for each simulation, and simulation procedures were exactly the same.

MELTS Simulation of Cave-Precave Evolution

The MELTS simulation of Cave/Precave liquid evolution ran at 2 kbar and along a best-fit path at the QFM+1 oxygen buffer, with an initial water content of 1 wt%. The results of this simulation were compiled and superimposed over observed data. Figures 17, 18 and 19 display the characteristics of the Cave-Precave best-fit model in comparison with observed chemistry for selected oxides. These results suggest that fractional crystallization of a primitive basalt composition (Cave sample SC99-302) could be responsible for much of the observed variation in major element chemistry

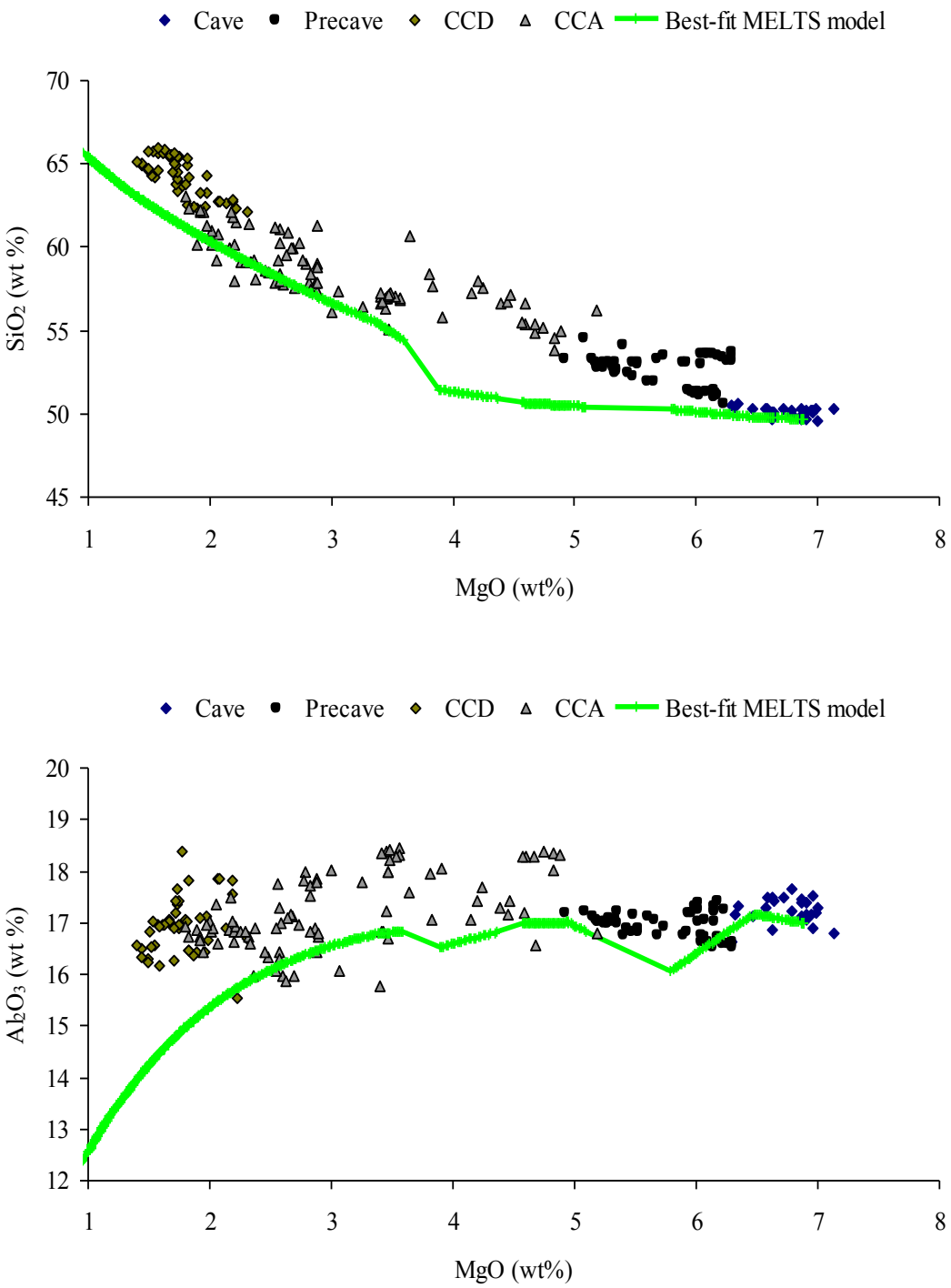

Figure 17. Best-fit MELTS solution for Cave basalt evolution. North Flank basalt data are excluded for clarity. CCD = Castle Creek dacites, CCA = Castle Creek andesite.

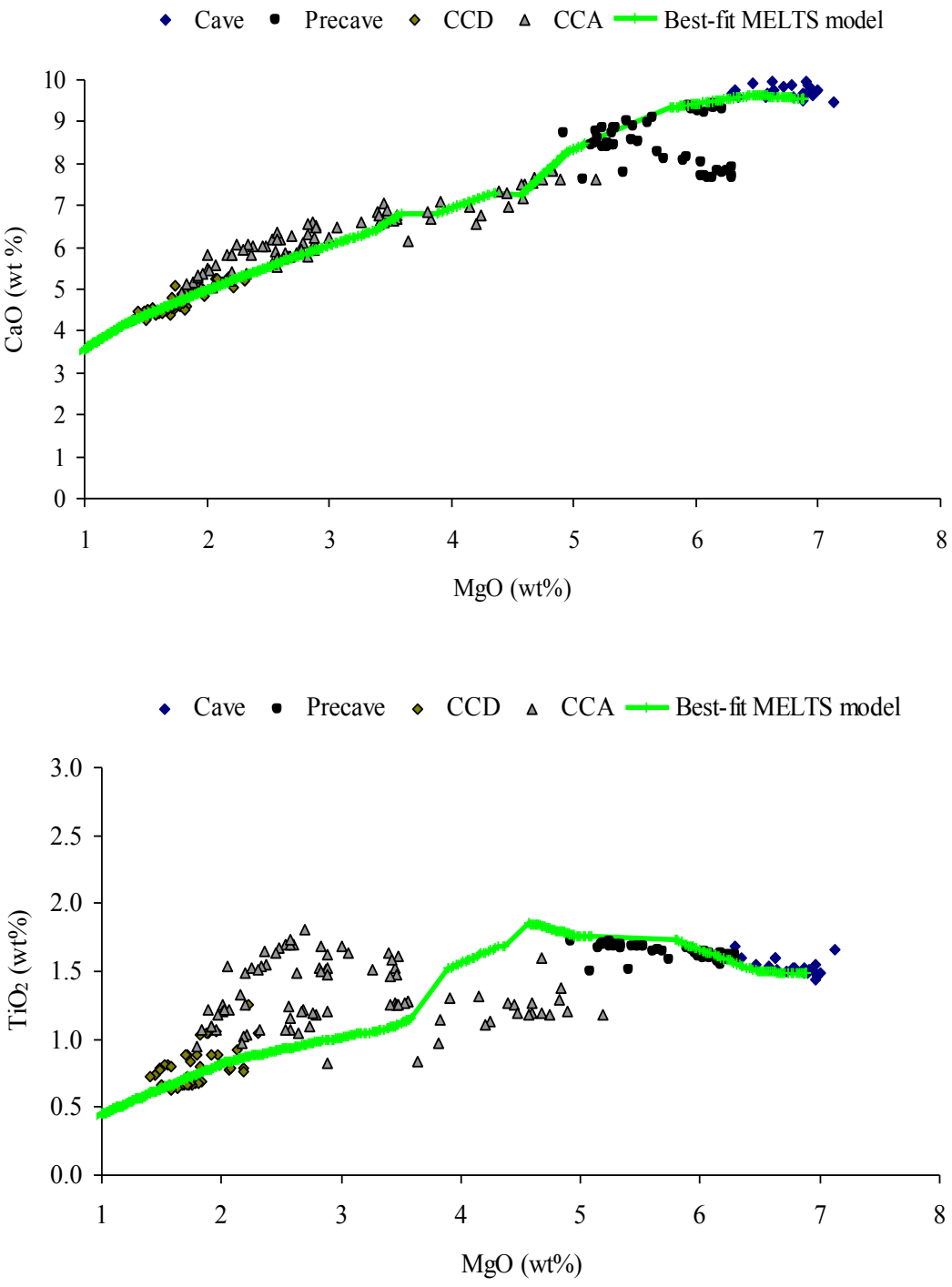

Figure 18. Best-fit MELTS solution for Cave basalt evolution. North Flank basalt data are excluded for clarity. CCD = Castle Creek dacites, CCA = Castle Creek andesite.

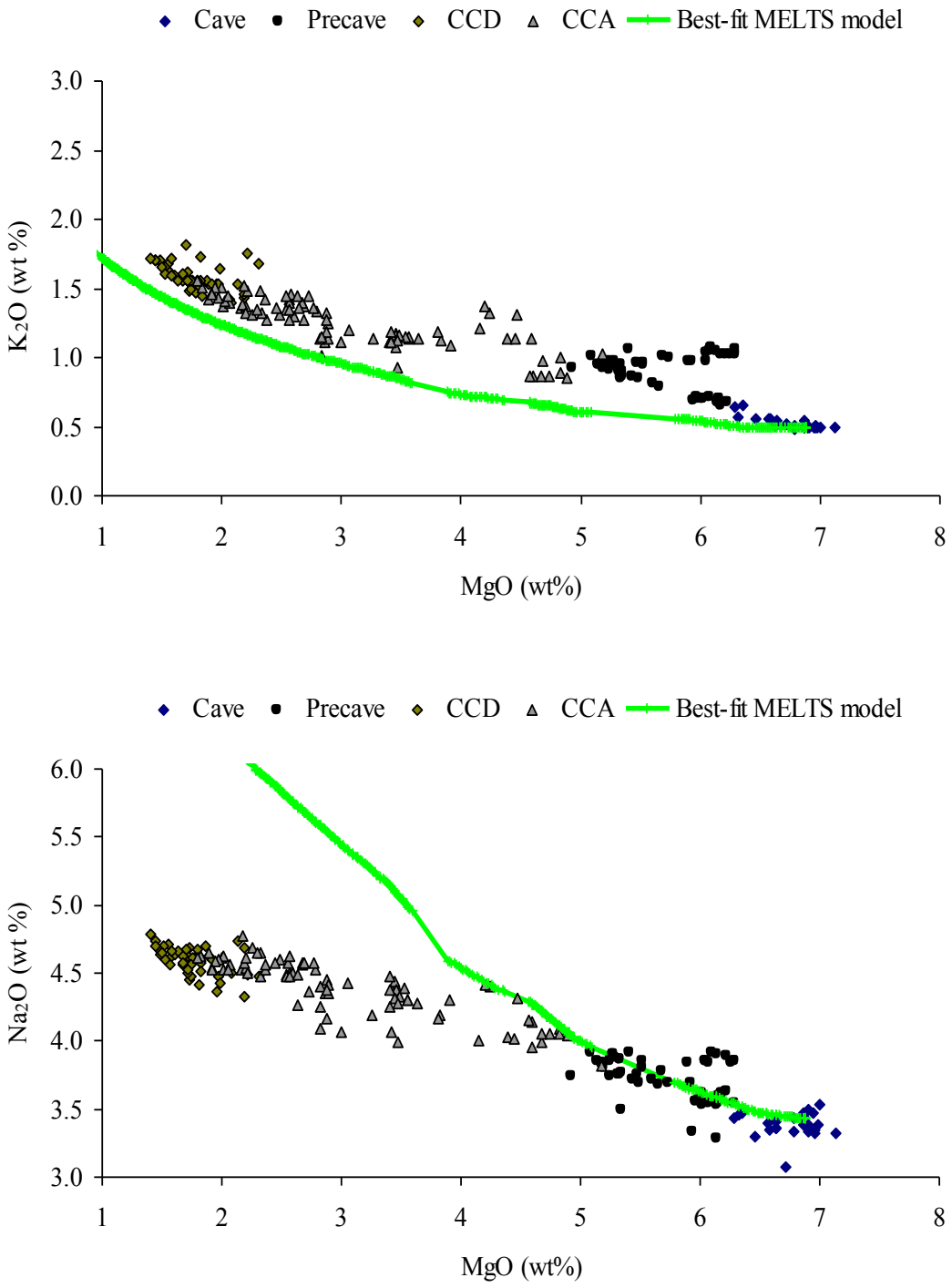

Figure 19. Best-fit MELTS solution for Cave basalt evolution. North Flank basalt data are excluded for clarity. CCD = Castle Creek dacites, CCA = Castle Creek andesite.

within the Castle Creek eruptive period. In fact, these plots reveal, in a first order sense, that Castle Creek period andesite and dacite compositions are attainable by fractional crystallization as well. This is not to say that fractional crystallization of a primitive Cave basalt such as sample SC99-302 is responsible for all observed variation, as data exist which are not satisfied by the model. Disagreement of model and observed values is found in all oxides but most noticeably SiO_2, Al_2O_3 and Na_2O. In the MELTS simulation, observed values of SiO_2 increase more rapidly than predicted by the simulation. The shape of the observed trend is also quasi-linear with a faint inflection point near the most SiO_2-rich andesite data, whereas MELTS simulations create a sharp-angled curve which changes slope about a well-defined inflection point at approximately 4 wt % MgO. Increasing oxygen fugacity in log unit steps helps to alleviate this problem in SiO_2 space, but typically decreases the goodness of model fit with respect to other oxides (e.g., TiO_2). The controlling mechanism in this case is saturation and crystallization of Fe-Ti oxides. Oxygen fugacity plays a major role in determining onset of Fe-Ti oxide crystallization and the composition of the mineral phase produced. The inflection point of each MELTS model curve in SiO_2-MgO space reflects onset of Fe-Ti oxide crystallization.

Observed values for the oxide Al_2O_3 are not in agreement with the results of the MELTS simulation. The simulation predicts an initial decrease in Al_2O_3, followed by an increase back to near-initial concentration. From this point, Al_2O_3 decreases along a concave-up curve that lies below observed concentrations. The high levels of Al_2O_3 relative to predicted concentrations could be related to a bias caused by plagioclase

accumulation within sampled lava flows. Furthermore, the comparison involves concentrations of Al_2O_3 predicted by MELTS for the residual liquid to bulk rock analyses, which are crystals plus liquid. Modeled Na_2O also fails to reproduce observed values. Cave, Precave and earliest andesite observed compositions are closely replicated by the model results, but separation occurs between the two at approximately 4.5 wt% MgO. At this point, the model curve becomes too steep and the trends diverge.

MELTS Simulation of North Flank Evolution

The best-fit model of North Flank evolution used an initial liquid composition equivalent to the bulk-rock composition of sample W95-60B. The simulation was executed at 2.5 kbar and was fixed at the QFM+3 oxygen fugacity buffer. Initial water content was set at 1 wt%. Plots of observed whole-rock chemistry with MELTS data for North Flank rocks are shown in Figures 20, 21 and 22. Data from North Flank samples show trends that are not easily explained by fractional crystallization of typical phases in equilibrium with basaltic magmas. MELTS simulations could not recreate observed K_2O, TiO_2 and Na_2O abundances. Observed values of TiO_2 decrease with decreasing MgO in a linear array. TiO_2 in MELTS simulations is initially incompatible and thus remains at constant concentration until approximately 6.5 wt% MgO. The onset of Fe-Ti oxide crystallization removes TiO_2 from the system, creating an inflection in the MgO-TiO2 trend. Numerous iterations that involved changing parameters modified the relative location of the inflection, but could not completely suppress the behavior; therefore model curves remain above observed North Flank TiO_2 values. Observed data may not

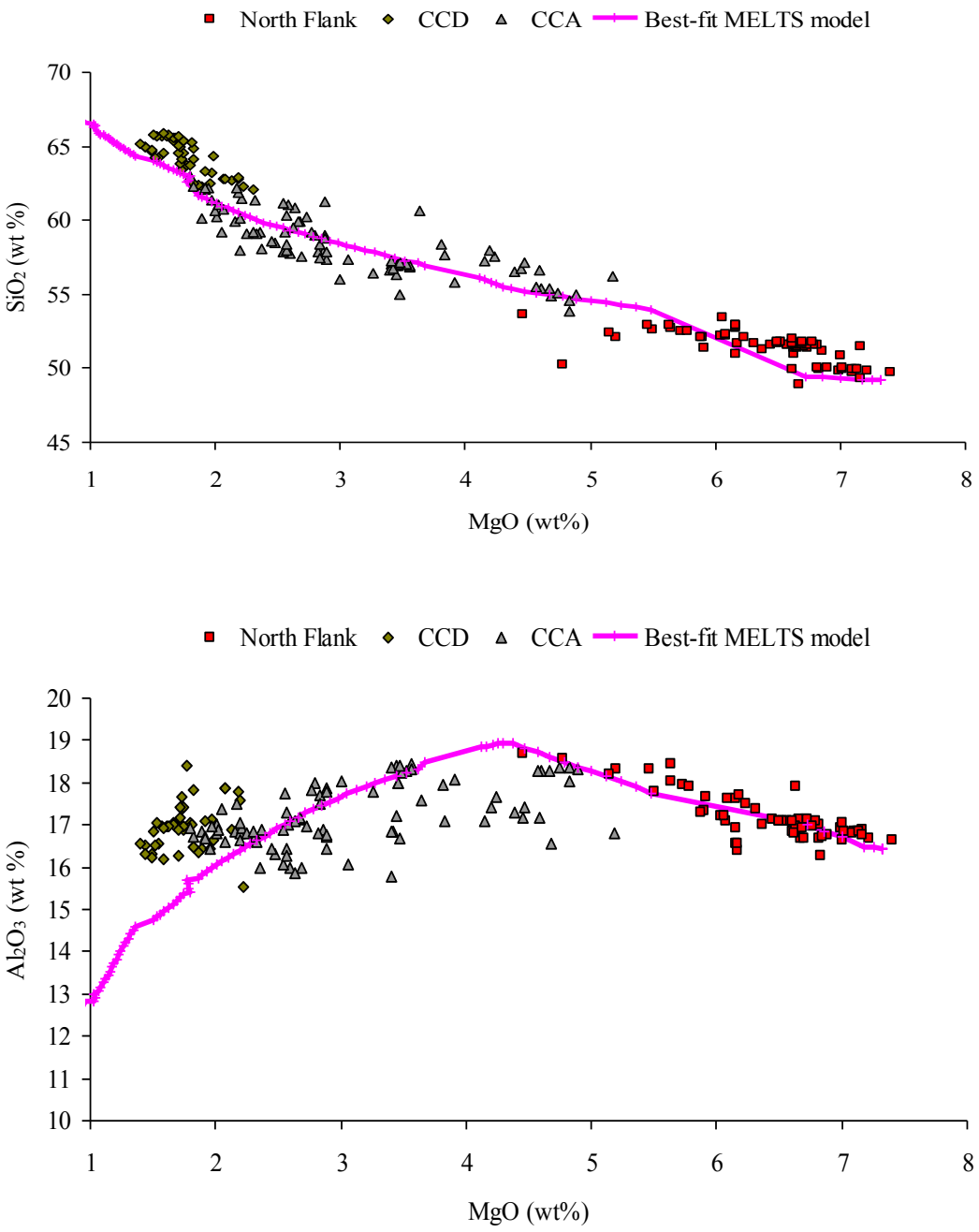

Figure 20. Best-fit MELTS solution for North Flank basalt evolution. Cave and Precave basalt data are excluded for clarity. CCD = Castle Creek dacites, CCA = Castle Creek andesite.

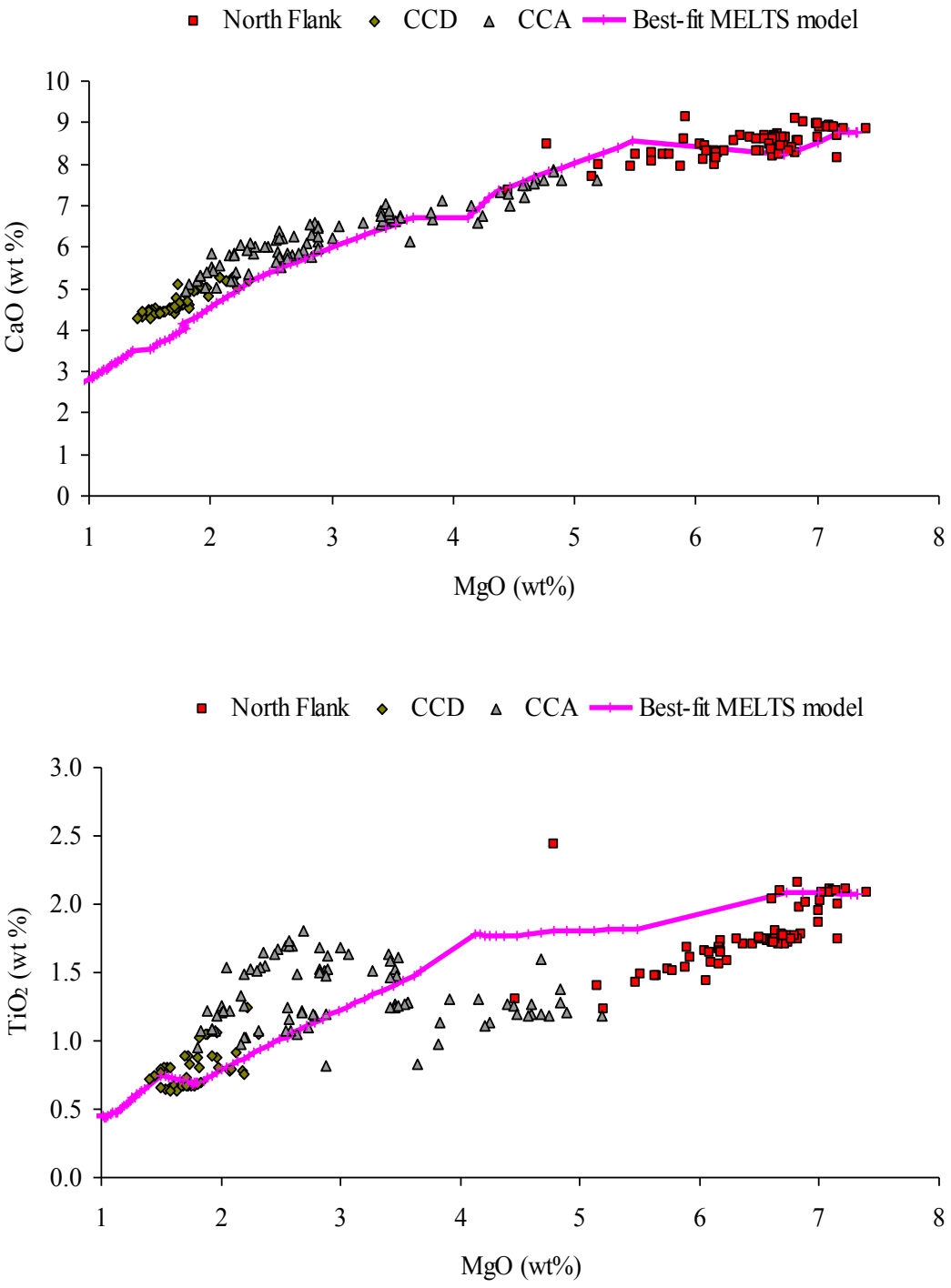

Figure 21. Best-fit MELTS solution for North Flank basalt evolution. Cave and Precave basalt data are excluded for clarity. CCD = Castle Creek dacites, CCA = Castle Creek andesite.

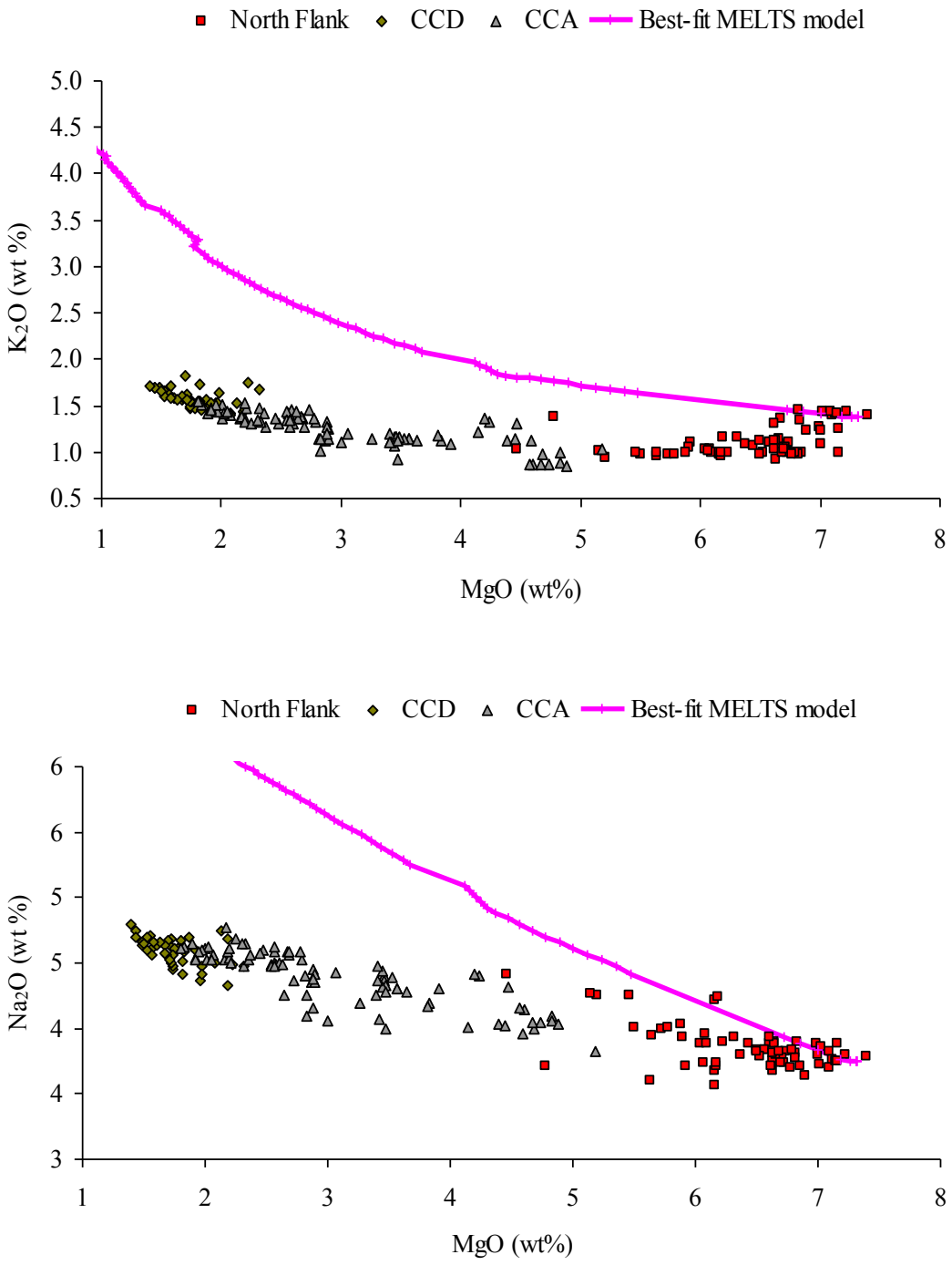

Figure 22. Best-fit MELTS solution for North Flank basalt evolution. Cave and Precave basalt data are excluded for clarity. CCD = Castle Creek dacites, CCA = Castle Creek andesite.

display inflection representative of the onset of crystallization of Fe-Ti oxides for a number of reasons. The first and perhaps most simple is that Fe-Ti oxides had saturated and begun crystallizing before the volcano began to sample the North Flank magma batch. A second, more complicated explanation involves magma mixing of the North Flank magma with a component with lower TiO_2. This possibility will be further explored below.

Observed K_2O values in North Flank data display behavior similar to that described for TiO_2. Initial (high MgO) abundances of K_2O are high and decrease with decreasing MgO concentration. This is opposite of typical fractional crystallization, as K_2O remains incompatible until the onset of crystallization of such phases as biotite and amphibole. Biotite and amphibole are not present in North Flank samples, nor does the best-fit MELTS model predict them as stable fractionating phases.

Predicted values of Na_2O concentrations increase more rapidly than observed values and continue that trend for the entirety of the model (see Figure 22). The relationship between observed and simulated data is very similar to that seen in the Cave model. This may be the effect of the model predicting incorrect plagioclase compositions; thus the amount of Na_2O removed by fractionation from the system is not correct.

The role of fractional crystallization as discussed by Smith and Leeman (1987) is reduced to one of secondary importance with respect to the evolution of the MSH plumbing system during Castle Creek time. The authors test the hypothesis that fractional crystallization could generate dacite rocks from Castle Creek basalt

compositions. They found dacite products from MSH to have similar, and in some cases lower abundances of trace elements (such as Zr, Hf, REE, U, Be, Ta, and Nb) when compared to associated basalts, thus precluding a relationship by simple fractional crystallization. Instead, Smith and Leeman (1987) propose melting of metabasaltic rocks at crustal levels to generate dacite liquid depleted in REE and high field strength elements (HFSE). The energy for melting in this case is related to intrusion of mantle-derived mafic magma.

A subsequent paper by Smith and Leeman (1993) focuses on fractional crystallization as a means evolving Castle Creek basaltic liquid into associated andesites. Fractional crystallization is determined to be a secondary process in this instance as well. Mixing, which will be discussed more below, is the primary mechanism invoked by the authors, as multiple lines of evidence (isotopic, trace element) support andesite generation by mixing of Castle Creek age basalt with dacite.

Magma Mixing

Results of MELTS modeling reveal that fractional crystallization of a liquid of either Cave (SC99-302) or North Flank (W95-60B) affinity can reproduce major element oxide trends on a first order level. Although there is some scatter, trace element trends (e.g., Ba and Sr) in the Cave and Precave suites typically increase with decreasing MgO. Such behavior is broadly consistent with fractional crystallization, although detailed modeling of all elements is required to confirm this. However, as discussed above for North Flank samples, the behavior of some oxides is not consistent with simple fractional

crystallization. Among the most obvious is K2O. Referring back to Figures 11, 12 and 13, it is clear that most trace element plots mimic to varying degrees the behavior of the K_2O-MgO plot. That is, trace element concentration decreases with decreasing MgO concentration. Magma mixing could potentially generate such trends. Thus, an hypothesis worthy of further research is that the geochemical signatures of the North Flank basalts represent magma mixing. However, other oxide-oxide trends such as CaO-MgO and Al2O3-MgO are not consistent with simple magma mixing, suggesting additional complications must be considered. Furthermore, trace element data (e.g., Cr, Ni) do exist that seem to be more closely related with AFC processes, such as Cr and Ni. Indeed, if magma mixing is occurring in North Flank magma, it is doing so without substantially altering the magma with respect to other elements and oxides.

Strontium Isotopic Compositions

$^{87}Sr/^{86}Sr$ data from Castle Creek basalts produced by this study reveal increasing isotopic ratios with decreasing abundance of MgO. These results can be interpreted to be consequences of assimilation, magma mixing, or a combination of one or both with fractional crystallization. The process of assimilation has been energetically linked to fractional crystallization (Spera and Bohrson, 2001 and references therein). Thus, fractionation of a Mg-rich phase (e.g., olivine) could generate the decreasing MgO trend while simultaneously driving anatexis and assimilation, leading to an increase in the $^{87}Sr/^{86}Sr$ ratio of the magma. On the other hand, magma mixing could generate the observed variations if the recharge magma has a sufficiently high $^{87}Sr/^{86}Sr$ ratio. Again,

the simultaneous decrease in MgO could be attributed to either the process of mixing itself, or to fractional crystallization processes, or a combination of both. The Cave-Precave and North Flank trends, with the exception of 4 data points, are subparallel in $^{87}Sr/^{86}Sr$ versus MgO space (Figure 16), perhaps representing coincident but separate assimilation fractional crystallization (AFC) trends as discussed above. However, in a plot of $^{87}Sr/^{86}Sr$ versus Sr concentration (Figure 6) North Flank samples decrease in Sr concentration as $^{87}Sr/^{86}Sr$ increase. In contrast, the Cave-Precave samples increase in Sr concentration as $^{87}Sr/^{86}Sr$ increases. The Cave-Precave trend can still be reconciled with AFC processes, although the trend requires that as assimilation is occurring, more Sr is added through incorporation of anatectic melt than is being removed by FC. A possible explanation for the North Flank trend involves magma mixing with a basaltic component possibly similar to Precave.

Feldspar Compositions

Results of electron microprobe analyses, as discussed in the previous chapter, reveal crystals with a relatively broad range of An contents (An_{45-89}). Anorthite contents of plagioclase crystal cores and rims from each sample of Cave, Precave and North Flank basalt are plotted against the whole-rock abundance of MgO (Figure 23). Superimposed over the data is the predicted equilibrium anorthite-MgO trend as calculated by the associated best-fit MELTS model. Both the Cave-Precave and North Flank best-fit simulations are represented on the figure. Core analyses for all samples except SC98-271 share approximately the same core maximum An content, near An_{82}. Sample SC98-

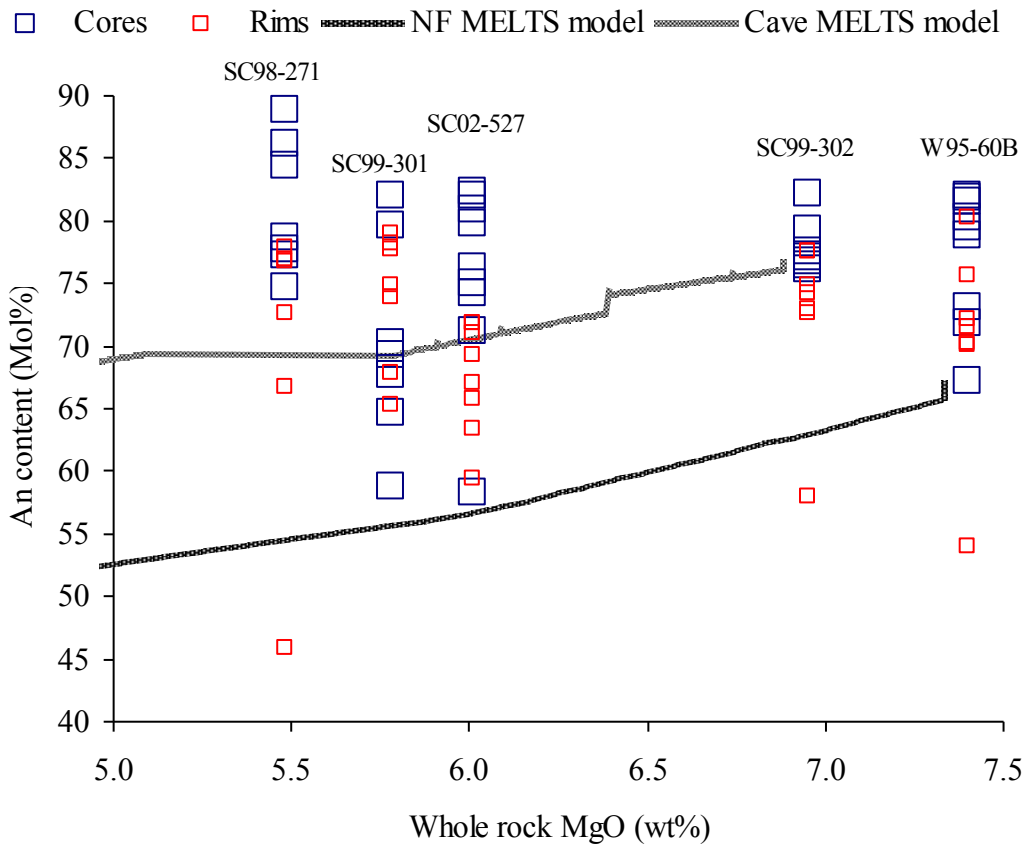

Figure 23. Plagioclase core and rim compositions compared to MELTS predicted equilibrium plagioclase compositions. SC99-302 is Cave basalt; SC99-301 and SC98-271 are Precave basalts; W95-60B and SC02-527 are North Flank (NF) basalt.

271 has a slightly higher maximum An content of approximately An_{89}. Rims are typically lower in An than cores. For rims and cores of all samples, a wide range of An contents are evident. This observation, coupled with the observation that the majority of compositions lie above the predicted equilibrium compositions given by MELTS, suggests that simple fractional crystallization is not the only explanation for the origin of either Cave-Precave or North Flank basalts.

Figures 24, 25 and 26 plot crystal size versus An content for both core and rim analyses on a sample by sample basis. For most crystals, this figure reveals that plagioclase is normally zoned. However, reversely zoned crystals do exist in all of the samples and are most prevalent in North Flank sample SC02-527. Based on this figure, no apparent relationship exists between size and An content of crystal core or rim. The one apparent feature is Cave sample SC99-302, which, with the exception of one data point, has the least variation of crystal core An contents over the size range. Comparison of analyses with NDIC and BSE imagery reveals many analyses of high-An cores are from crystals with sieve textures. Since sieve-textured zones cannot be analyzed directly by EMP, the spot for the analysis is typically the closest adjacent area of clean crystal growth, often resulting in an analysis taken at some distance from the spatial center of the Crystal. Thus, sieve-textured plagioclase analyzed in this study may not be representative of crystal cores, but may be more closely related to an intermediate stage of growth. Furthermore, Precave sample SC99-301 contains several core analyses that lie on or below the predicted equilibrium trend. This observation suggests the method employed by this study may not have revealed crystals with equilibrium cores simply because of the low numbers of crystals analyzed. Moreover, Figures 24-26 reveal very few crystals smaller than 500 μm were analyzed. A sampling bias towards complex, large plagioclase phenocrysts, coupled with the complications of analyzing texturally complex

regions might have contributed to a biased data set. More analyses over a larger crystal size range are needed to better assess relationships between size, anorthite content

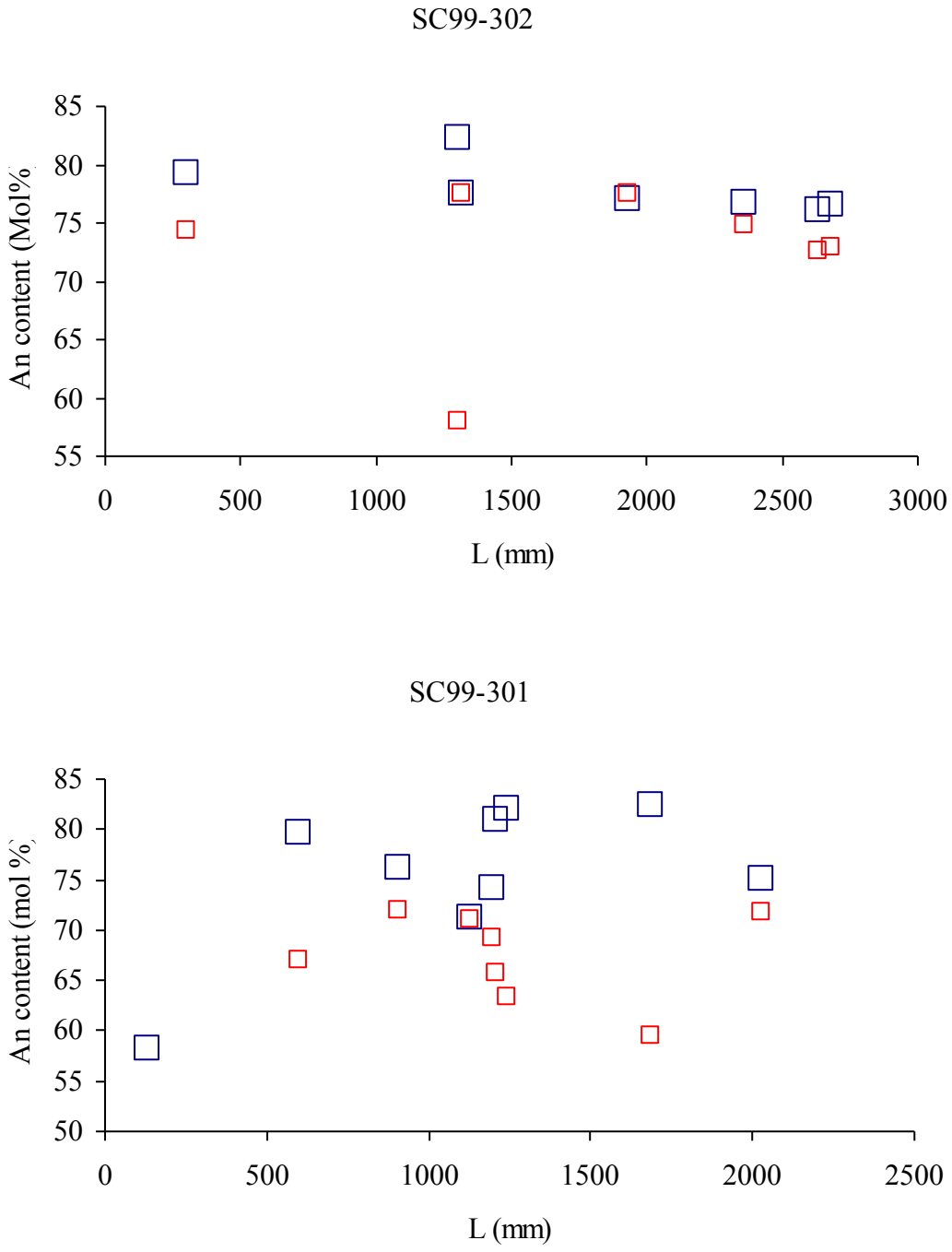

Figure 24. Plagioclase core and rim analyses versus crystal size for samples SC99-302 and SC99-301. Blue squares represent core compositions; red squares are rim compositions.

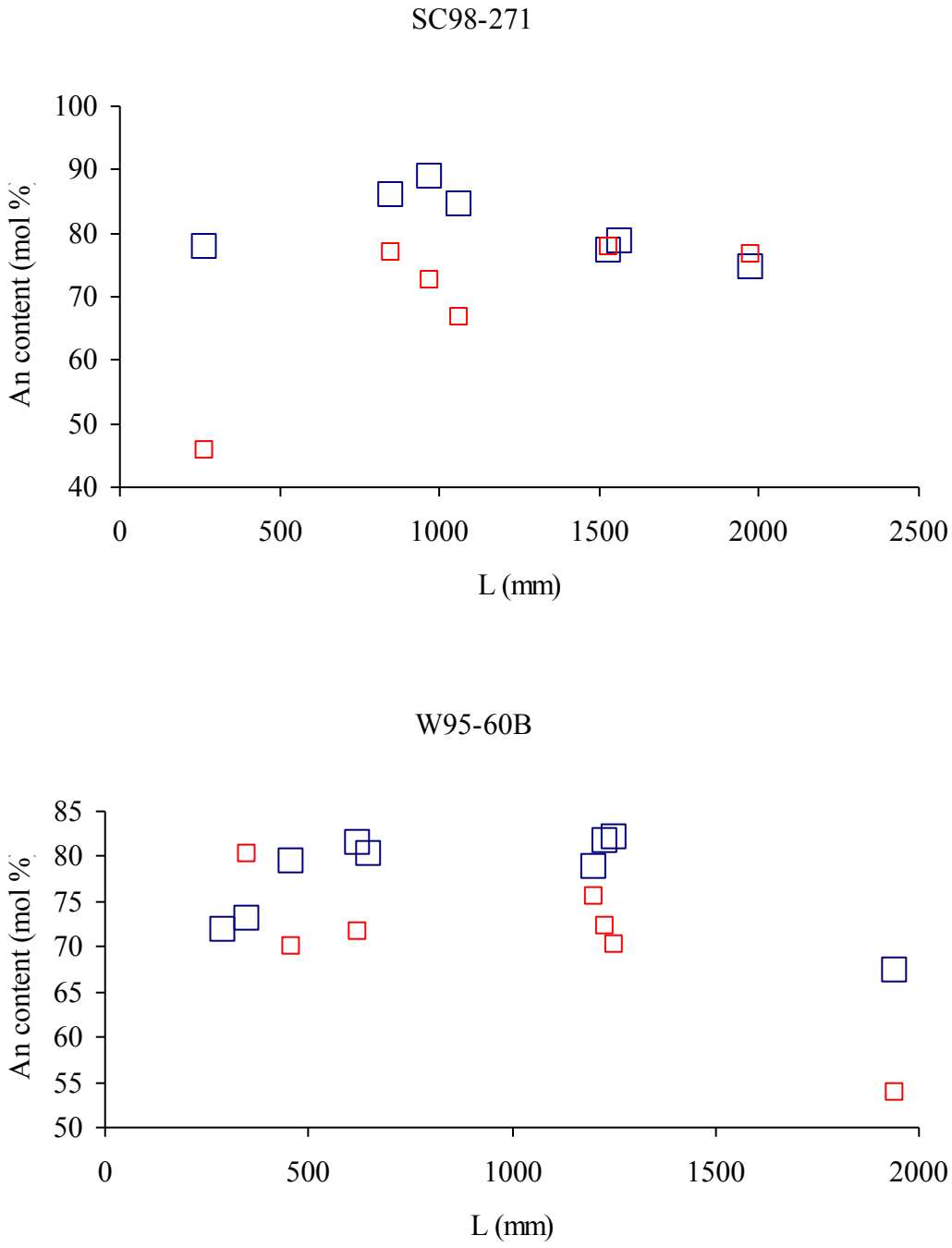

Figure 25. Plagioclase core and rim analyses versus crystal size for samples SC98-271 and W95-60B. Blue squares represent core compositions; red squares are rim compositions.

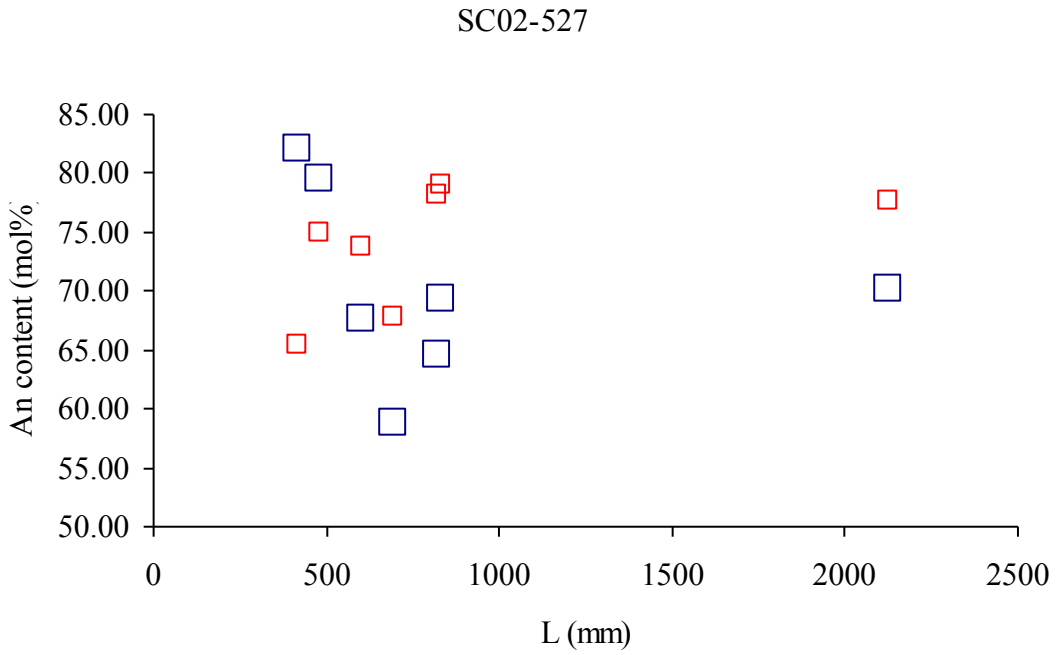

Figure 26. Plagioclase core and rim analyses versus crystal size for sample SC02-527. Blue squares represent core compositions; red squares are rim compositions.

and textural complexity within plagioclase crystals from Castle Creek basalts and to fully evaluate the record of magma chamber processes embedded within these crystals.

Crystal Size Distributions

Average crystal residence times were calculated using equation 2, with an assumed growth rate between 10^{-9} and 10^{-10} mm/s for phenocrysts and a range between $3 * 10^{-7}$ to $6 * 10^{-8}$ mm/s for microphenocrysts (Cashman and Marsh (1998) and Cashman (1993)). For phenocrysts, average residence times range between 3 and 6 years for the 10^{-9} mm/s growth rate and 30 and 60 years for the 10^{-10} mm/s growth rate. Microphenocryst

average residence times for the 3 * 10^{-7} mm/s growth rate are 2 to 4 days while the 6 x 10^{-8} mm/s rate yields 10 to 19 day average residence times. All ages are based on slope data from CSD plots (Figures 27, 28 and 29). In some cases, regression of the slope of the relevant CSD yields large uncertainties (i.e., poor R^2); in order to try to constrain the range of average residence times represented by individual crystal populations, multipleregression lines were fit to the phenocryst population of sample SC99-301. Using a minimum of 3 data points, regression lines were fit to the steepest and shallowest portions of the phenocryst data array. The minimum crystallization time determined by this method, calculated using the 10^{-10} mm/s growth rate is approximately 15 years. The maximum age, based on the shallowest slope, is 52,850 years. Because of the mathematical relationship that exists between time, slope and growth rate, approximately 85% of all slope values yield ages between 15 and 100 years.

The differences between the microphenocryst and phenocryst arrays in all 5 CSDs of this study are very similar. The size range at which the change in slope occurs is approximately 0.5 mm for all CSDs. Crystal size distributions with kinked shapes and multiple crystal populations have been interpreted in a number of ways. Crystal size distributions have been shown, in certain instances, to be recorders of magma chamber processes such as magma mixing (e.g., Salisbury, 2003). In this case the abrupt temperature change associated with mixing of contrasting magmas causes plagioclase nucleation and growth, and thus changes the slope of the CSD (Salisbury, 2003; Marsh 1998; Cashman and Marsh, 1998). The smaller, more steeply sloped population (typically referred to as microlites) has also been interpreted as forming by ascent driven

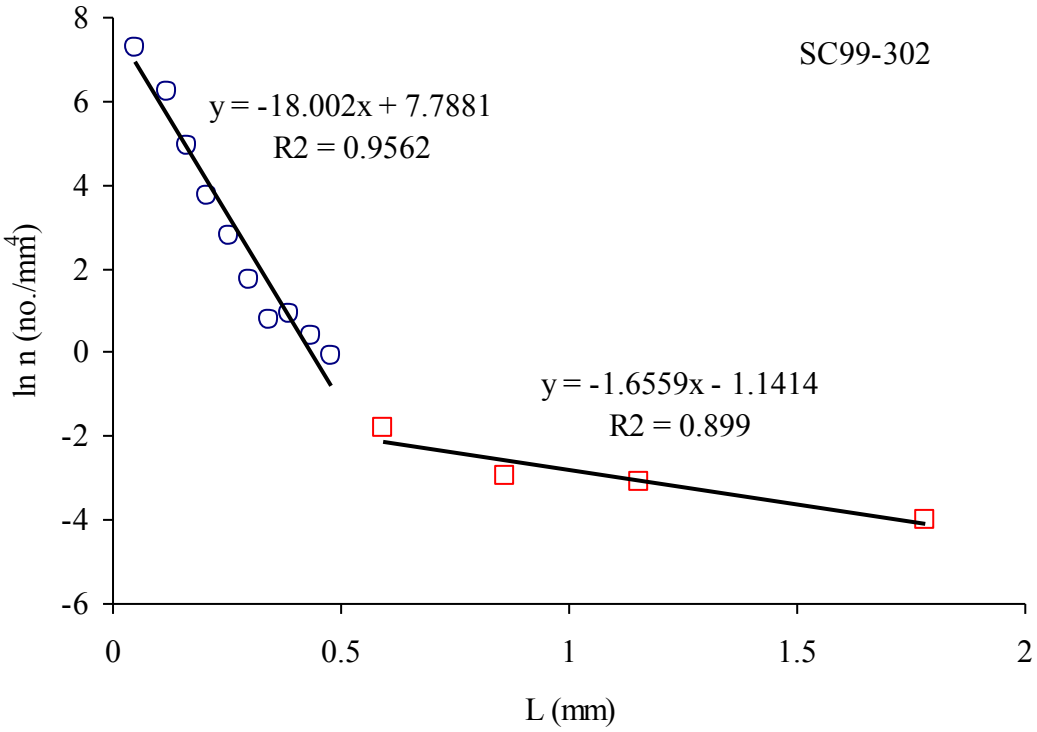

Figure 27. Plagioclase CSD for sample SC99-302. Red squares represent phenocrysts, blue circles represent microphenocrysts.

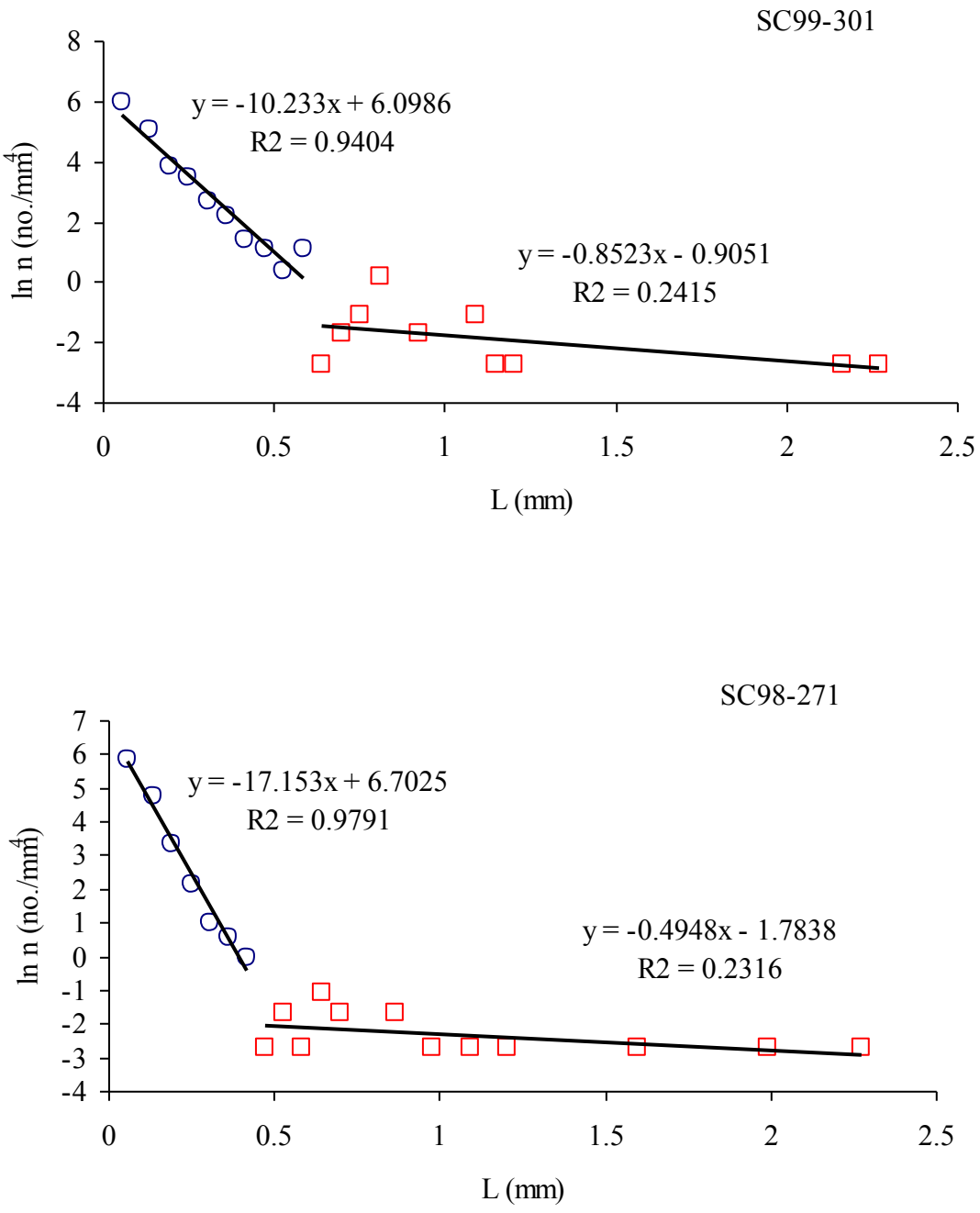

Figure 28. Plagioclase CSDs for samples SC99-301 and SC98-271. Red squares represent phenocrysts, blue circles represent microphenocryst

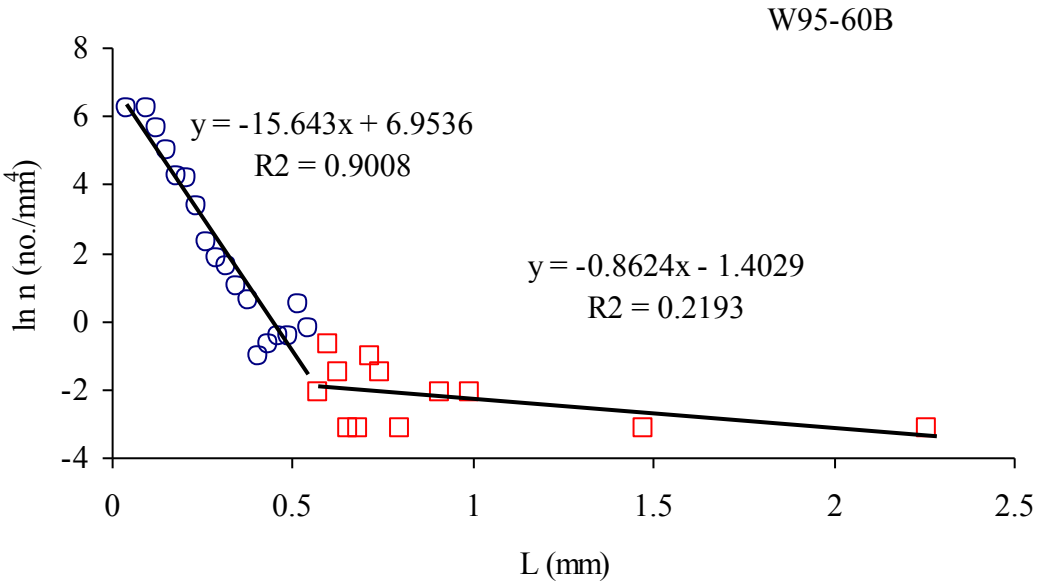

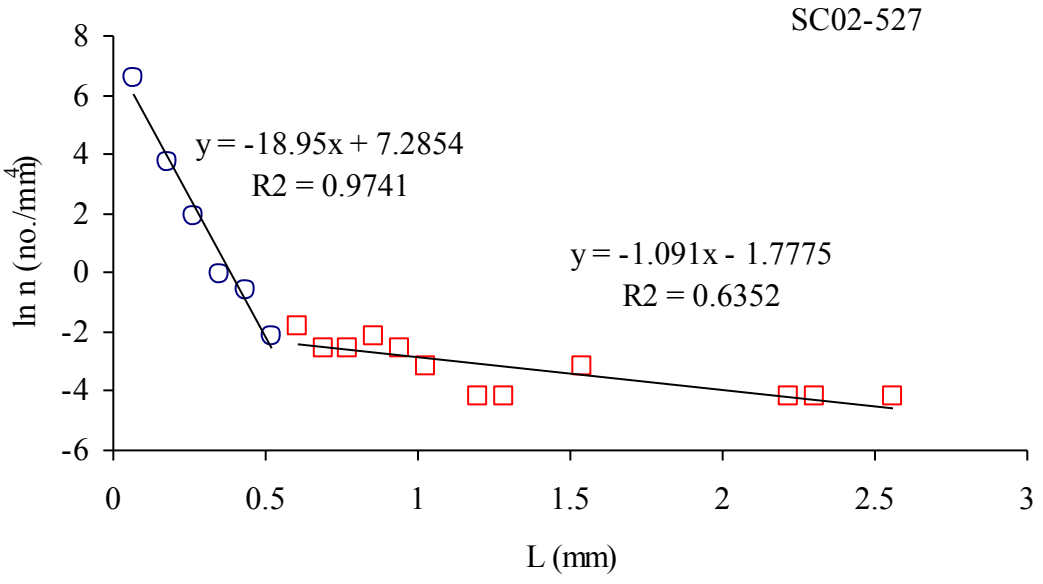

Figure 29. Plagioclase CSDs for samples W95-60B and SC02-527. Red squares represent phenocrysts, blue circles represent microphenocrysts.

crystallization in the conduit. The large amount of undercooling caused by decompression and degassing can alter the nucleation and growth rate of plagioclase dramatically, compared to those in a magma chamber (Cashman, 1993). Marsh (1998) argues that CSDs are an integration of multiple nucleation events. As in the previous scenario, kinked CSDs may be the combination of a deep and a shallow nucleation event. The author also argues that growth rate can be size dependant. This scenario could create a curved distribution if larger crystals grow more slowly than smaller crystals.

Plagioclase CSDs from Castle Creek basalts may be interpreted as representing any one or a reasonable combination of these scenarios. There does not seem to be a strong relationship between crystal chemistry and CSD measurements. CSD data suggest that each lava flow analyzed may have experienced a similar thermal history with initial conditions dominated by crystal growth and later by crystal nucleation. Crystal residence times calculated from CSDs reveal crystal growth occurred over timescales of days to decades for all samples analyzed. More detailed analysis of plagioclase crystal chemistry could reveal a relationship between CSD data and crystal chemistry. Furthermore, CSDs performed on andesite and dacite of Castle Creek affinity could elucidate thermal histories for those rocks, and then could be compared to results from basalt CSDs. This exercise would allow for more complete testing of AFC and magma mixing hypotheses.

CHAPTER V

CONCLUSION

Summary

Mount St. Helens (MSH) volcano in southwestern Washington has intermittently erupted mainly dacite products for the last 40,000 years. On limited occasions the volcano has produced andesite lava flows, and during one short-lived period, basaltic lava flows. This time interval has been termed the Castle Creek eruptive period and occurred between approximately 2500 and 1700 years B.P. The Castle Creek period erupted dacite, andesite and basalt within this short span of time, and all basaltic units were erupted in approximately the last 100 years of the episode. This is the only known occurrence of basaltic eruptive products at MSH, and yet these lava flows were a major contributor to the buildup of the modern stratocone associated with Mount St. Helens. Three litho-stratigraphic units have been recognized by this thesis within the basalts of Castle Creek; from youngest to oldest they are: the Cave basalt, Precave basalt and North Flank basalt. Petrogenetic relations between these units of the Castle Creek eruptive period provide insight into the nature of the subjacent magma chamber during Castle Creek time.

MELTS simulations reveal primitive Cave basalt can be related to most Precave basalts, andesite and dacite compositions of Castle Creek age through isobaric fractional crystallization at low pressures (2 kbar) and water contents (1 wt%). MELTS predicts fractionating phase assemblages that contain plagioclase, olivine, clinopyroxene, orthopyroxene, magnetite and minor amounts of apatite. This phase assemblage is in agreement with observed mineralogy of MSH basalts. Plagioclase compositions

predicted by MELTS range between approximately An_{52} and An_{76}. Observed values span a composition range of $An_{48–89}$. Olivine compositions as predicted by MELTS are approximately Fo_{82} for the Cave model and Fo_{90} for the North Flank model. This is in agreement with the findings of Smith and Leeman (2005), who analyzed olivine from MSH lavas by EMP and recorded compositions between $Fo_{83–84}$. MELTS predicts 27% of the 82% of solids fractionated from the system are pyroxene for the Cave model. This is in distinct contrast to the 2-5% modal pyroxene found in Cave basalt. This suggests the model is not simulating perfectly the crystallization conditions experienced by Cave magma.

Simulations of North Flank basalt evolution reveal fractional crystallization is may be operative during that time interval as well, but at slightly higher pressures (2 kbar) and the same water content. However, high initial abundances of K_2O and TiO_2, among other incompatible elements within the North Flank, preclude fractional crystallization as the only mechanism operating in the magma plumbing system.

Strontium isotopic compositions also suggest fractional crystallization alone is not responsible for variation within the basalts, as evidenced by the relatively large range of $^{87}Sr/^{86}Sr$ ratios (approximately 0.7030-0.7034) and increasing $^{87}Sr/^{86}Sr$ ratios with decreasing whole rock MgO contents. This suggests Castle Creek basaltic magma experiences either assimilation or magma mixing, or both, during its evolution. Despite compositional data that suggest complex processing in the magma plumbing system, crystal size distribution data suggest that basalts experienced similar growth conditions and thermal histories because CSD plots reveal similar behavior in all five samples. Plagioclase feldspar from basalt samples, based on regression of CSD data, had

maximum average residence times between 30 and 60 years. That this number is within the timeframe of basaltic volcanism at MSH suggests that plagioclase could have recorded in detail open-system behavior influencing magmatic compositions during Castle Creek time.

Eruption of such a large range of magmatic compositions within the Castle Creek eruptive period suggests the magma reservoir system at MSH during Castle Creek time was sufficiently complex to allow for interaction of discreet magma batches. Petrologic evidence favors these postulations as data suggest interaction between discrete magma batches may have occurred during Castle Creek time and may be responsible for much of the compositional diversity that is not easily explained by simple fractional crystallization of typical phases associated with basaltic volcanism. Furthermore, data presented in this thesis suggest two end member basalt groups exist at MSH during Castle Creek time, Cave and North Flank. Precave basalt, which is both stratigraphically and (approximately) compositionally intermediate, may indicate interaction between the Cave and North Flank basalts. MELTS model results qualitatively support this postulation as well, as models of both end member liquids can reproduce observed chemistry.

Future Work

Future work to better document magmatic processes during Castle Creek time should include MELTS simulations of the same parental compositions used in this thesis in polybaric fractional crystallization simulations. This may result in a predicted phase assemblage that more closely approximates observed mineralogy, thereby producing a better fit of the model to major element variations. This would contribute to a better

understanding of the role that fractional crystallization played during Castle Creek time. Detailed analysis of trace elements will also shed light on the importance of fractional crystallization. Based on the Sr isotope results presented here, it is clear that open-system processes play a role in the evolution of Castle Creek magmas. It is possible that these magmas experienced assimilation; this hypothesis can be addressed through collection of additional isotope data on the basalts. Quantitative modeling may also be appropriate. Further exploration of the magma mixing model is also important. A critical aspect of this approach includes conducting quantitative modeling of whole rock major and trace element data. Additional electron microprobe analyses of phenocryst phases within basalts, andesites and dacites will further constrain the genetic relationships of each, including the possible role of magma mixing. Of particular interest, detailed phase compositional data may reveal evidence for magma mixing by elucidating by crystal sharing histories.

Additional data collected on the andesites and dacites, including Sr isotopes and mineral chemical data, may provide insight into the petrogenetic relationships these rocks have with Castle Creek basalts. Such data would allow for a more robust test of models that involve magma mixing of basalt and dacite to produce andesites. These data would also inform the hypothesis of Smith and Leeman which calls upon crustal melting to produce dacite (Smith and Leeman, 1993; Smith and Leeman, 1987).

REFERENCES CITED

Anderson, A. T., 1983, Oscillatory zoning of plagioclase: nomarski interference contrast microscopy of etched polished thin sections: American Mineralogist, v. 68, p. 125-129

Asimow, P. D., and Ghiorso, M. S., 1998, Algorithmic modifications extending MELTS to calculate subsolidus phase relations: American Mineralogist, v. 83, p. 1127-1131.

Atwater, T., 1970, Implications of plate tectonics for the Cenozoic tectonic evolution of western North America: GSA Bulletin, v. 81, p. 3513-3535.

Browne, B. L., Dehn, J., Uto, K., Hoshizumi, H., Eichelberger, J. C., Patino, L. C., and Vogel, T. A., 2006, Generation of porphyritic and equigranular mafic enclaves during magma recharge evens at Unzen volcano, Japan: Journal of Petrology, v. 47, p. 301-328.

Cashman, K. V., 1993, Relationship between plagioclase crystallization and cooling rate in basaltic melts: Contributions to Mineralogy and Petrology, v. 113, p. 126-142.

Cashman, K. V., and Marsh, B. D., 1998, Crystal size distribution (CSD) in rocks and the kinetics and dynamics of crystallization II: Makaopuhi lava lake: Contributions to Mineralogy and Petrology, v. 99, p. 292-305.

Clynne, M. A., 1999, A complex magma mixing origin for rocks erupted in 1915, Lassen Peak, California: Journal of Petrology, v. 40, p. 105-132.

Clynne, M. A., Champion, D. E., Wolfe, E. W., Gardner, C. A., Pallister, J. S., 2004, Stratigraphy and paleomagnetism of the Pine Creek and Castle Creek eruptive episodes, Mount St. Helens, Washington: Eos Trans. American Geophysical Union, vol. 85.

Crosson, R. S., and Owens, T. J., 1987, Slab geometry of the Cascadia subduction zone beneath Washington from earthquake hypocenters and teleseismic converted waves: Geophysical Research Letters, v. 14, p. 824-827.

Davidson, J. P., and Tepley, F. J., 1997, Recharge in volcanic systems: evidence from isotope profiles of phenocrysts: Science, v. 275, p. 826-829.

DePaolo, D. J., 1981, Trace element and isotopic effects of combined wallrock assimilation and fractional crystallization: Earth and Planetary Science Letters, v. 53, p. 189-202.

DePaolo, D. J., Perry, F. V., and Baldridge, W.S., 1992, Crustal versus mantle sources of granitic magmas: a two-parameter model based on Nd isotopic studies: Transactions of the Royal Society of Edinburgh: Earth Sciences, v. 83, p. 439-446.

Duncan, R. A., 1982, A captured island arc chain in the Coast Range of Oregon and Washington: Journal of Geophysical Research, v. 87, p. 10827-10837.

Dungan, M. A., 1987, Open system magmatic evolution of the Taos plateau volcanic field, northern New Mexico: II. The genesis of cryptic hybrids, Journal of Petrology, v. 28, p. 955-977.

Eichelberger, J. C., 1978, Andesitic volcanism and crustal evolution: Nature, v. 275, p. 21-27.

Eichelberger, J. C., and Izbekov, P.E., 2000, Eruption of andesite triggered by dyke injection: contrasting cases at Karymsky Volcano, Kamchatka and Mt. Katmai, Alaska: Philosophical Transactions of the Royal Society A: Mathematical, Physical, and Engineering Sciences, v. 358, p. 1465-1485.

Evarts, R. C., Ashley, R.P. and Smith, J.G., 1987, Geology of the Mount St. Helens area: record of discontinuous volcanic and plutonic activity in the Cascade arc of southern Washington: Journal of Geophysical Research, v. 92, p. 155-169.

Ghiorso, M. S., and Sack, R. O., 1995, Chemical mass transfer in magmatic processes IV: a revised and internally consistent thermodynamic model for the interpolation and extrapolation of liquid-solid equilibria in magmatic systems at elevated temperatures and pressures: Contributions to Mineralogy and Petrology, v. 119, p. 197-212.

Gualda, G. A. R., 2006, Crystal size distributions derived from 3D datasets; sample size versus uncertainties: Journal of Petrology, v. 47, p. 1245-1254.

Guffanti, M., and Weaver, C. S., 1988, Distribution of late Cenozoic volcanic vents in the Cascade range: volcanic arc segmentation and regional tectonic considerations: Journal of Geophysical Research, v. 93, p. 6513-6529.

Halliday, A. N., Fallick, A. E., Dickin, A. P., Mackenzie, A. B., Stephens, W. E., and Hildreth, W., 1983, The isotopic and chemical evolution of Mount St. Helens: Earth and Planetary Science Letters, v. 63, p. 241-256.

Knesel, K. M., Davidson, J. P., Duffield, W. A., 1999, Evolution of silicic magma through assimilation and subsequent recharge: evidence from Sr isotopes in sanidine phenocrysts, Taylor Creek rhyolite, NM: Journal of Petrology, v. 40, p. 773-786.

Marsh, B. D., 1998, On the interpretations of crystal size distributions in magmatic systems: Journal of Petrology, v. 39, p. 553-599.

Maury, R. C., Bizouard, H., 1974, melting of acid xenoliths into a basanite: an approach to the possible mechanisms of crustal contamination: Contributions to Mineralogy and Petrology, v. 48, p. 275-286.

McBirney, A. R., Taylor, H. P., and Armstrong, R. L., 1987, Paricutin re-examined: a classic example of crustal contamination in calc-alkaline magma: Contributions to Mineralogy and Petrology, v. 95, p. 4-20.

Michaelson, C. A., and Weaver, C. S., 1986, Upper mantle structure from teleseismic P wave arrivals in Washington and nothern Oregon: Journal of Geophysical Research, v. 91, p. 2077-2094.

Miller, M. M., Melbourne, T. I., Johnson, D. J., Sumner, W. Q., 2002, Periodic slow earthquakes from the Cascadia subduction zone: Science, v. 295, p. 2423.

Mooney, W. D., and Weaver, C. S., 1989, Regional crustal structure and tectonics of the Pacific coastal states; California, Oregon and Washington: Geological Society of America Memoir, v. 172, p. 129-161.

Mullineaux, D. R., and Crandell, D. R., 1981, The eruptive history of Mount St. Helens, *in* Lipman, P. W., and Mullineaux D. R., ed., The 1980 eruptions of Mount St. Helens, Washington: Geological Survey Professional Paper 1250, p. 3-15.

Parsons, T., Tréhu, A. M., Luetgert, J. H., Miller, K., Kilbride, F., Wells, R. E., Fisher, M. A., Flueh, E., Brink, U. T., and Christensen, N. I., 1998, A new view into the Cascadia subduction zone and volcanic arc: implications for earthquake hazards along the Washington margin: Geology, v. 26, p. 199-202.

Parsons, T., Wells, R. E., Flueh, E., ten Brink, U. S., and Fisher, M. A., 1999, Three-dimensional velocity structure of Siletzia and other accreted terranes in the Cascadia fore arc of Washington: Journal of Geophysical Research, v. 104, p. 18015-18039.

Perry, F. V., DePaolo, D. J., and Baldridge, W. S., 1993, Neodymium isotopic evidence for decreasing crustal contributions to Cenozoic ignimbrites of the western United States; implications for the thermal evolution of the Cordilleran crust: GSA Bulletin, v. 105, p. 872-882.

Petford, N., Cruden A. R., McCaffrey, K. J. W. and Vigneresse, J. L., 2000, Granite magma formation, transport and emplacement in the Earth's crust: Nature 408, p. 669-673.

Ramos, F. C., and Reid, M. R., 2005, Distinguishing melting of heterogenous mantle sources from crustal contamination: insights from Sr isotopes at the pheocryst scale, Pisgah Crater, California: Journal of Petrology, v. 46, no. 5, p. 999-1012

Rudnick R. L., McDonough, W. F., mcCulloch, M. T., and Taylor, S. R., 1986, Lower crustal xenoliths from Queensland, Australia: evidence for deep crustal assimilation and fractionation of continental basalts: Geochimica et Cosmochimica Acta, v. 50, p. 1099-1115.

Salisbury, M. J., 2003, Magma mixing histories recorded in plagioclase crystals from the 1915 eruption of Lassen Peak, California: Unpublished Masters Thesis, Central Washington University.

Sherrod, D. R., and Smith, J. G., 1990, Quaternary extrusion rates of the Cascade Range, northwestern United States and southern British Columbia: Journal of Geophysical Research, v. 95, p. 465-474.

Smith, D. S. and Leeman, W. P., 1987, Petrogenesis of Mount St. Helens dacitic magmas: Journal of Geophysical Research, v. 92, p. 313-334.

Smith, D. S., and Leeman, W. P., 1993. The origin of Mount St. Helens andesites: Journal of Volcanology and Geothermal Research, v. 55, p. 271-303.

Smith, D. S., and Leemnan, W. P., 2005, Chromian spinel-olivine phase chemistry and the origin of primitive basalts of the southern Washington Cascades: Journal of Volcanology and Geothermal Research, v. 140, p. 49-66.

Snavely, P. D., MacLeod, N. S., and Wagner, H. C., 1968, Tholeiitic and alkalic basalts of the Eocene Siletz River volcanics, Oregon Coast Range: American Journal of Science, v. 266, p. 454-481.

Snavely, P. D., and Wells, R. E., 1996, Cenozoic evolution of the continental margin of Oregon and Washington. In Rogers, A.M., Ed., Assessing Earthquake Hazards and Reducing Risk in the Pacific Northwest: U.S. Geol. Survey Professional Paper, 1560, p. 161-182.

Sparks, R. S. J., Sigurdsson, H., and Wilson, L., 1977, Magma mixing: a mechanism for triggering acid explosive eruptions: Nature, v. 267, p. 315-318.

Sparks, R. S. J., and Marshall, L. A., 1986, Thermal and mechanical constraints on mixing between mafic and silicic magmas: Journal of Volcanology and Geothermal Research, v. 29, p. 99-124.

Spera, F. J., and Bohrson, W. A., 2001, Energy-constrained open-system magmatic processes I: general model and energy-constrained assimilation and fractional crystallization (EC-AFC) formulation: Journal of Petrology, v. 42, p. 999-1018.

Turner, S., George, R., Jerram, D. A., Carpenter, N., and Hawkesworth, C., 2003, Case studies of plagioclase growth and residence times in island arc lavas from Tonga and the Lesser Antilles, and a model to reconcile discordant age information: Earth and Planetary Science Letters, v. 214, p. 279-294.

Watts, R. B., De Silva, S. L., De Rios, G. J., Croudace, I., 1999, Effusive eruption of viscous silicic magma triggered and driven by recharge: a case study of Cerro Chascon-Runtu Jarita dome complex in southwest Bolivia: Bulletin of Volcanology, v. 61, p. 241-264.

Weaver, C. S., Grant, W. C., and Shemata, J. E., 1987, Local crustal extension at Mount St. Helens, Washington: Journal of Geophyical Research, v. 92, p. 170-178.

Zellmer, G. F., Sparks, R. S. J., Hawkesworth, C. J., and Wiedenbeck, M., 2003, Magma emplacement and remobilization timescales beneath Montserrat: Insights from Sr and Ba zonation in plagioclase phenocrysts: Journal of Petrology, v. 44, p. 1413-1431.

APPENDICES

Appendix A

BSE and NDIC Image of Plagioclase in Sample SC99-302 with Approximate Microprobe Spot Locations. Upper image is BSE, Lower is NDIC

302-1

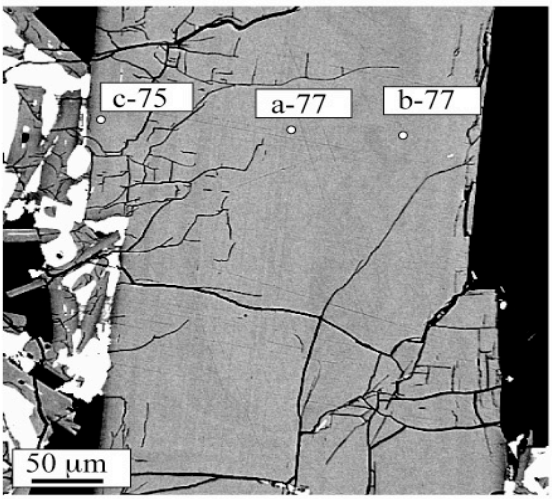

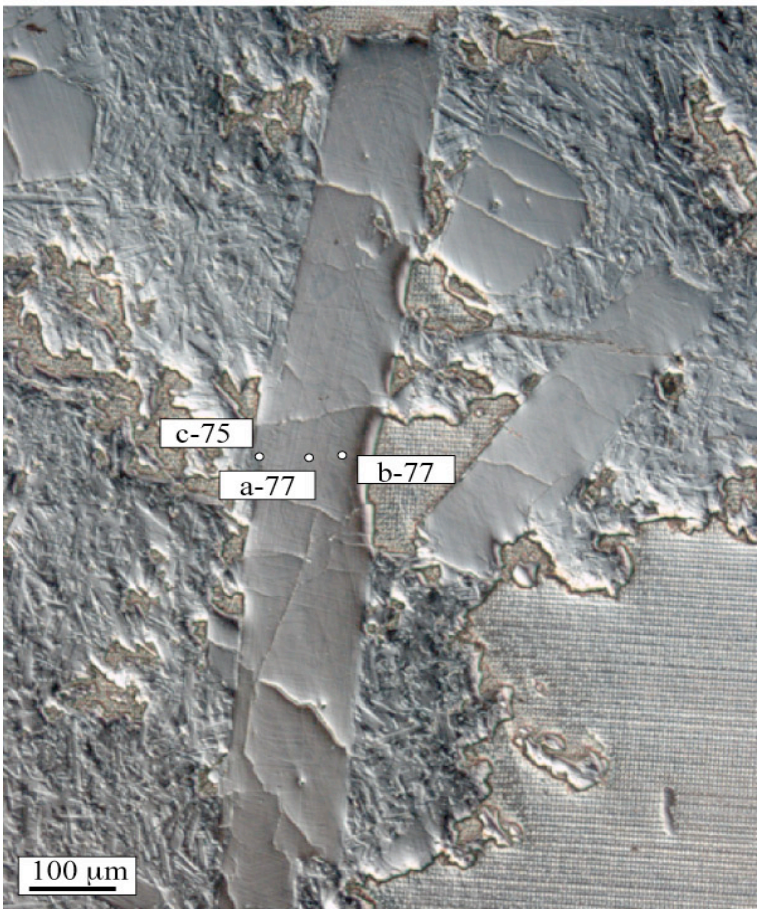

302-3

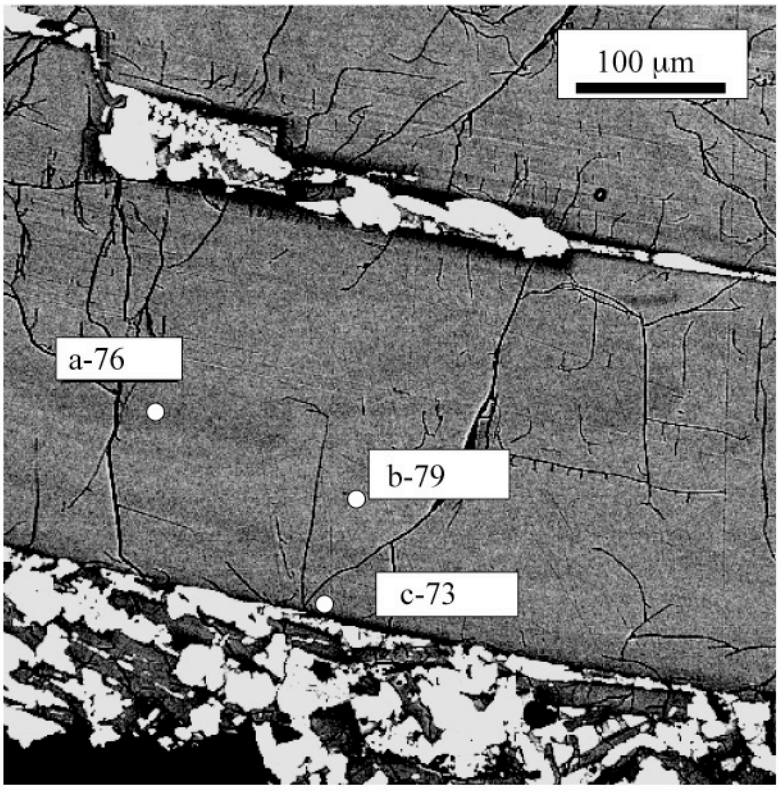

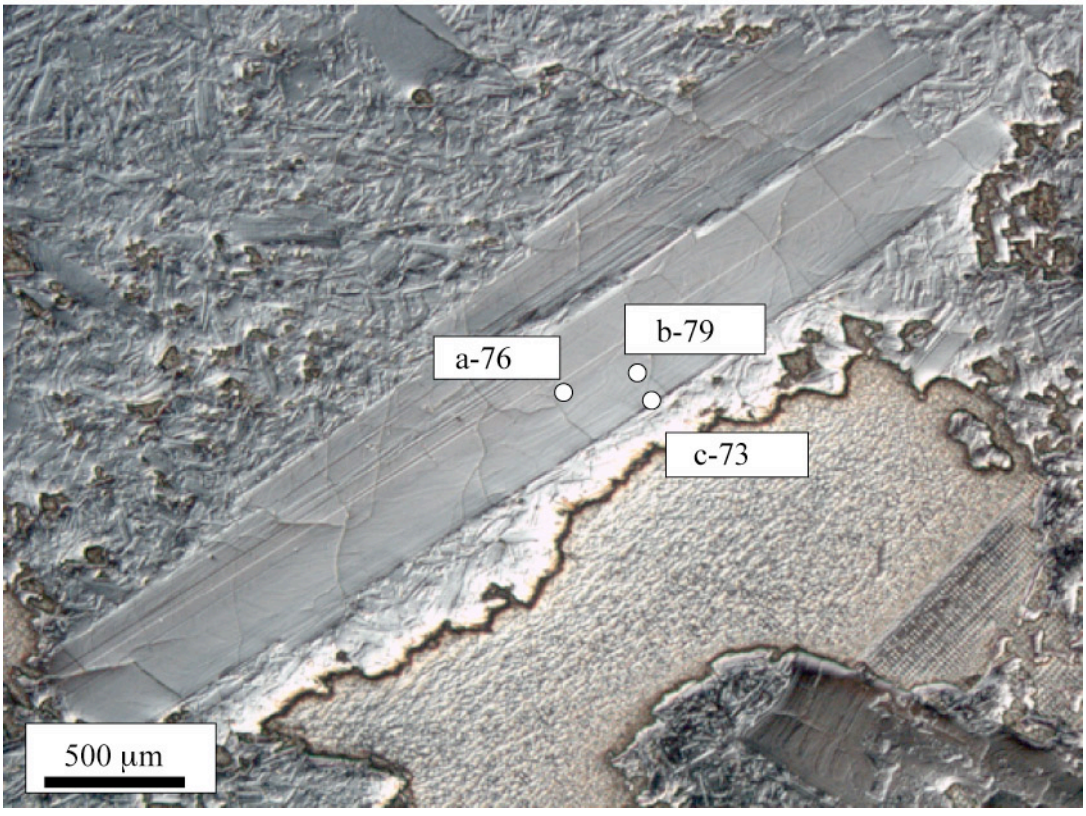

302-5

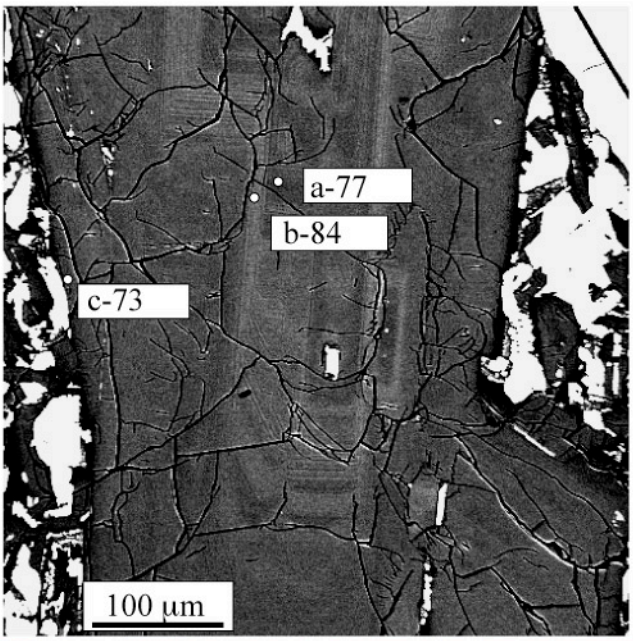

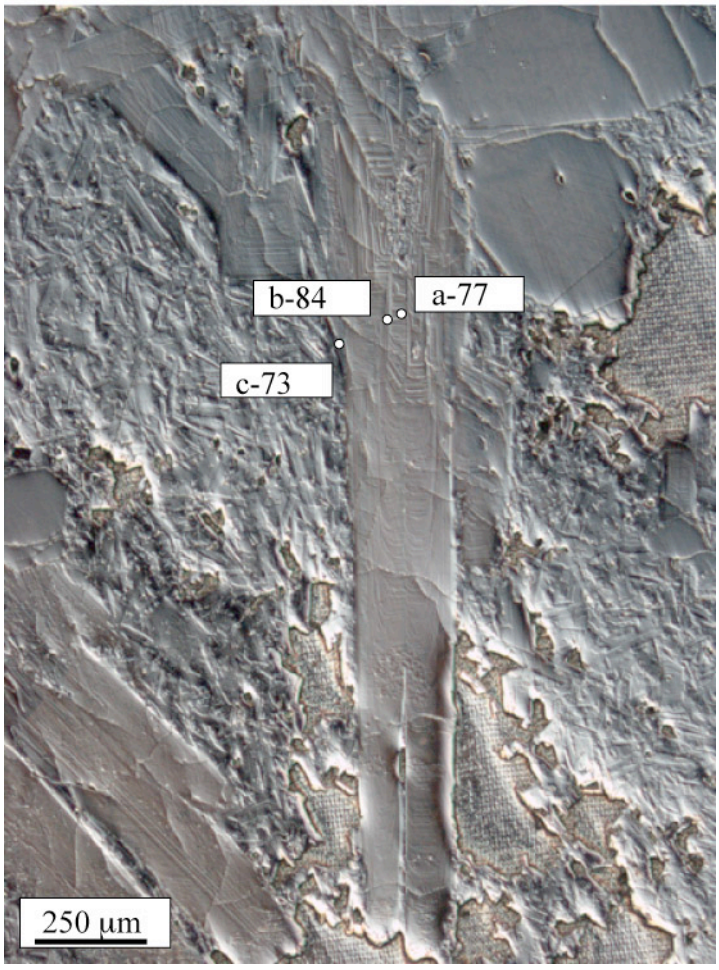

302-8

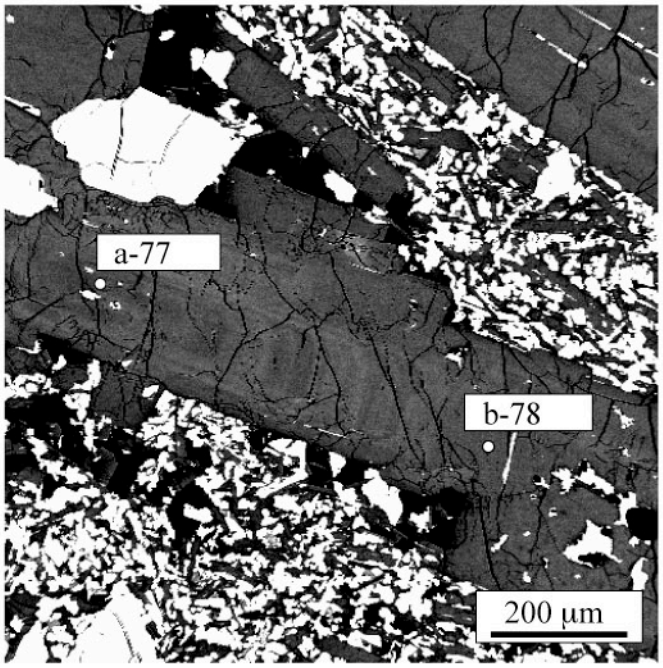

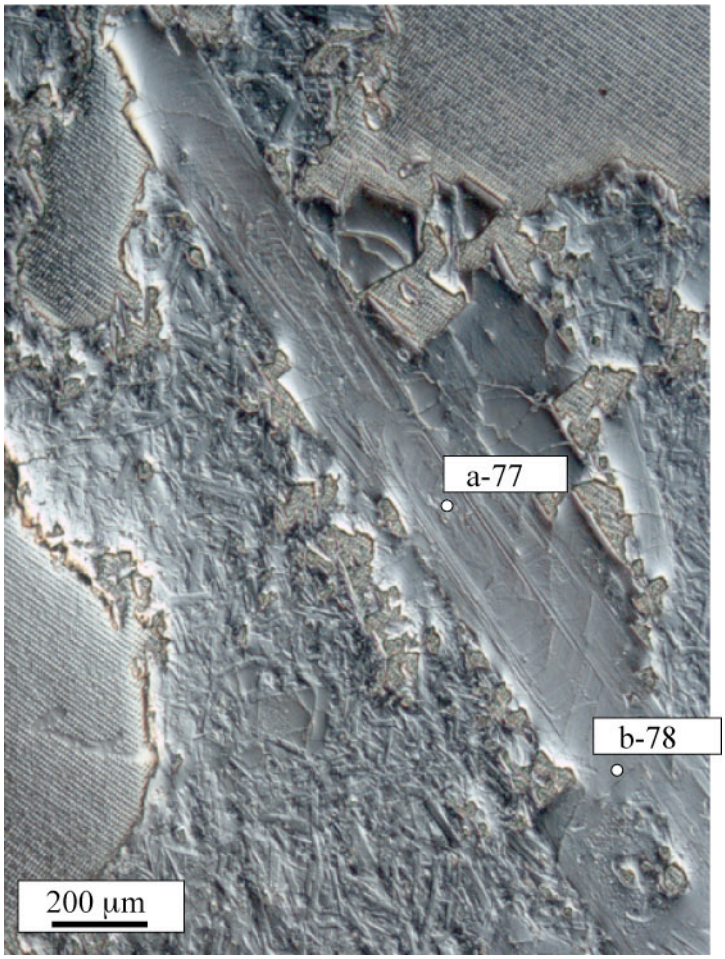

302-10

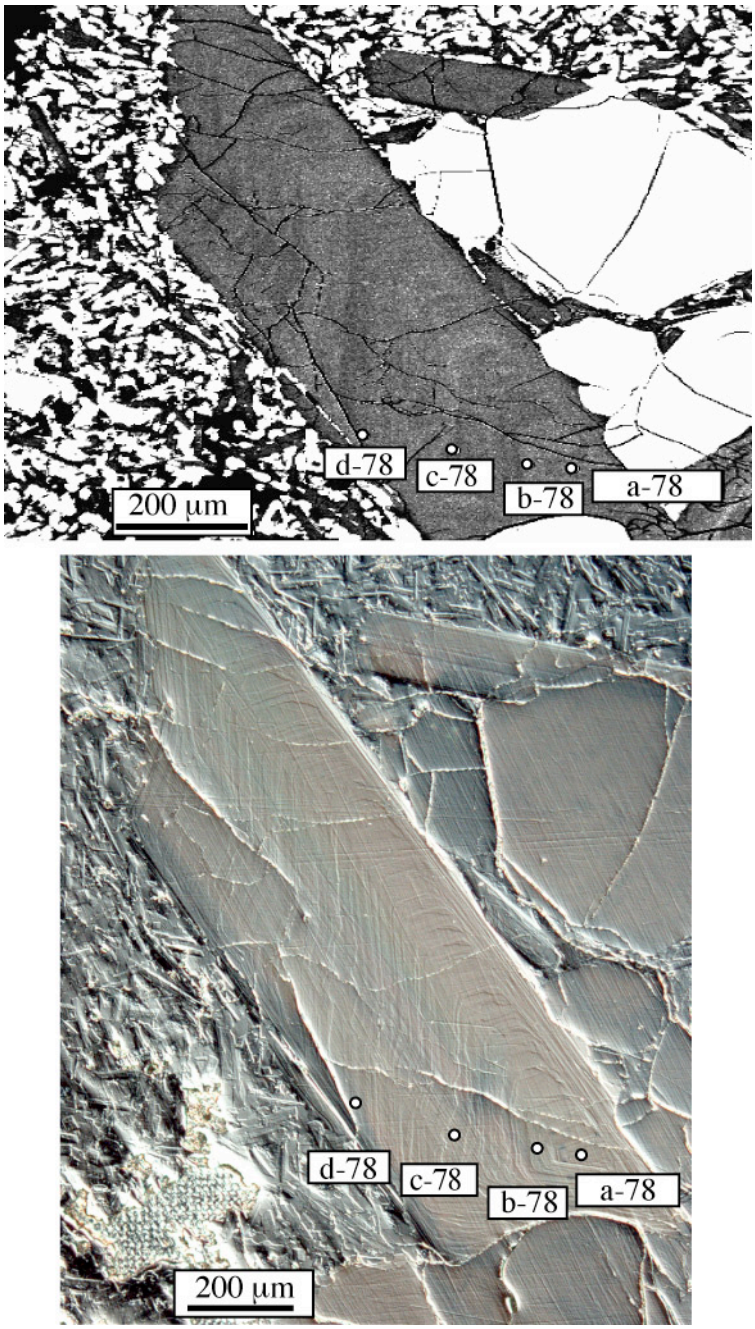

302-11

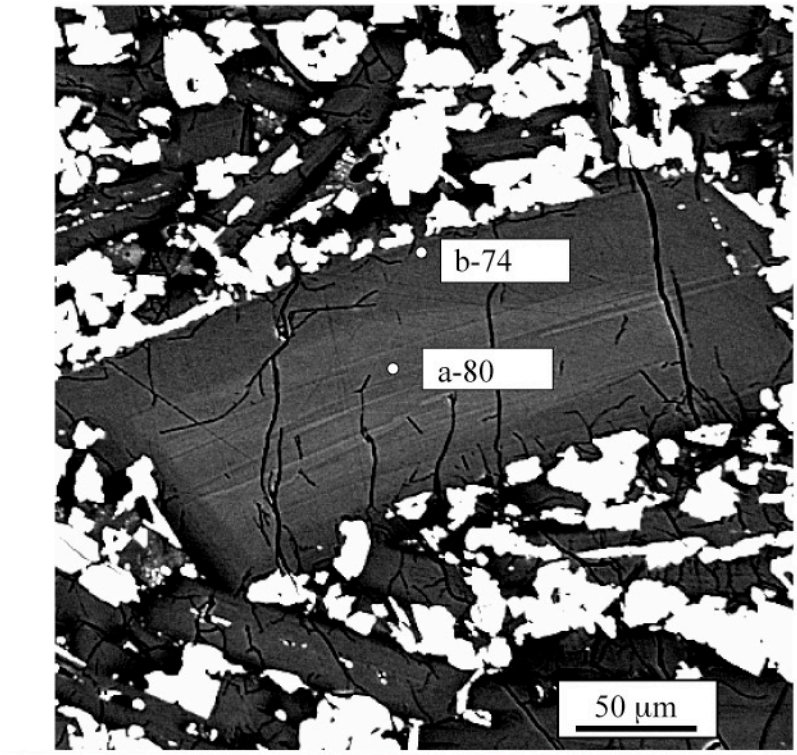

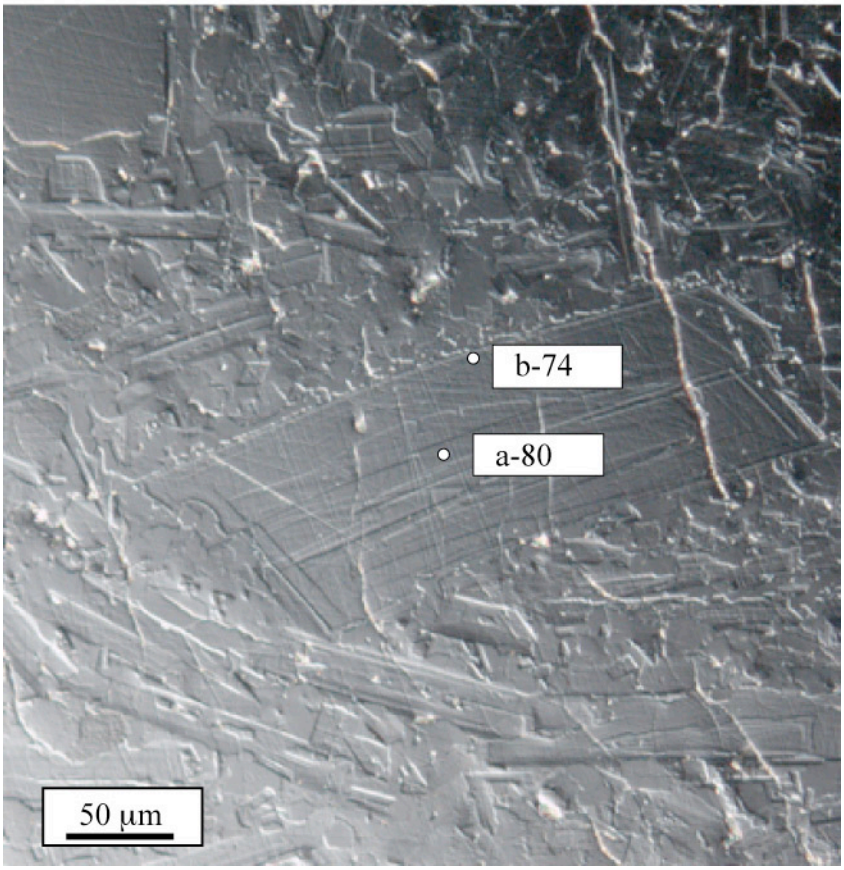

302-12

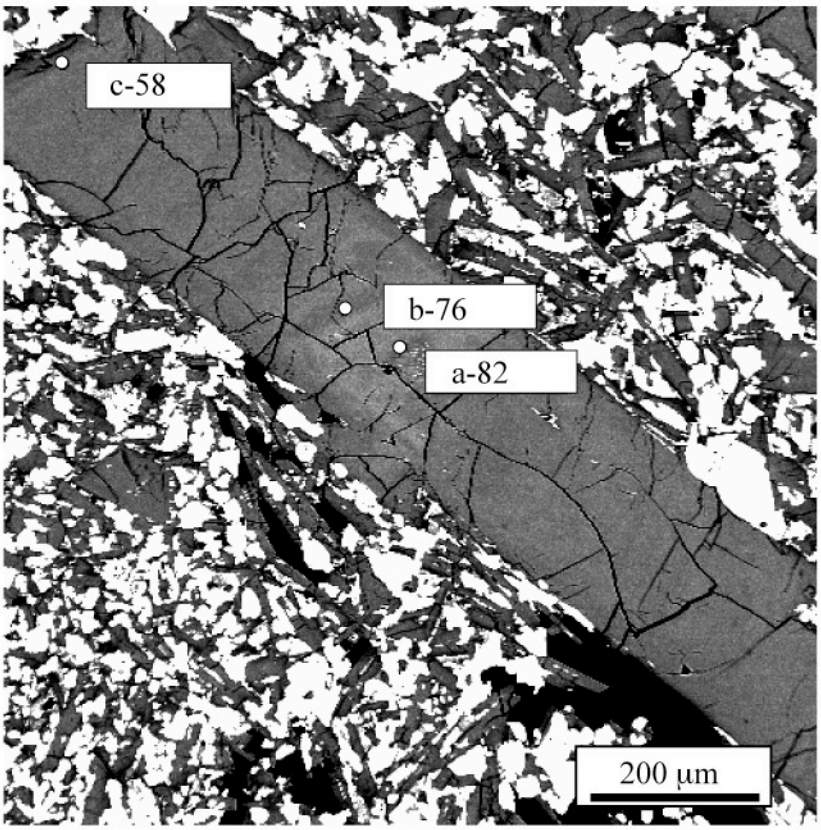

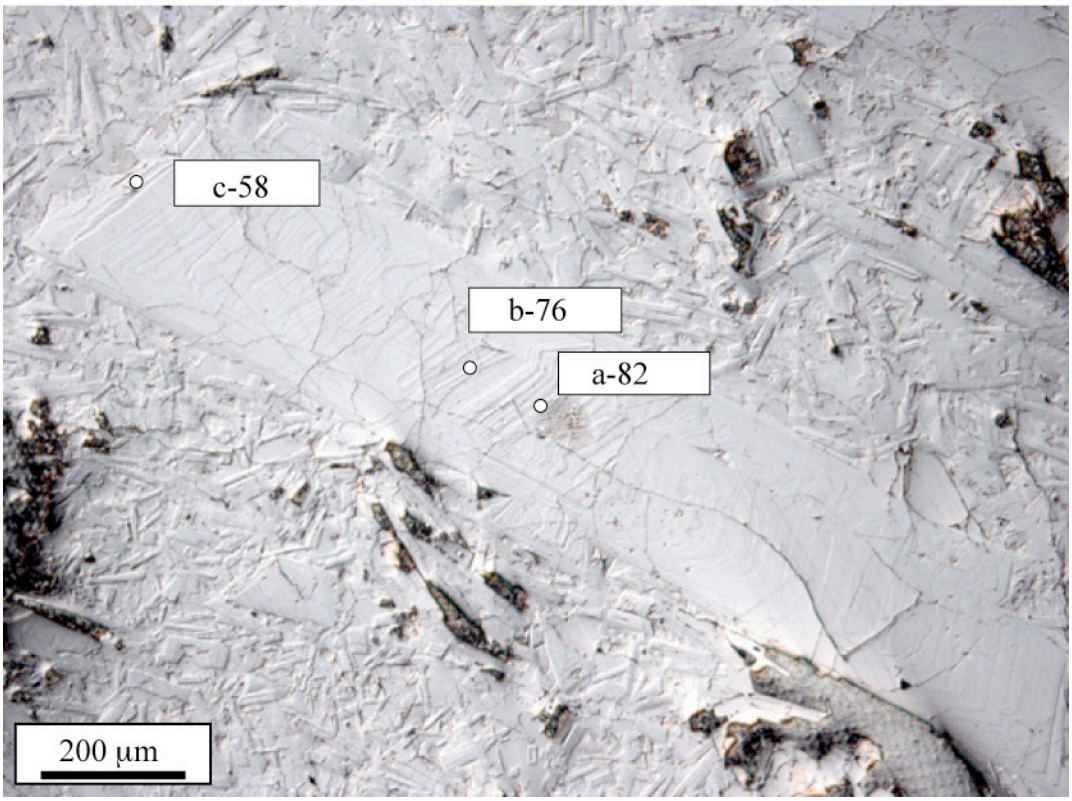

Appendix B

BSE and NDIC Images of Plagioclase in Sample SC99-301 with Approximate Microprobe spot locations. Upper image is BSE, lower image is NDIC.

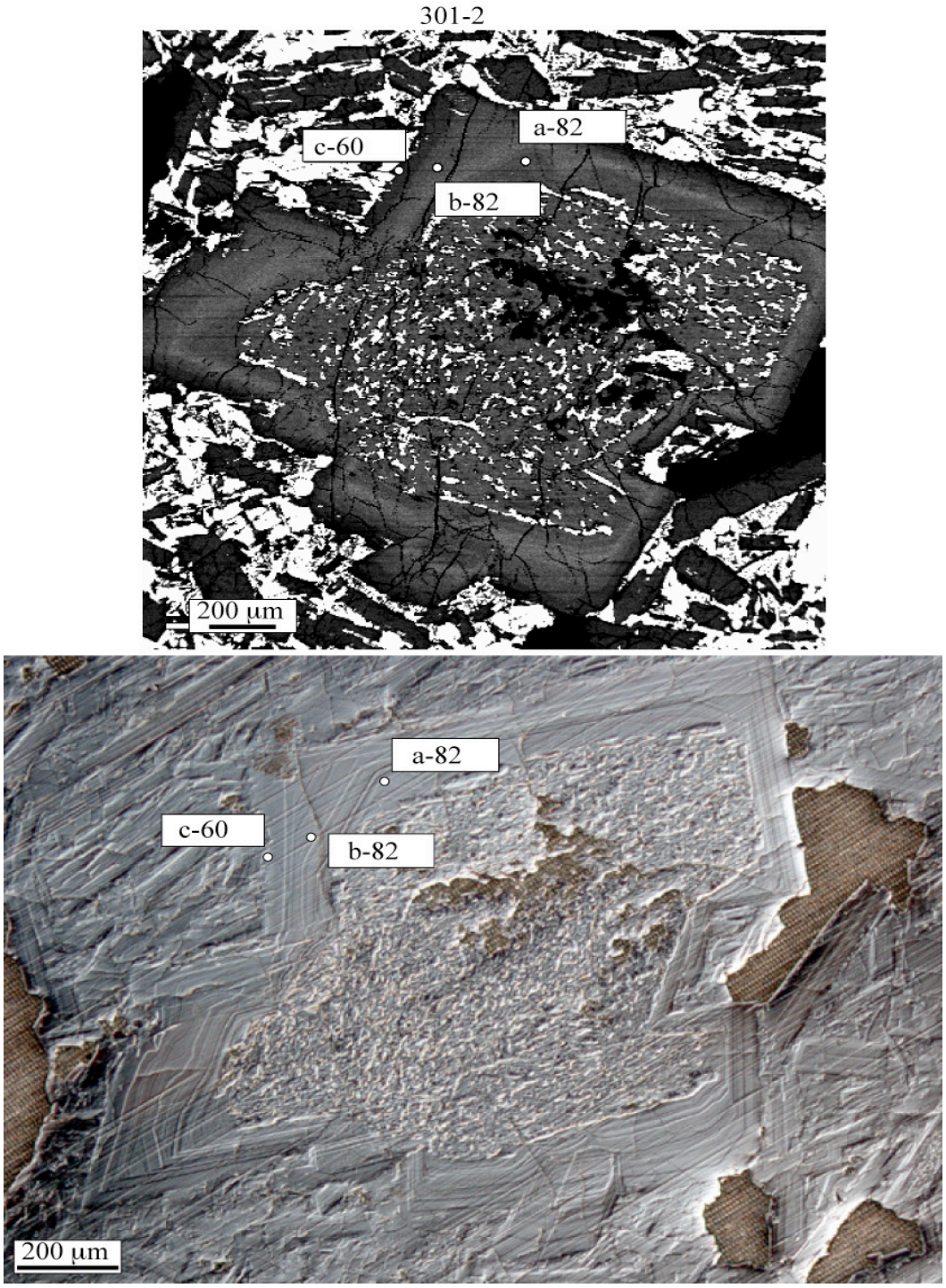

301-3

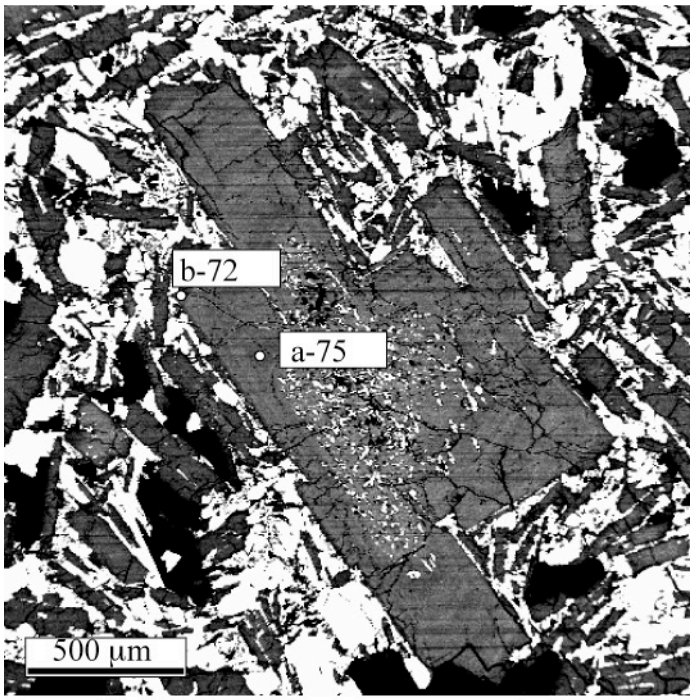

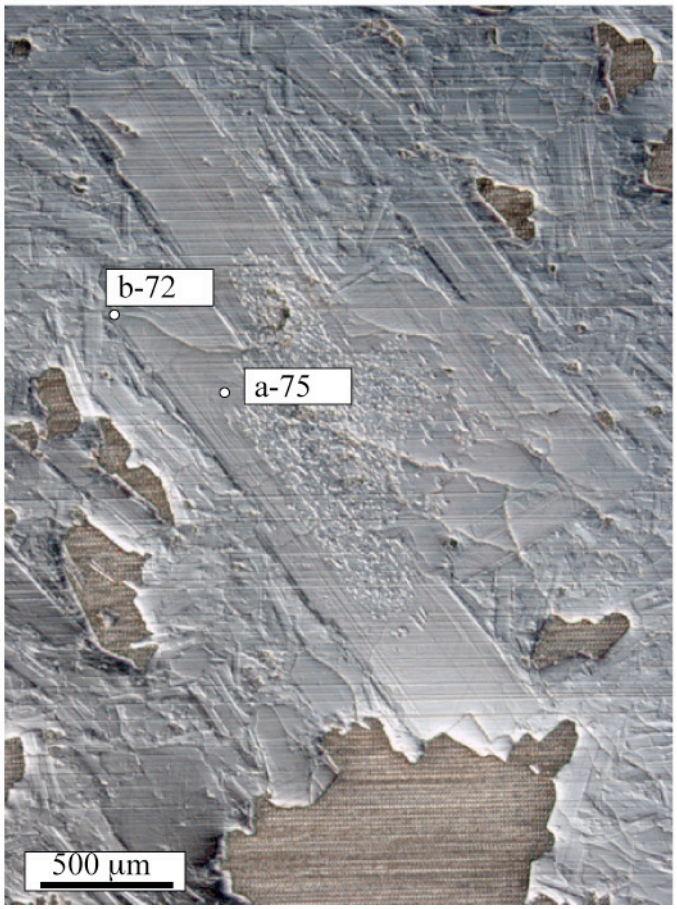

301-6

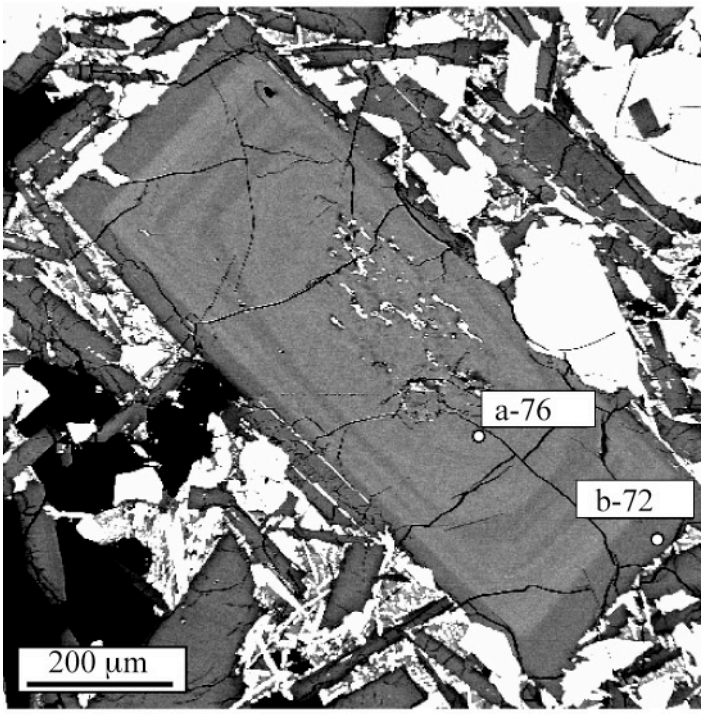

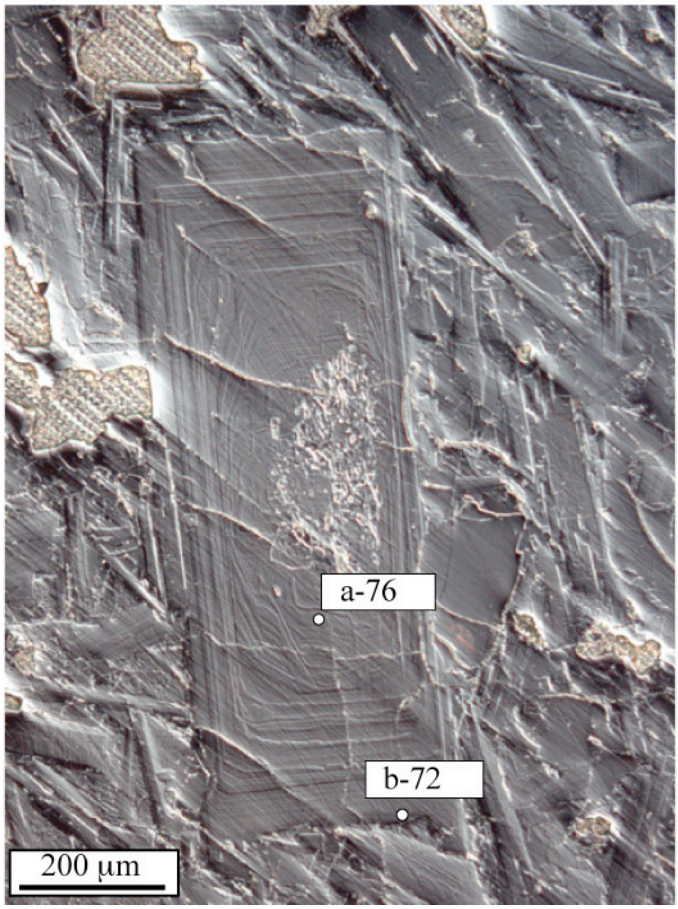

301-7

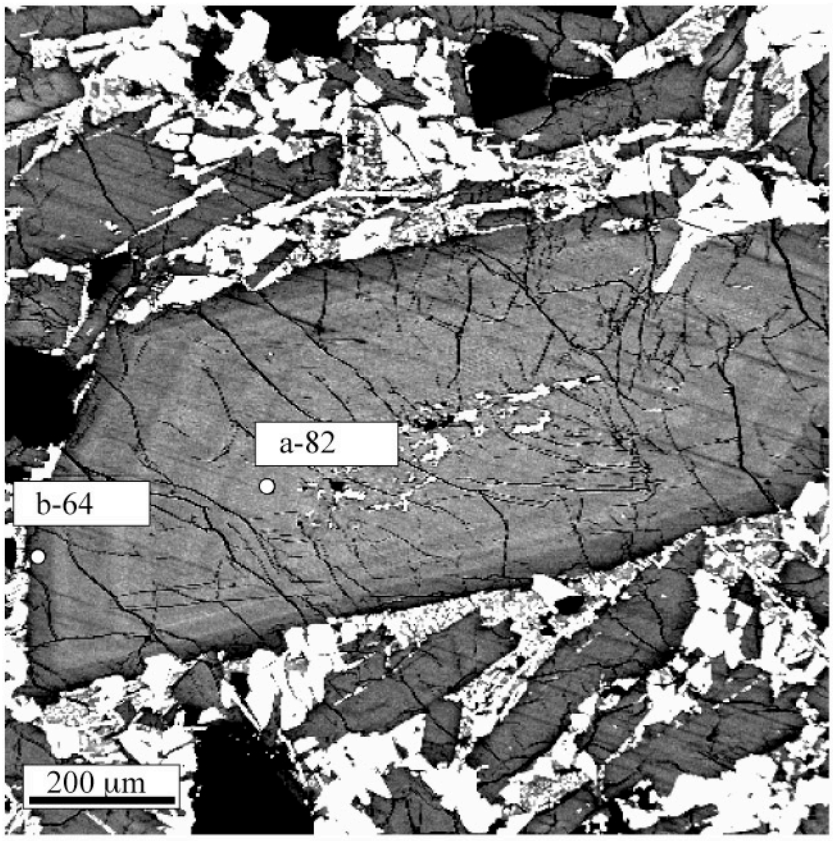

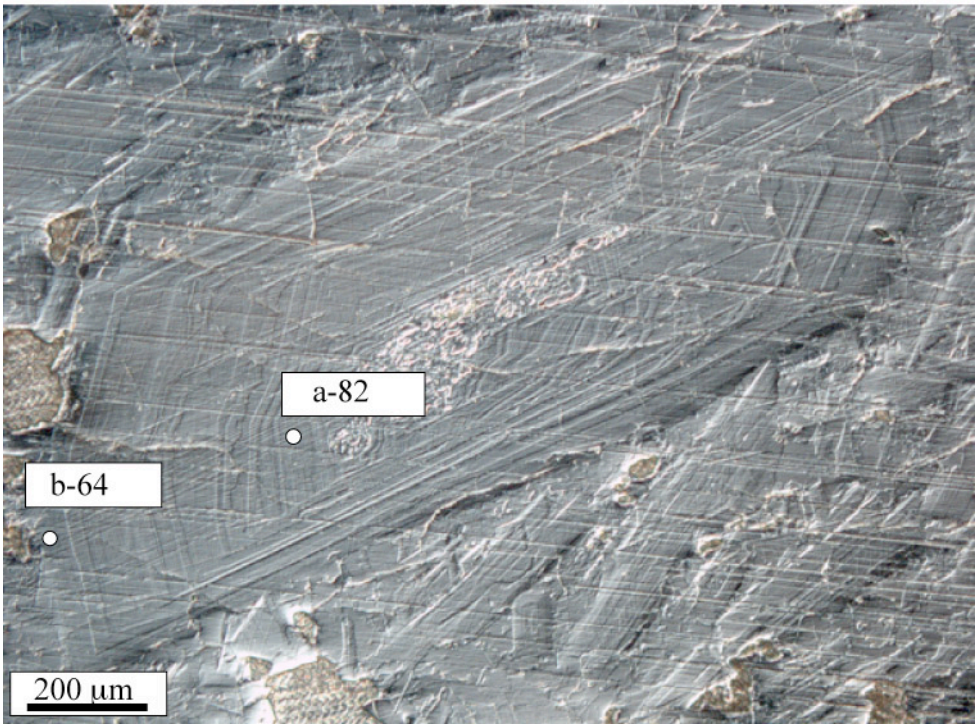

301-8

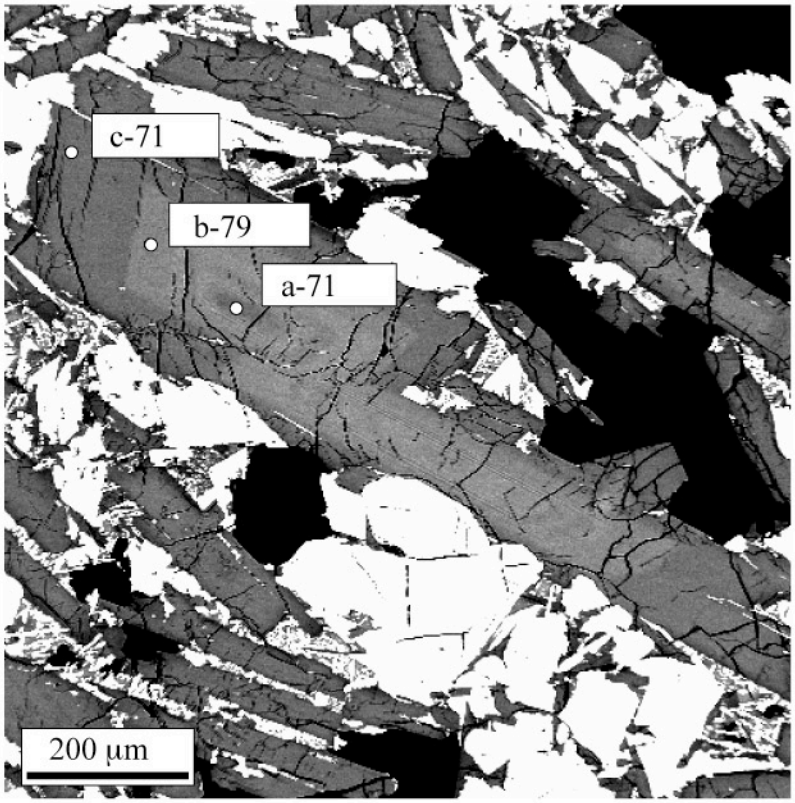

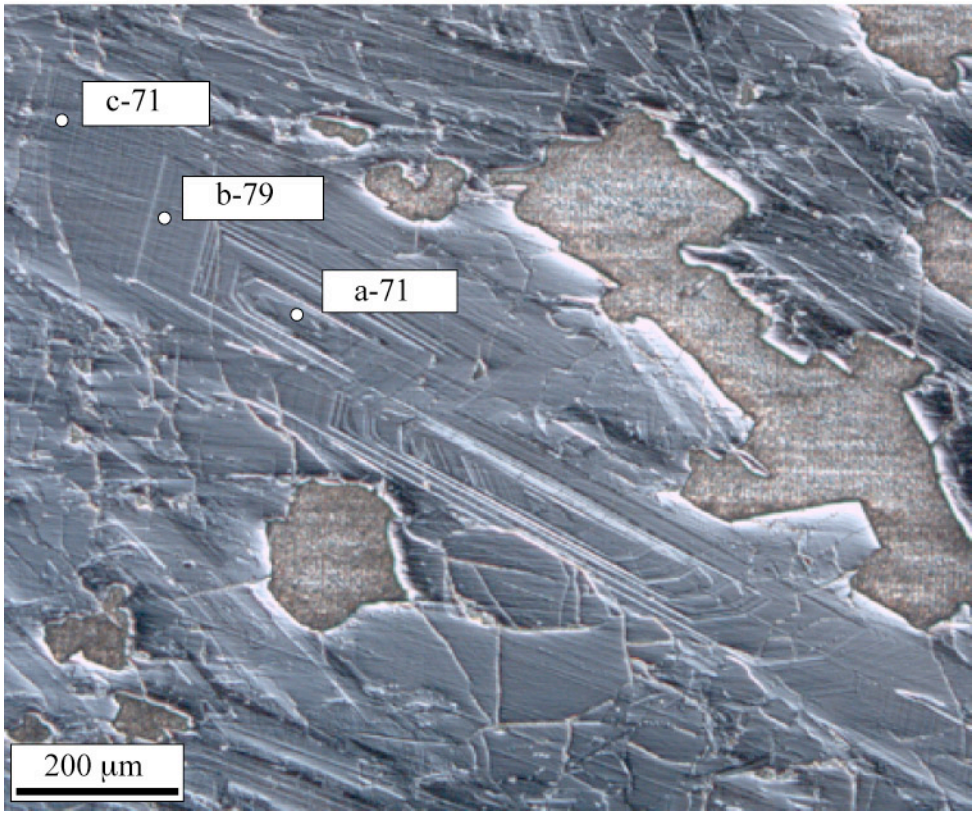

301-10

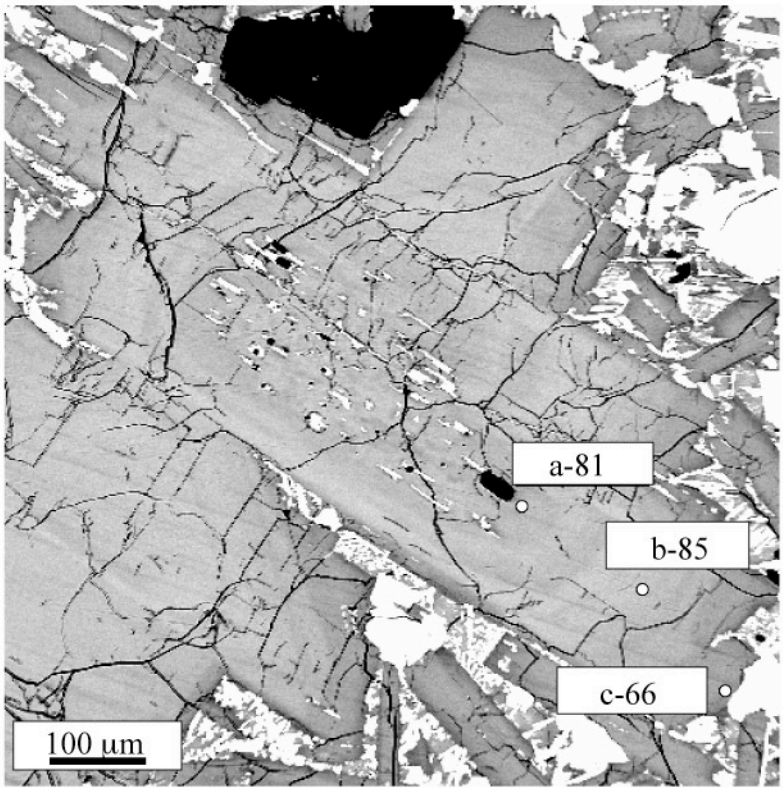

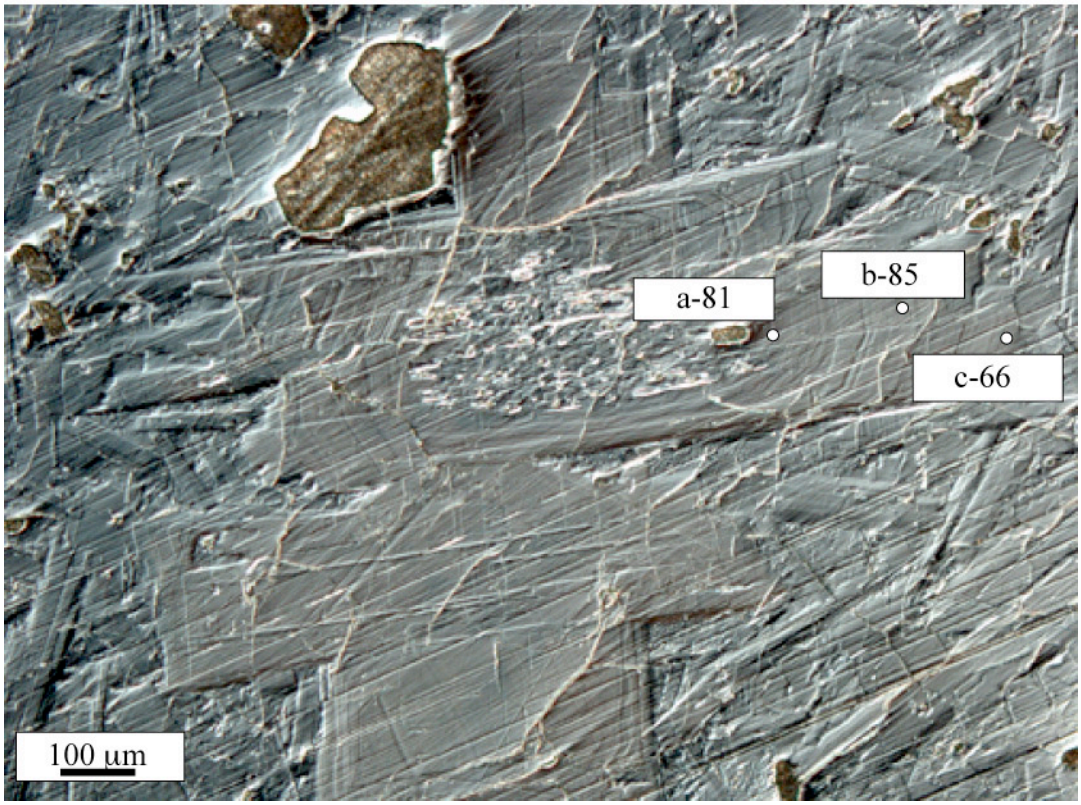

301-11, 301-gm

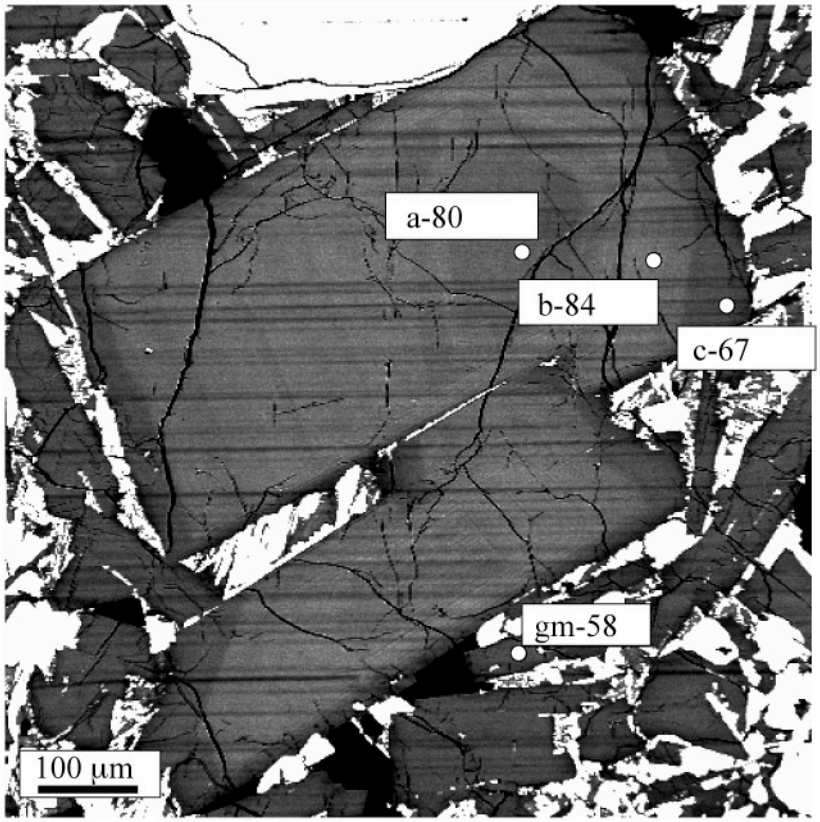

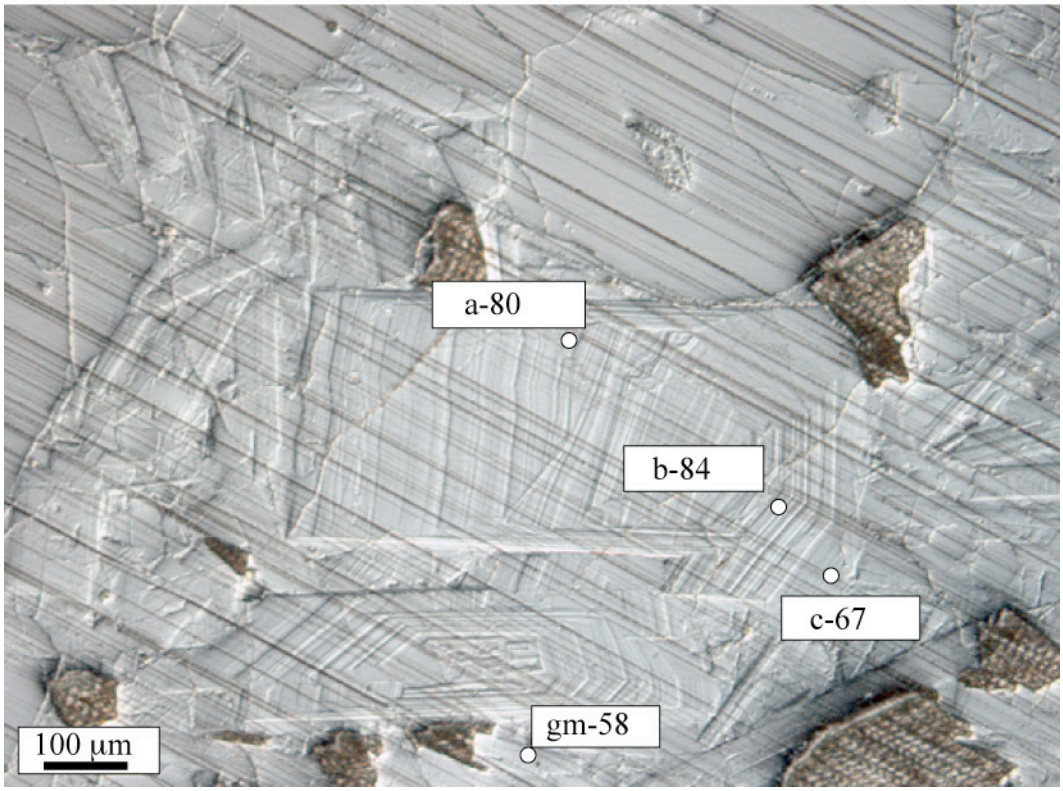

Appendix C

BSE and NDIC Images of Plagioclase in Sample SC98-271 with Approximate Microprobe spot locations. Upper image is BSE, lower image is NDIC.

271-1

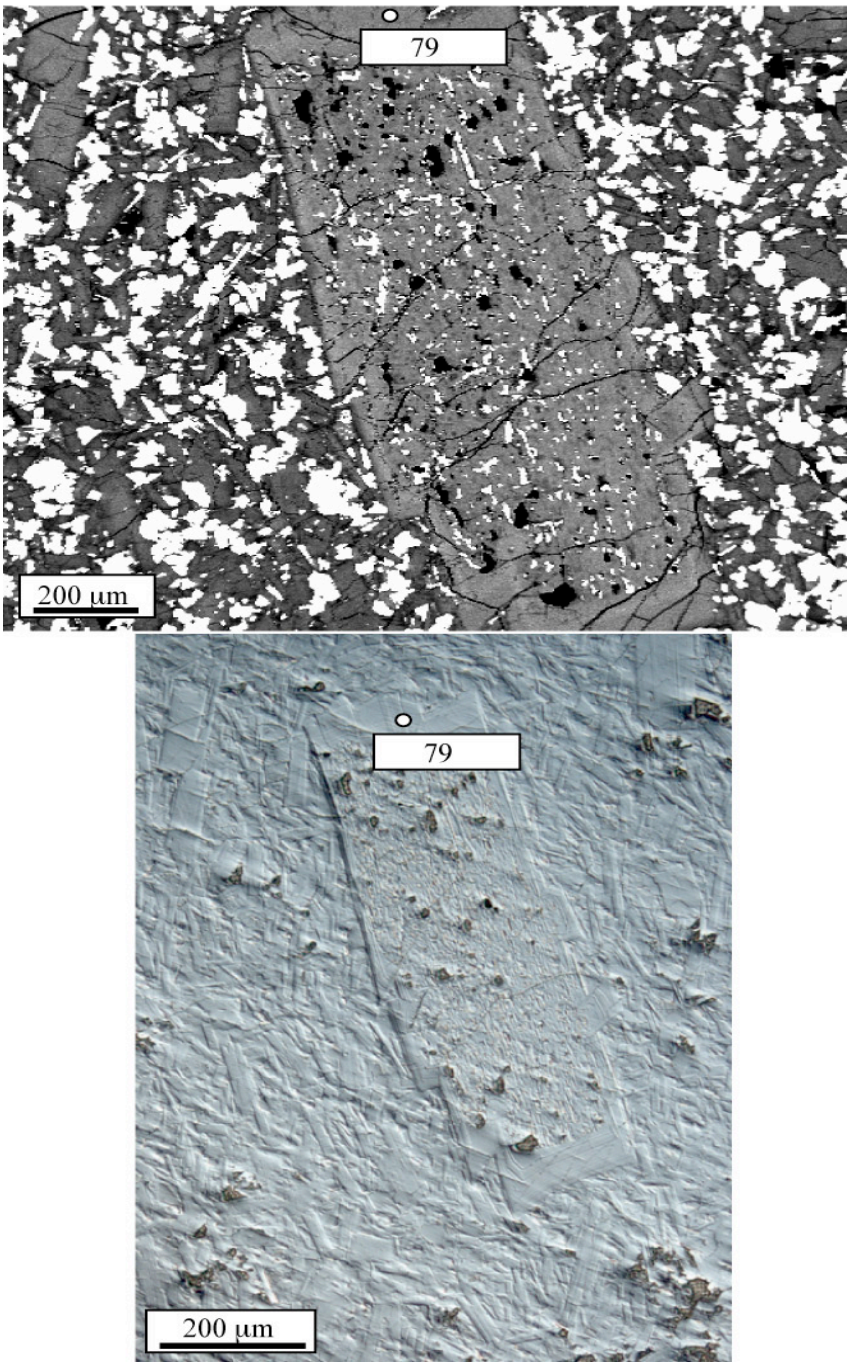

271-3

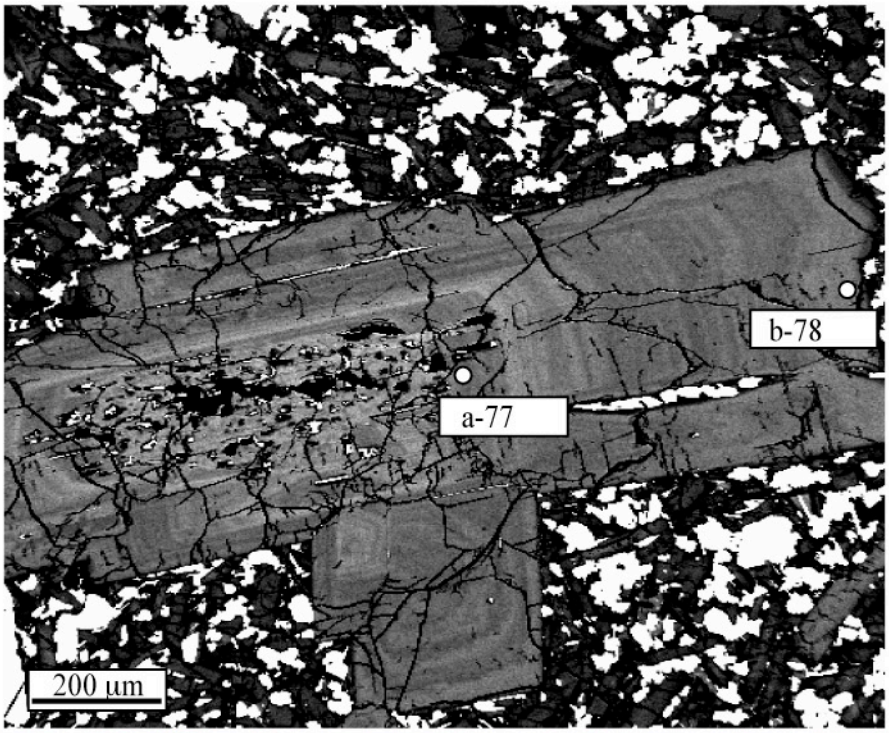

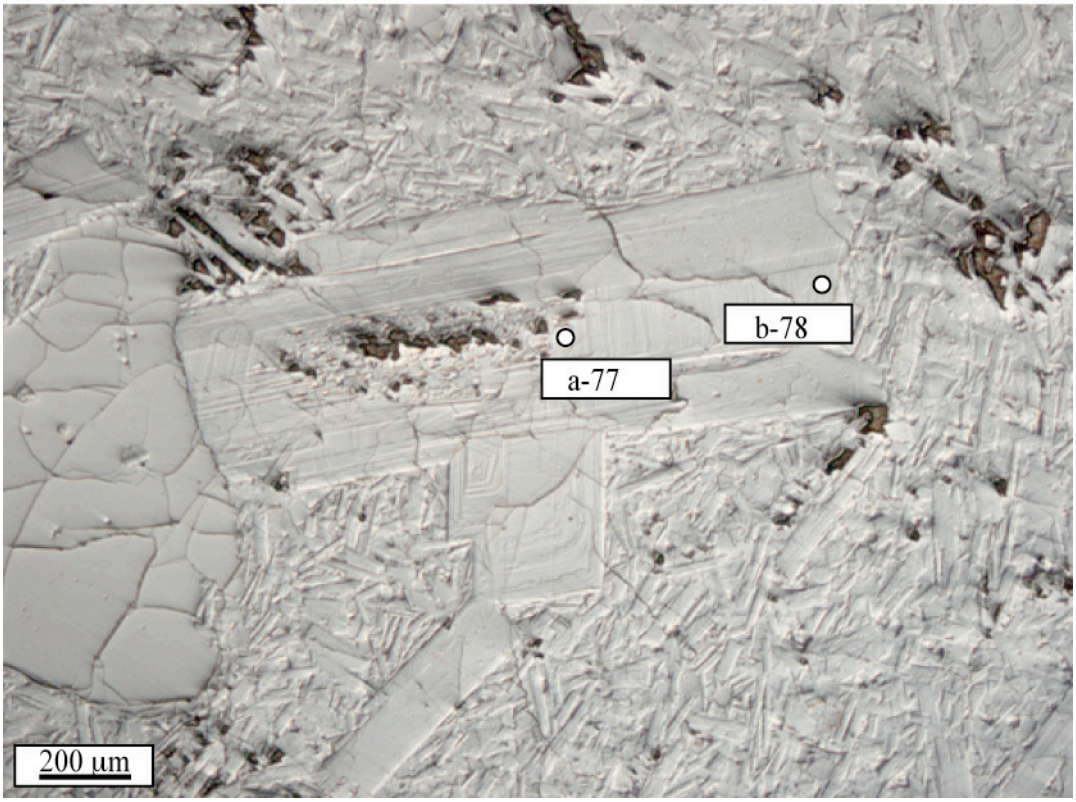

271-5

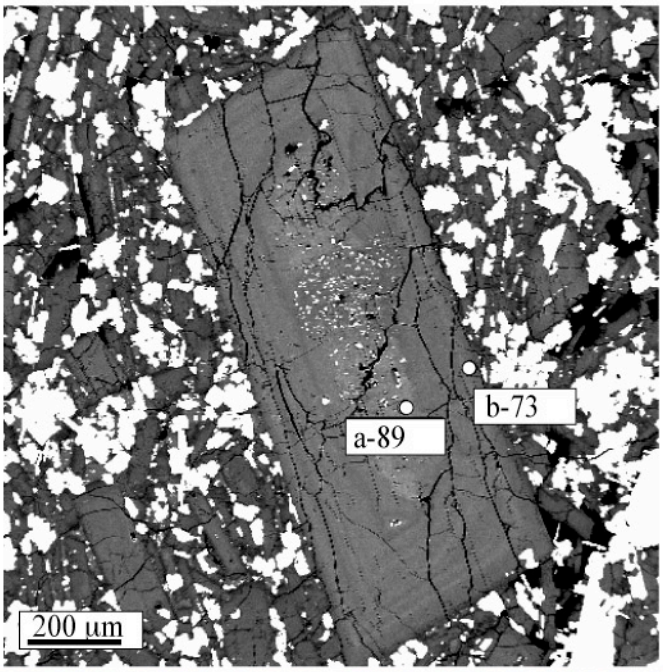

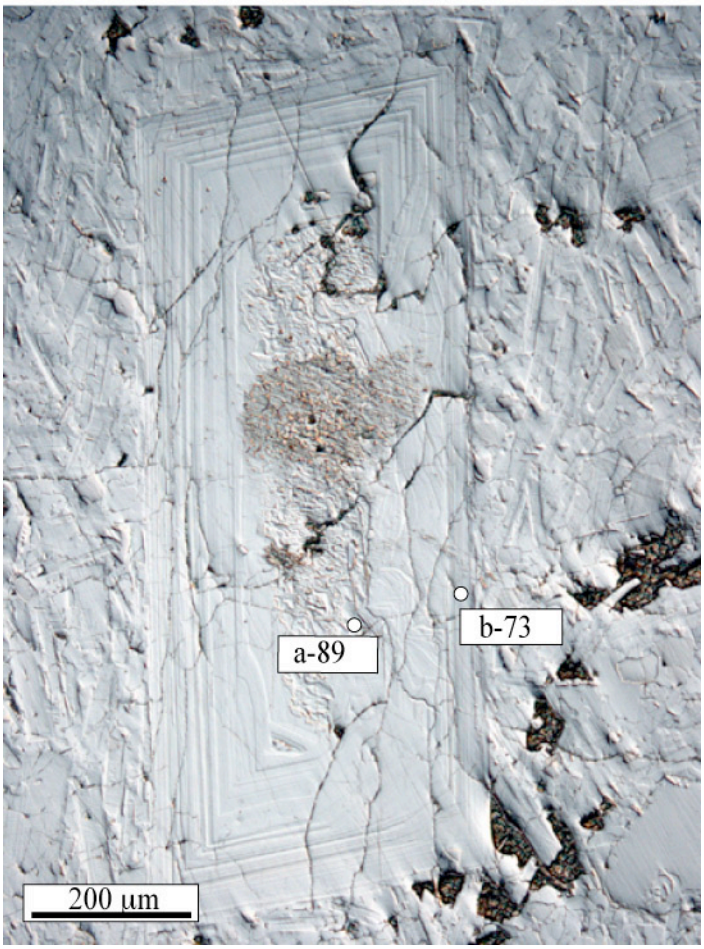

271-6

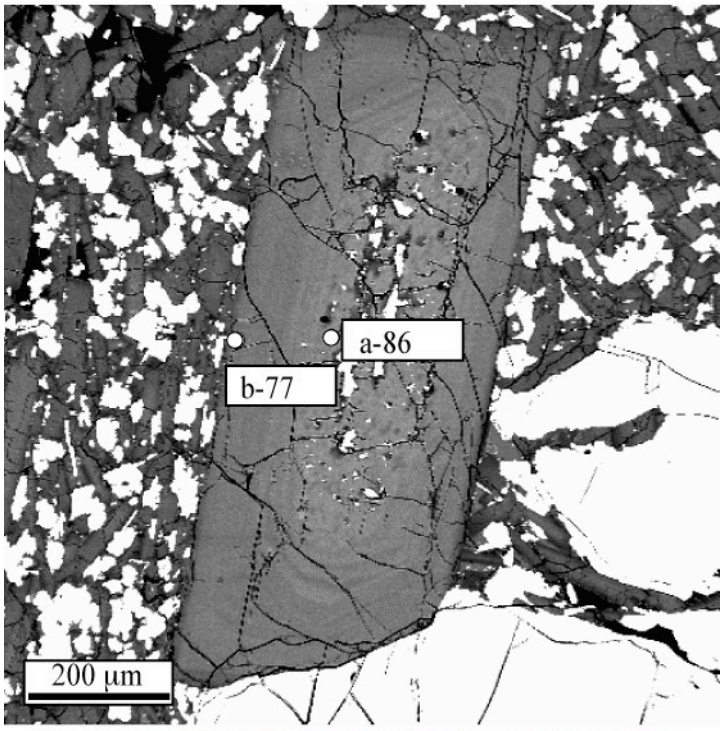

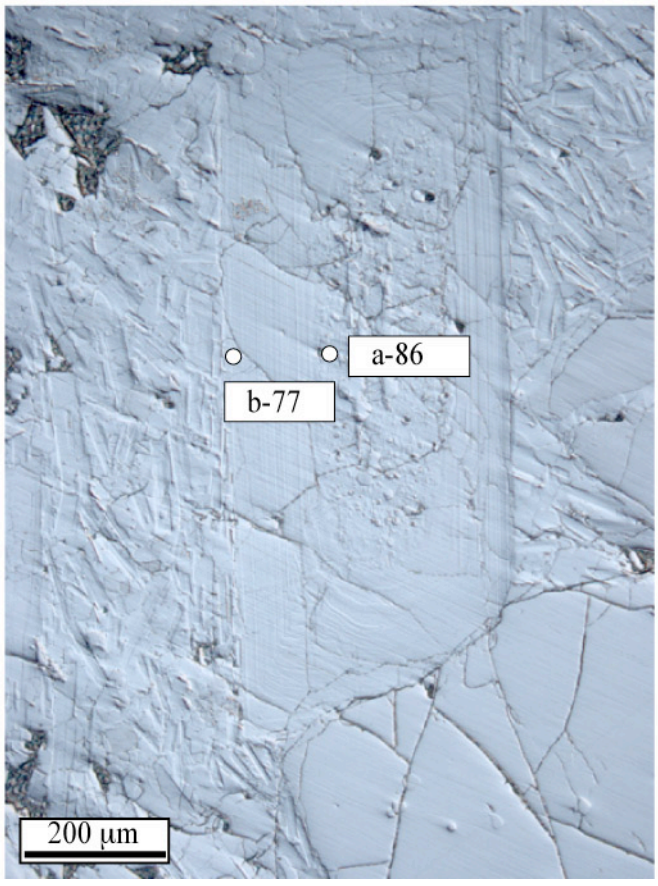

271-10

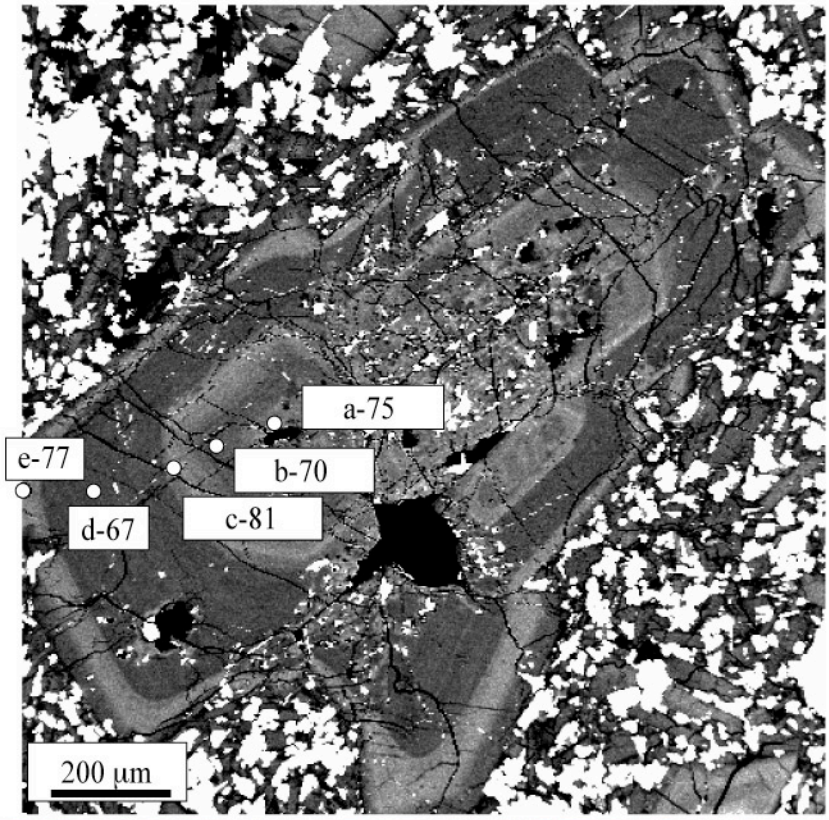

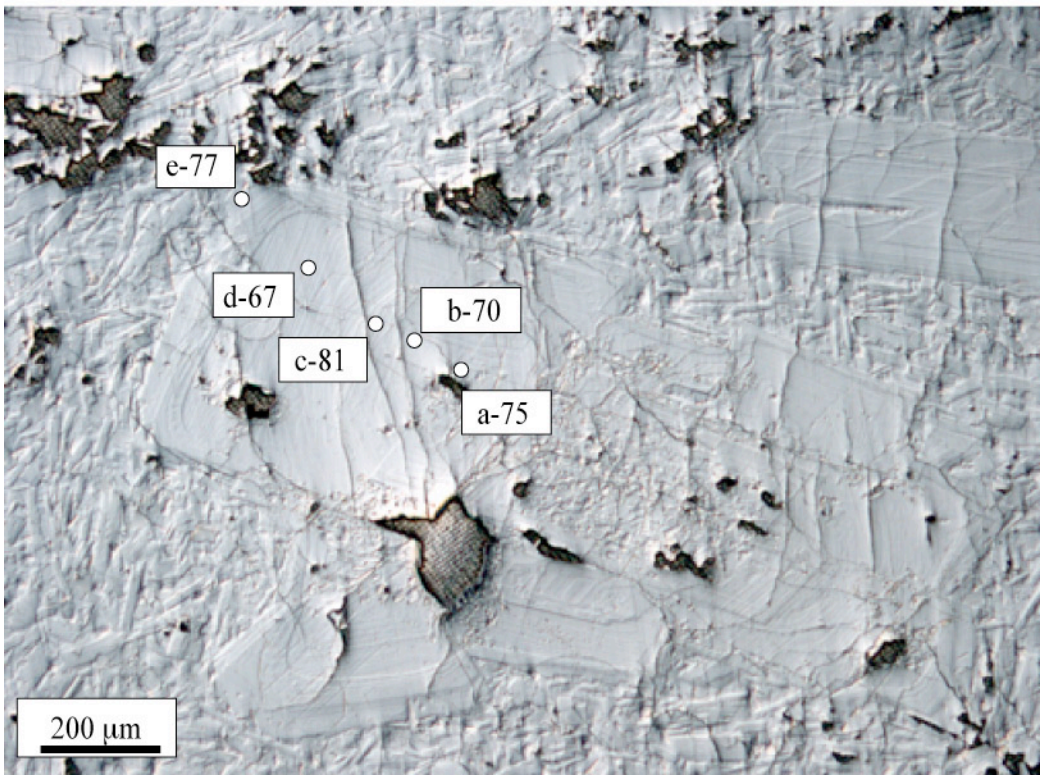

271-15

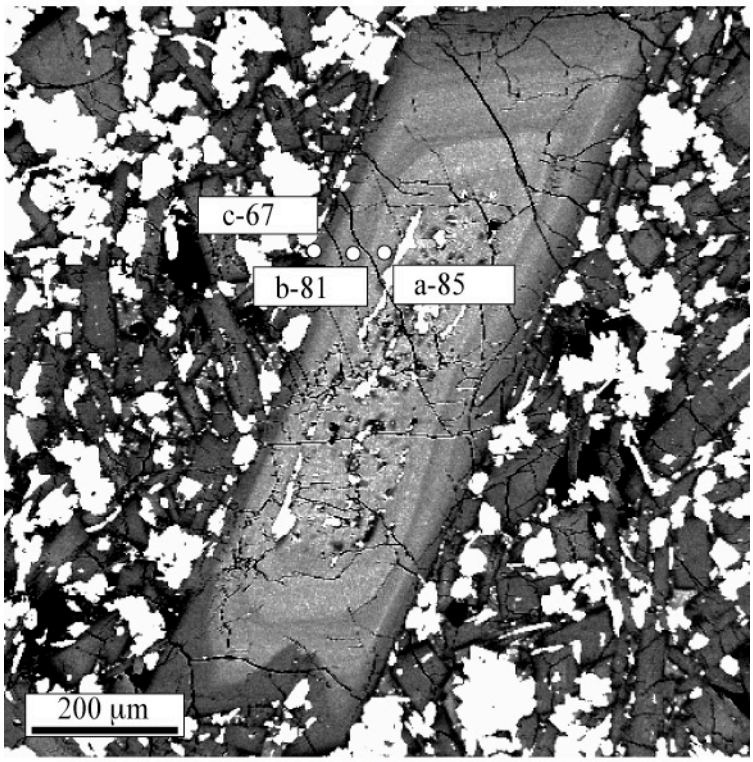

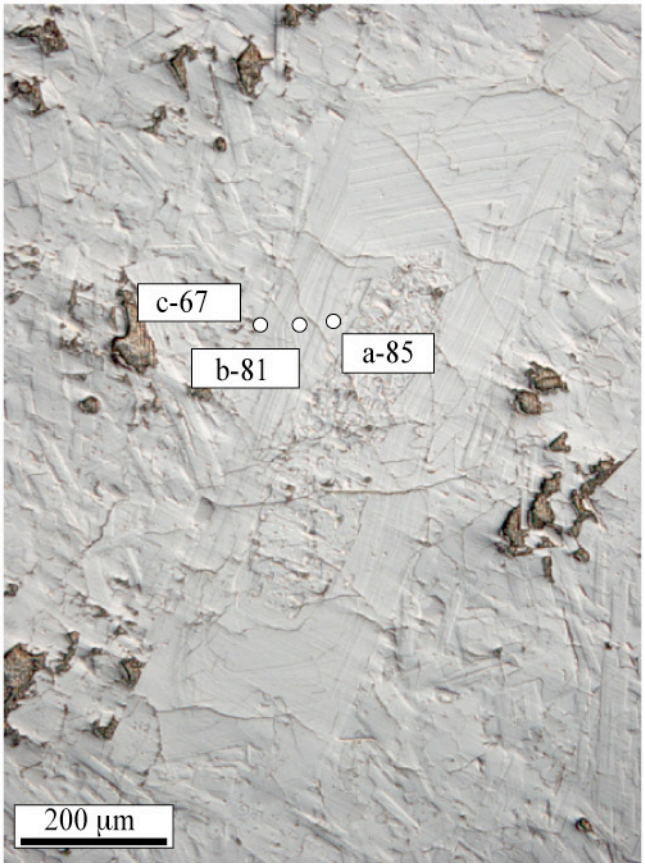

271-16

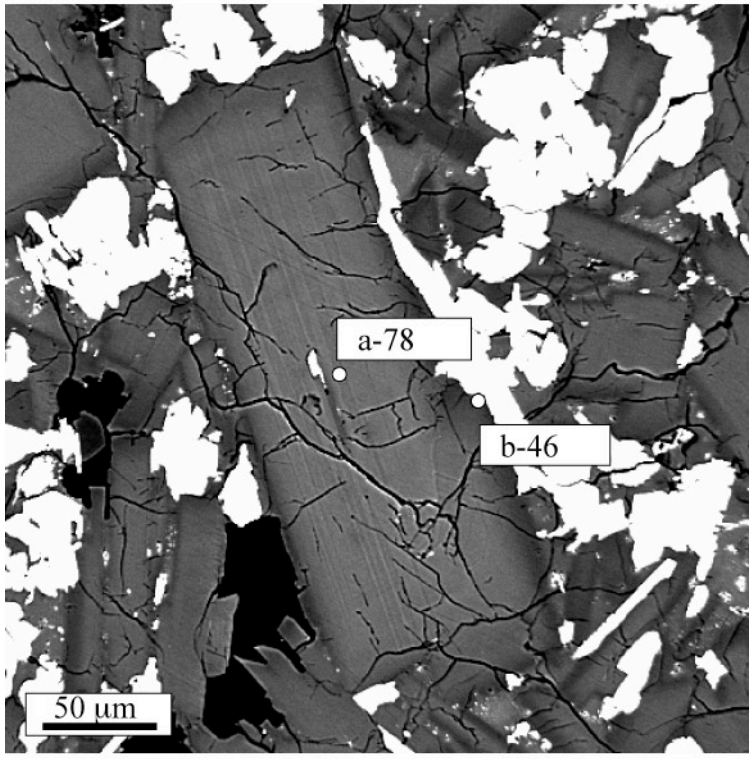

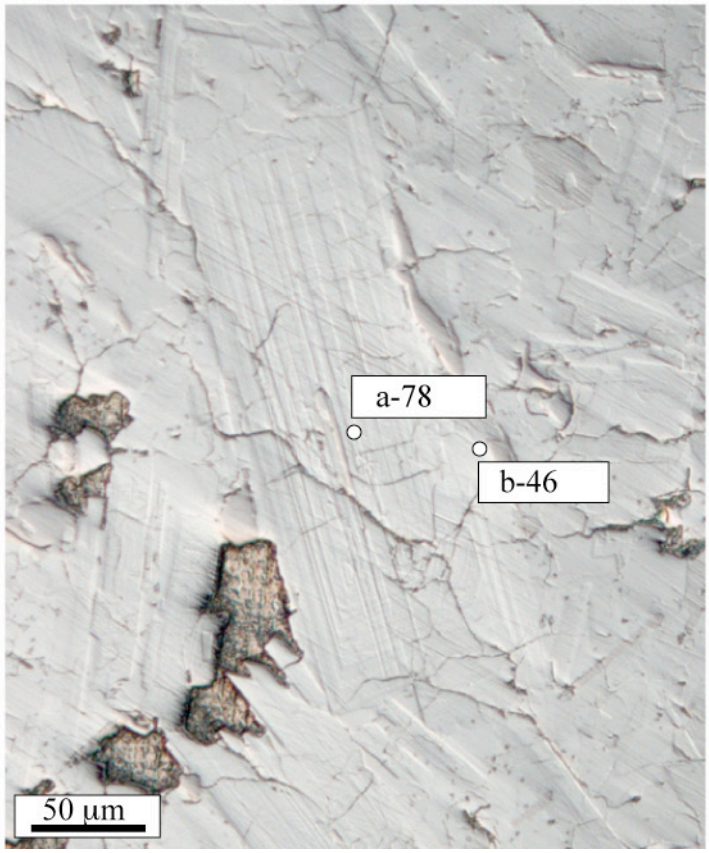

Appendix D

BSE and NDIC Images of Plagioclase in Sample W95-60B with Approximate Microprobe spot locations. Upper image is BSE, lower image is NDIC.

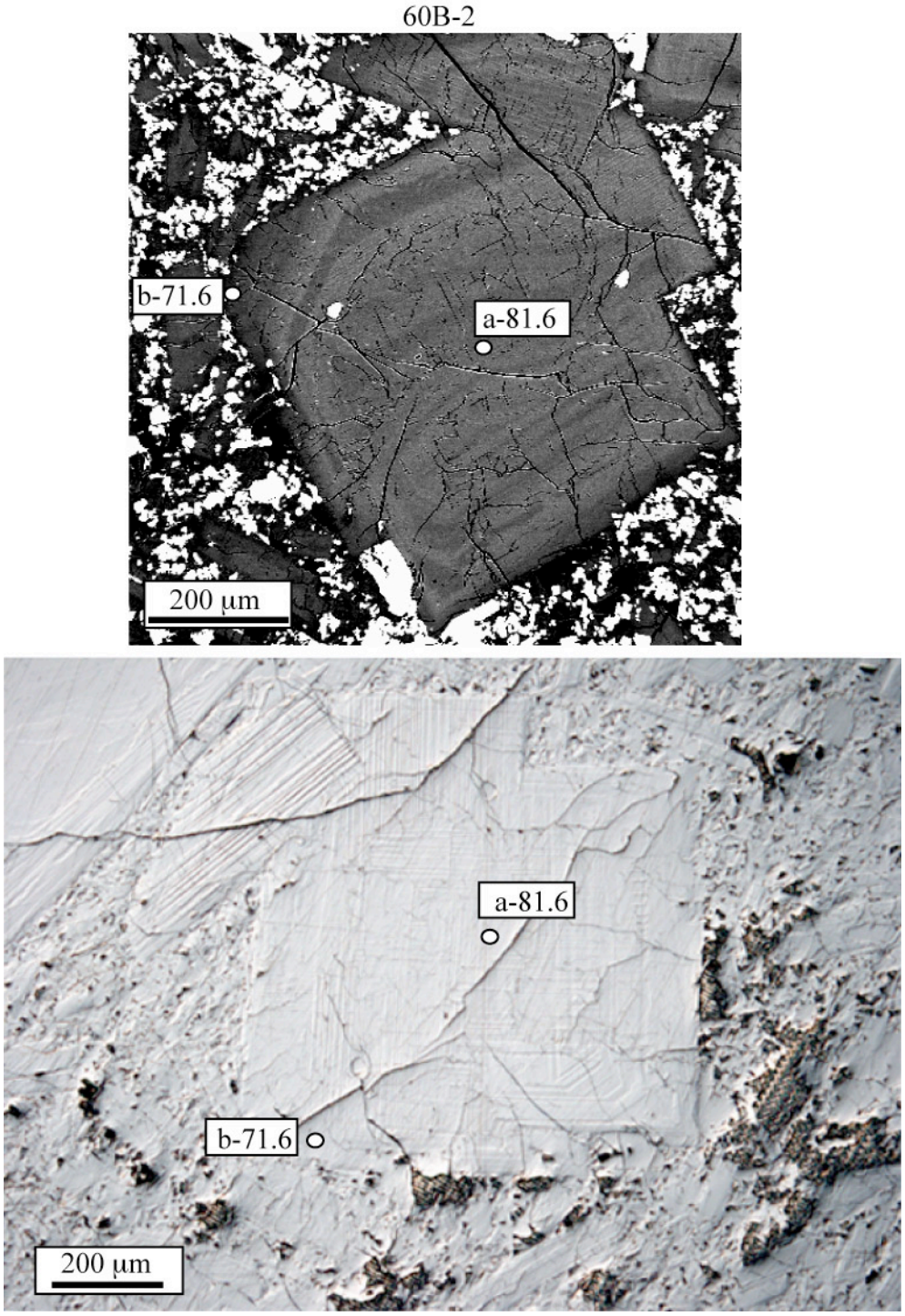

60B-4

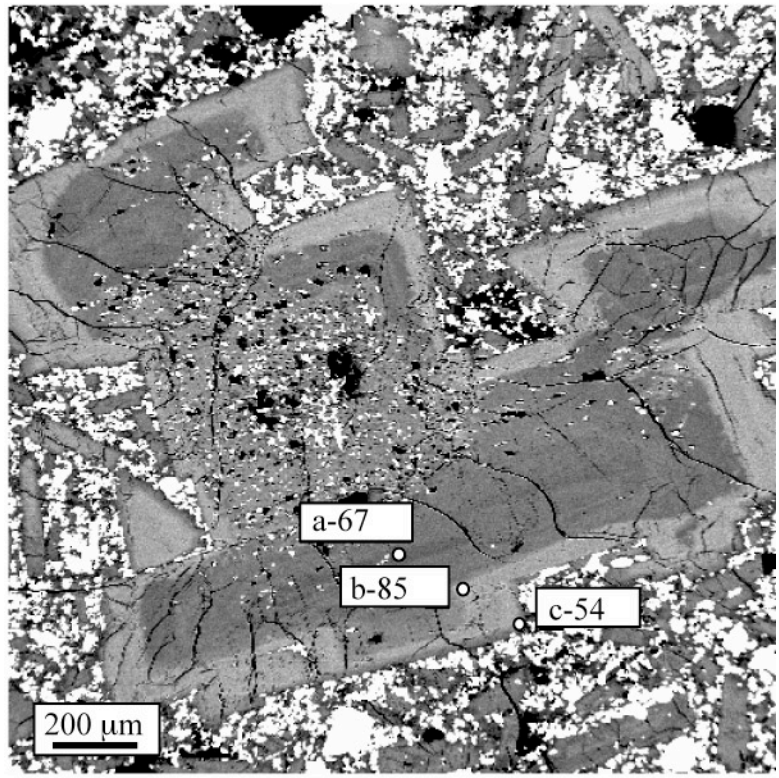

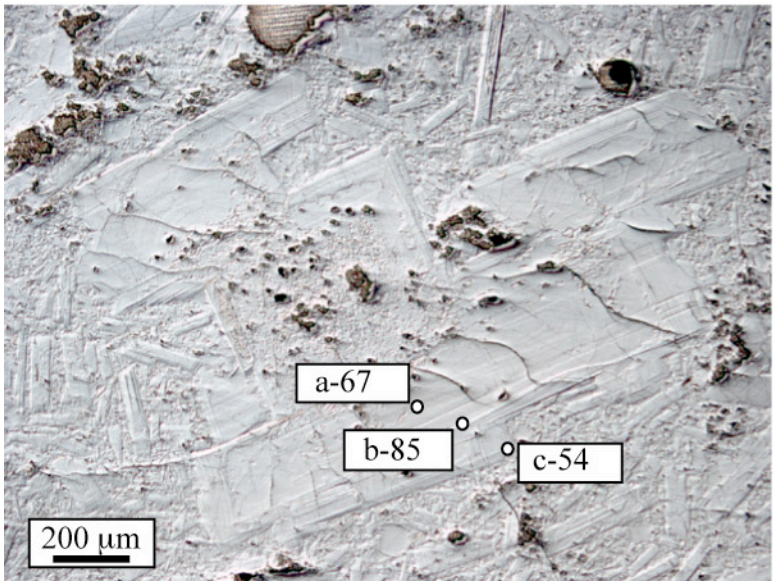

60B-6, 60B-gm

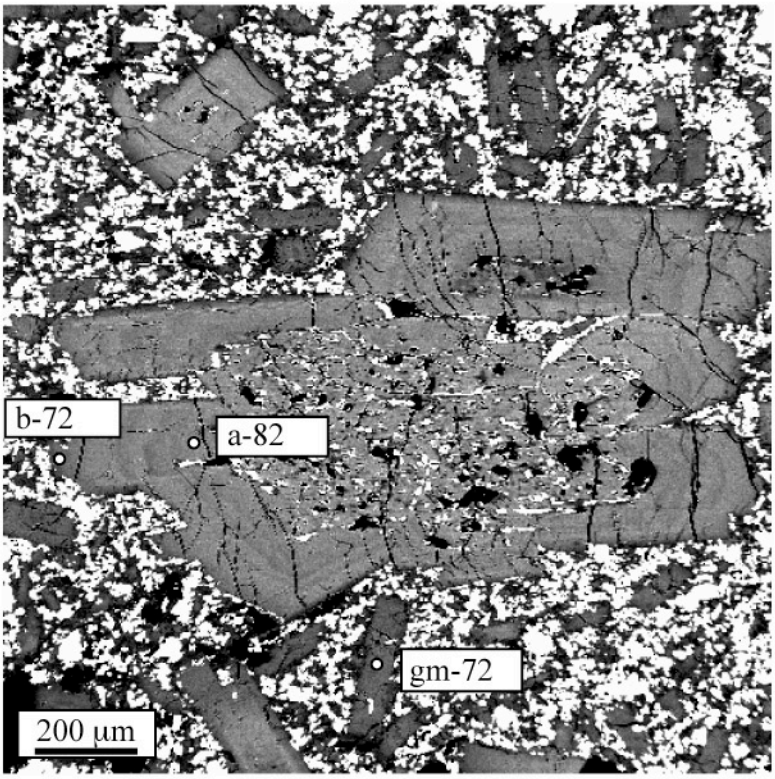

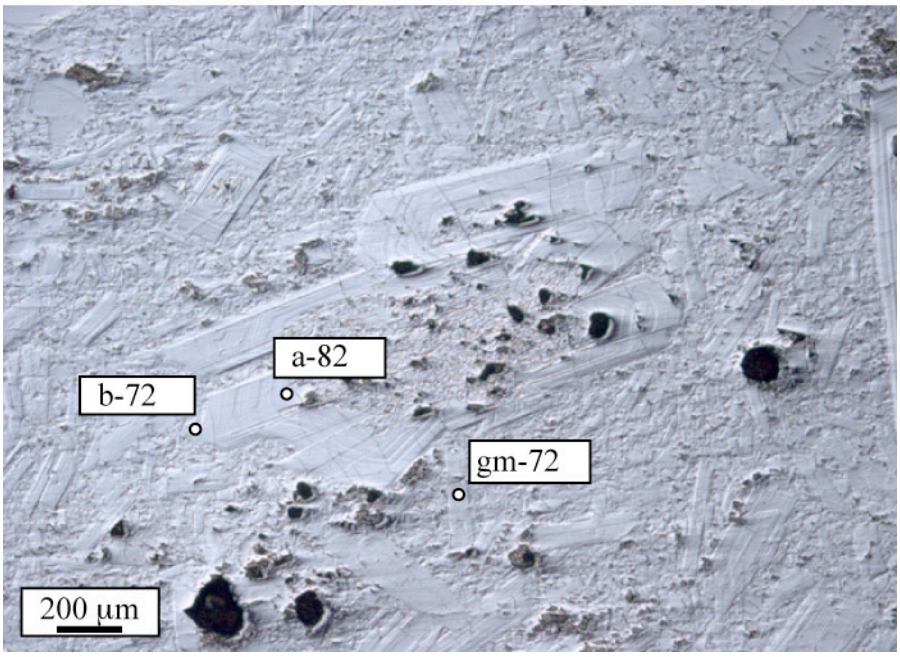

60B-10

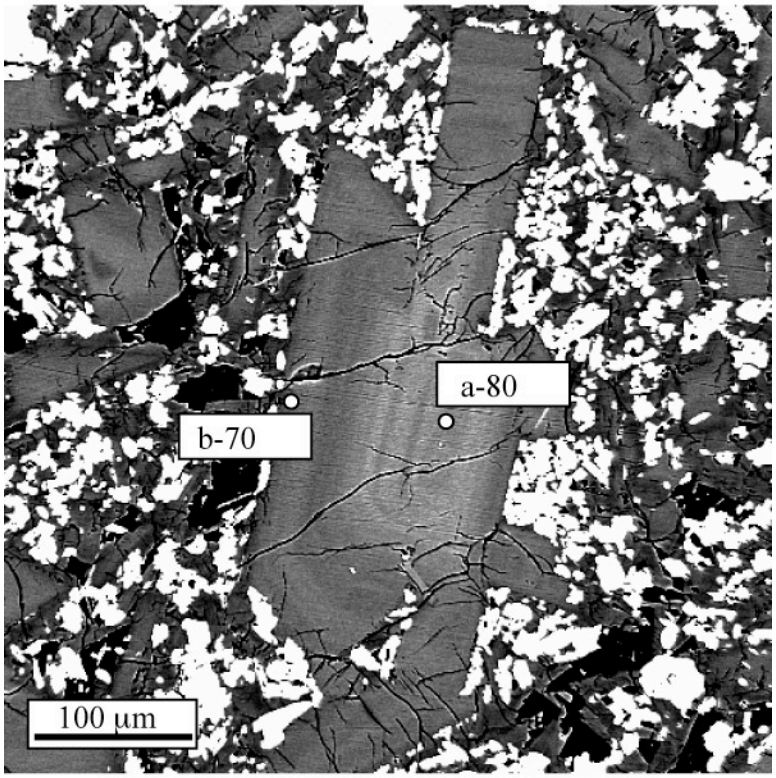

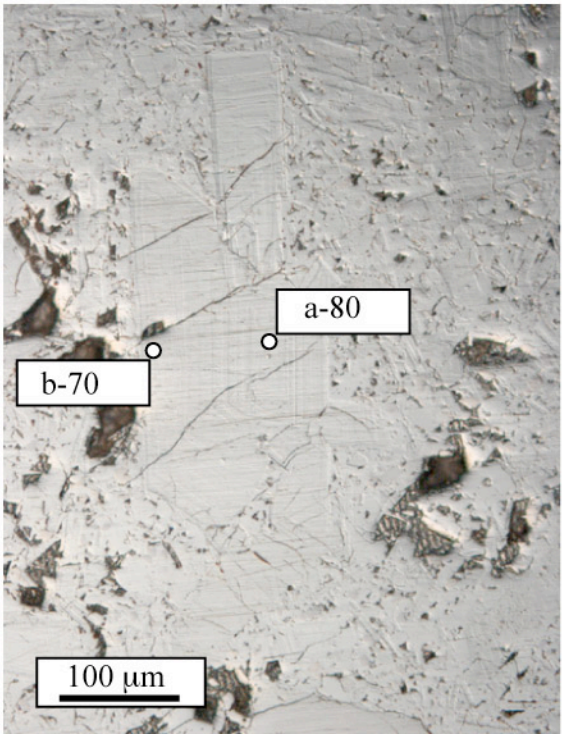

60B-12

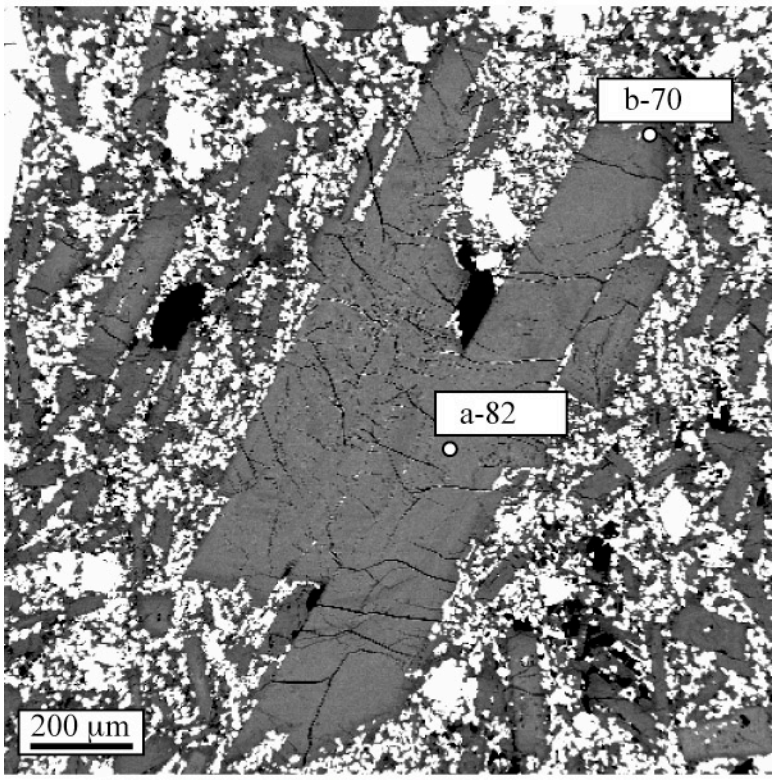

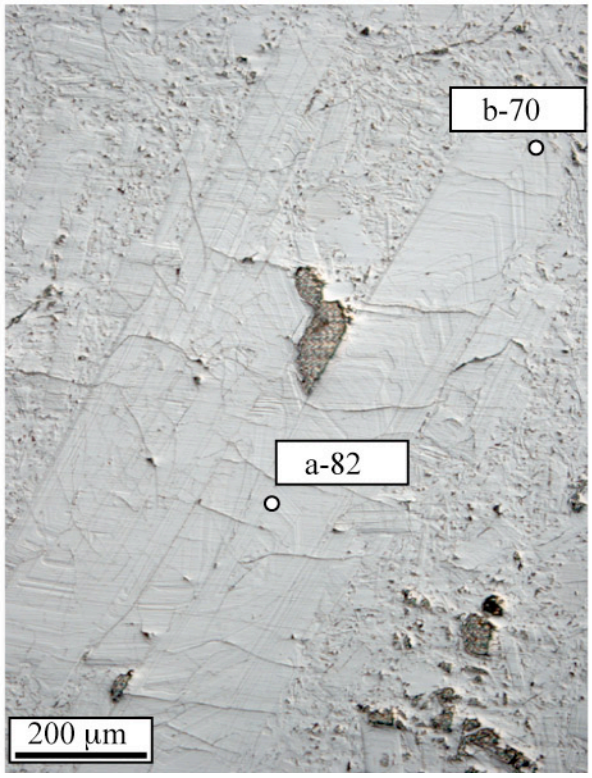

60B-13

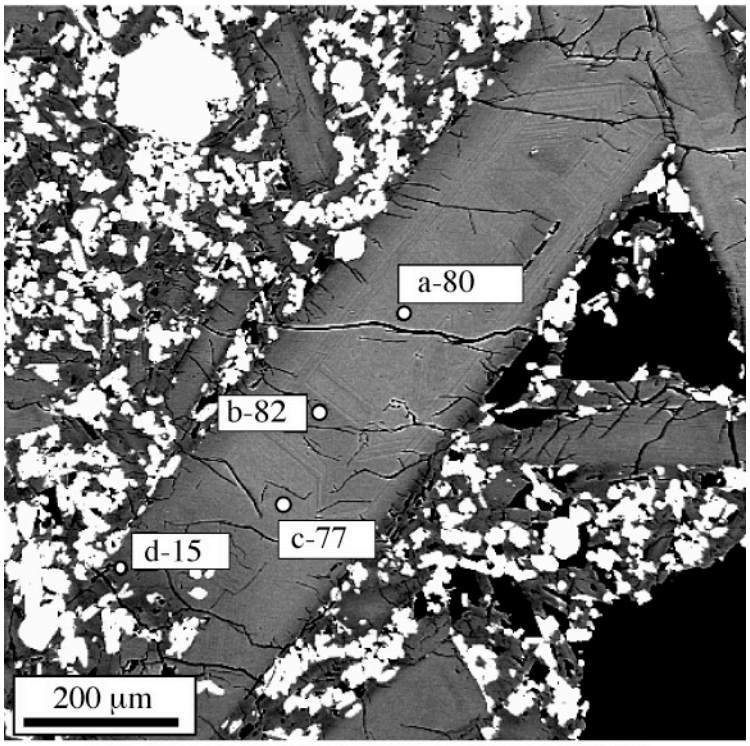

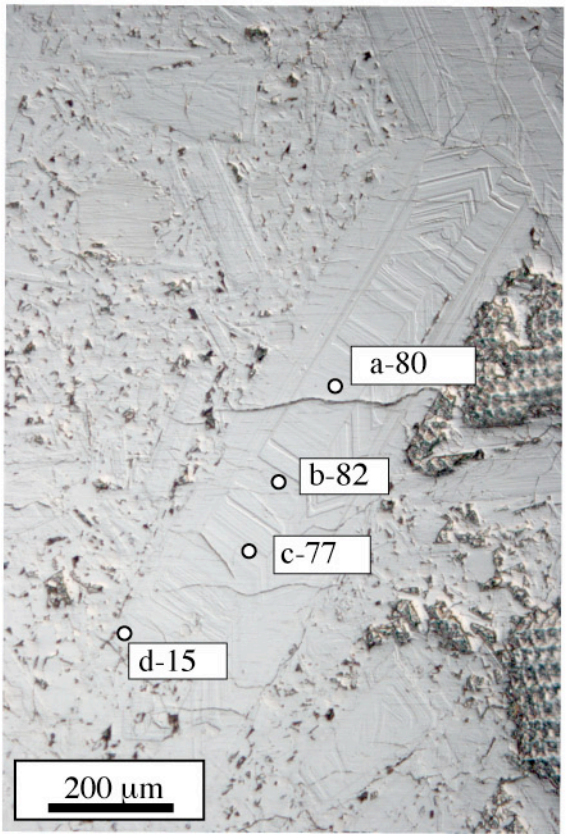

60B-14

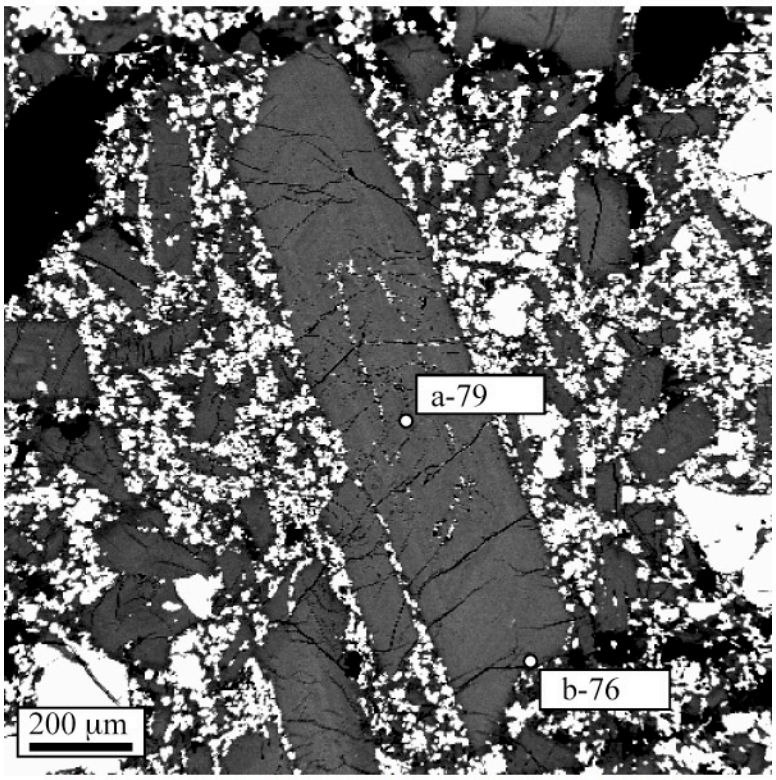

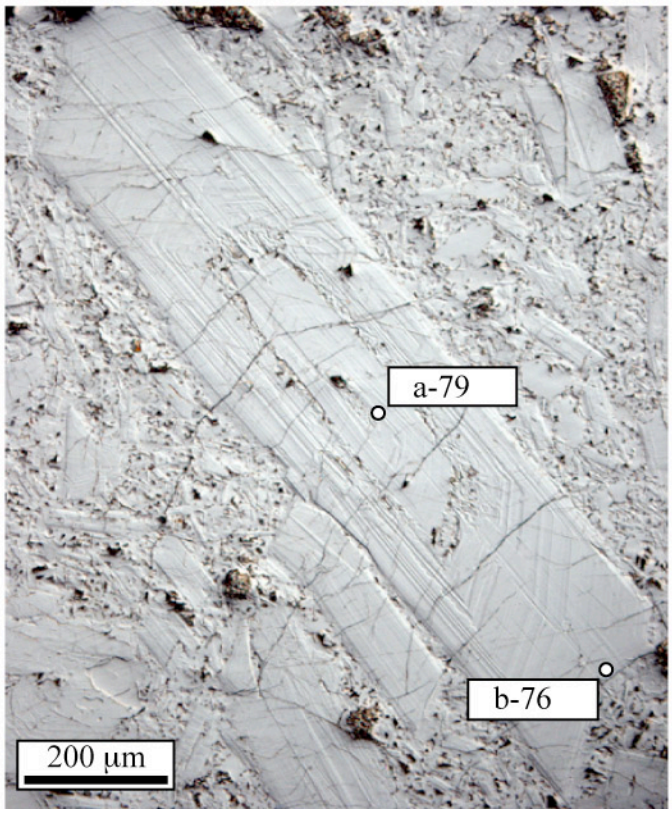

60B-16

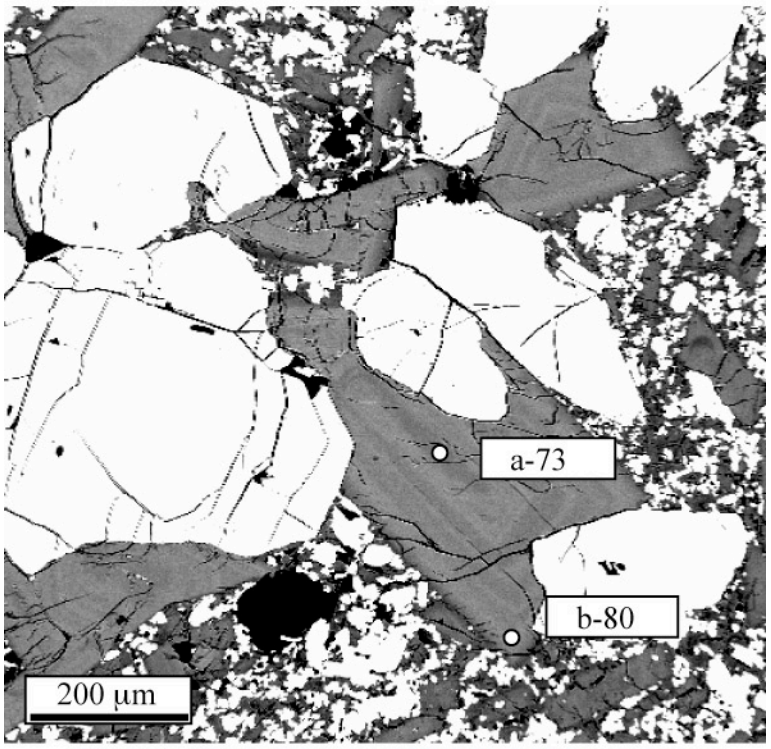

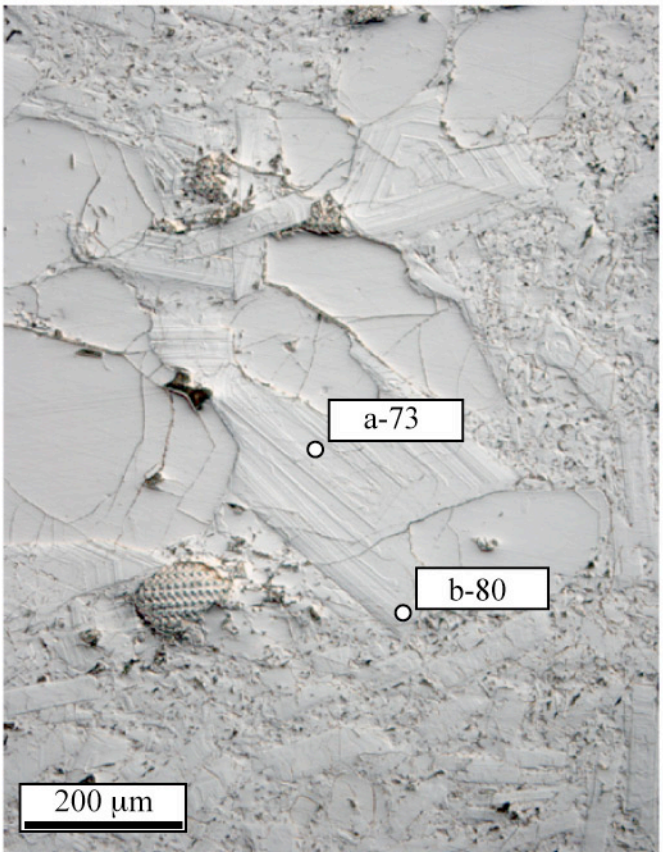

Appendix E

BSE and NDIC Images of Plagioclase in Sample SC02-527 with Approximate Microprobe spot locations. Upper image is BSE, lower image is NDIC.

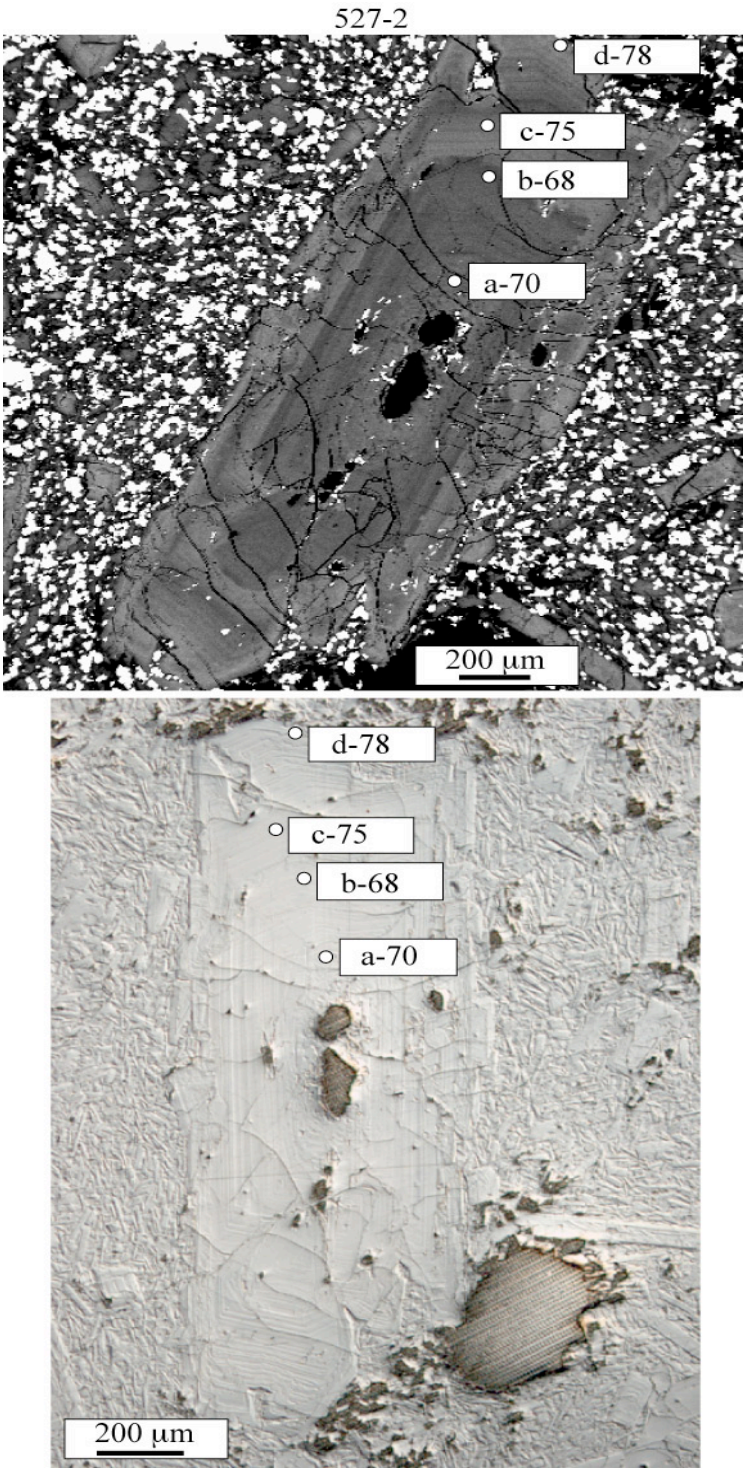

527-9

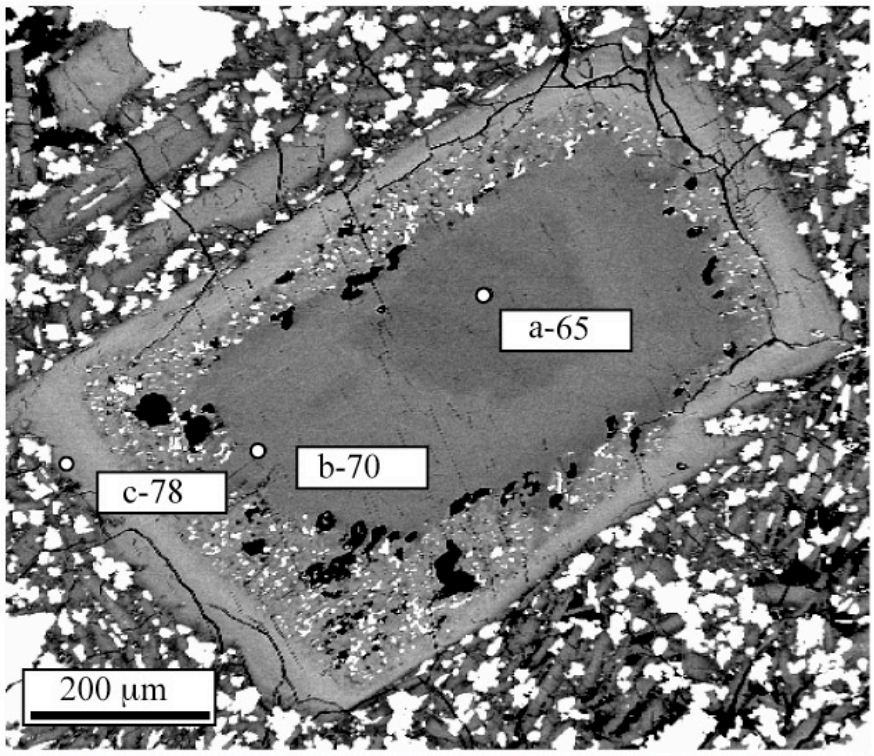

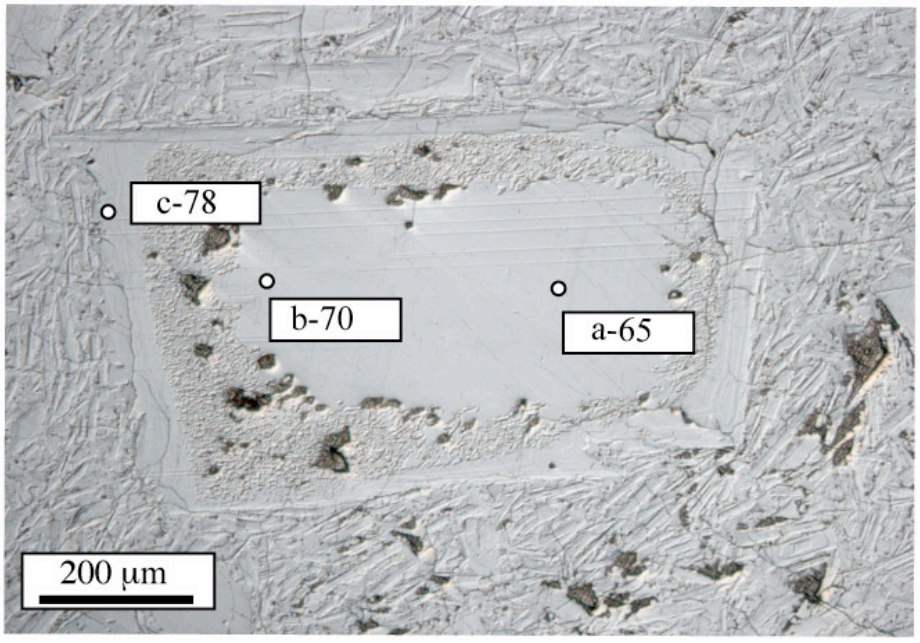

527-10

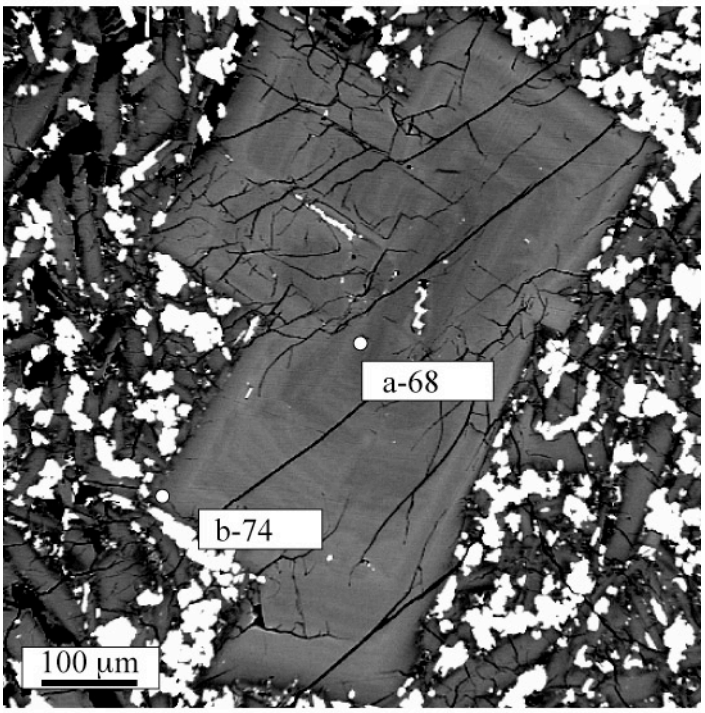

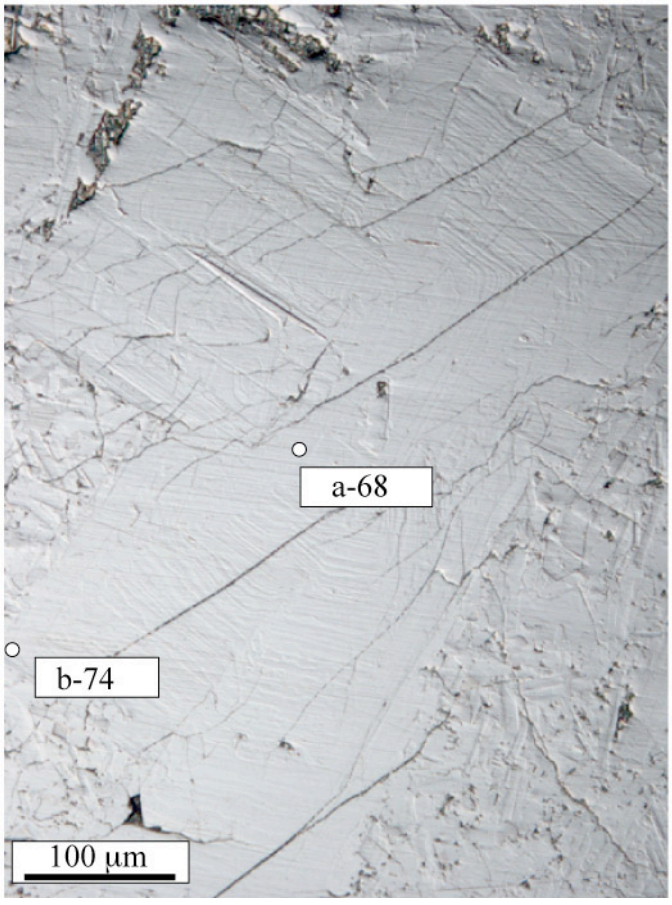

527-14

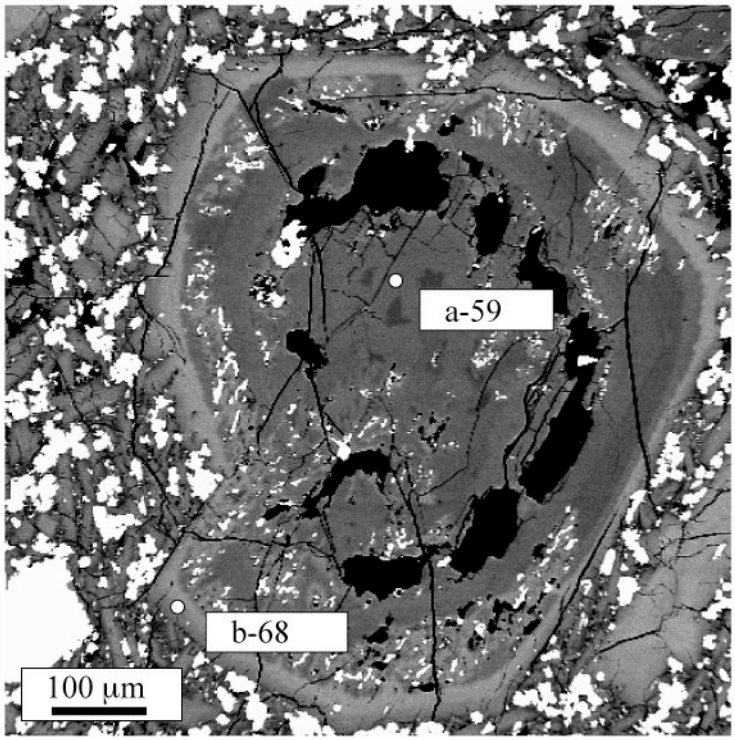

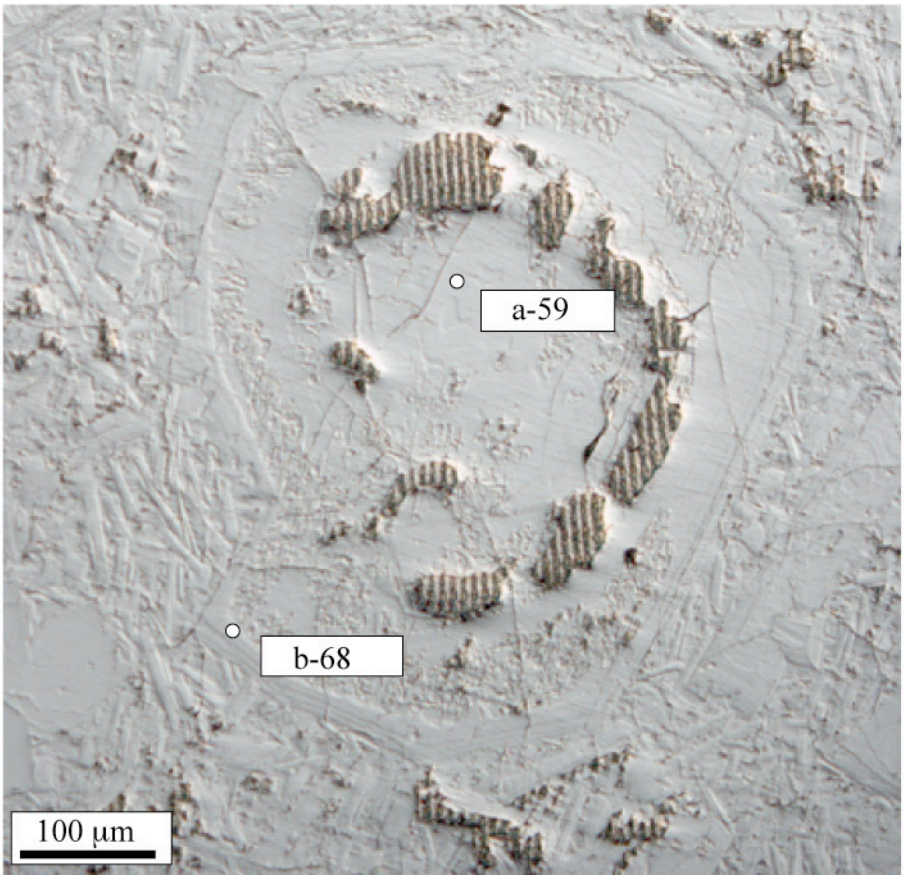

527-15

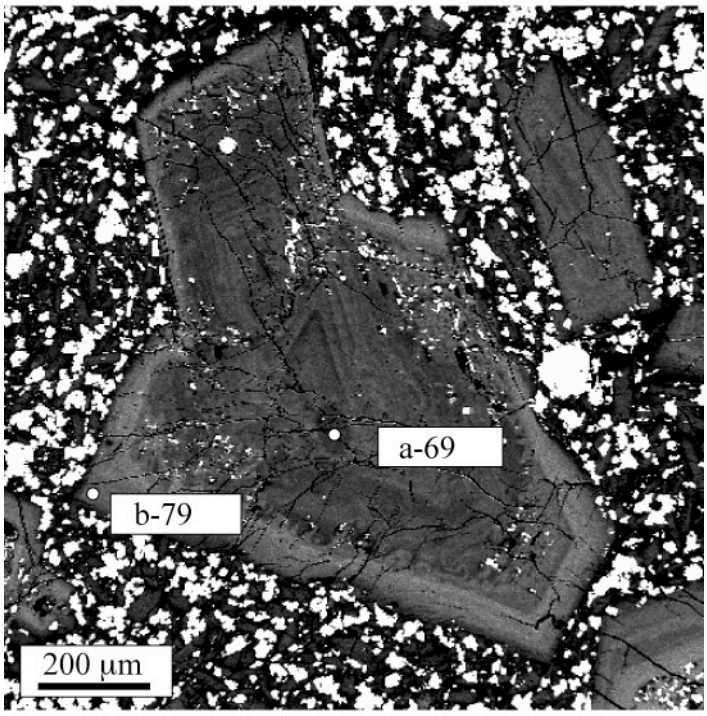

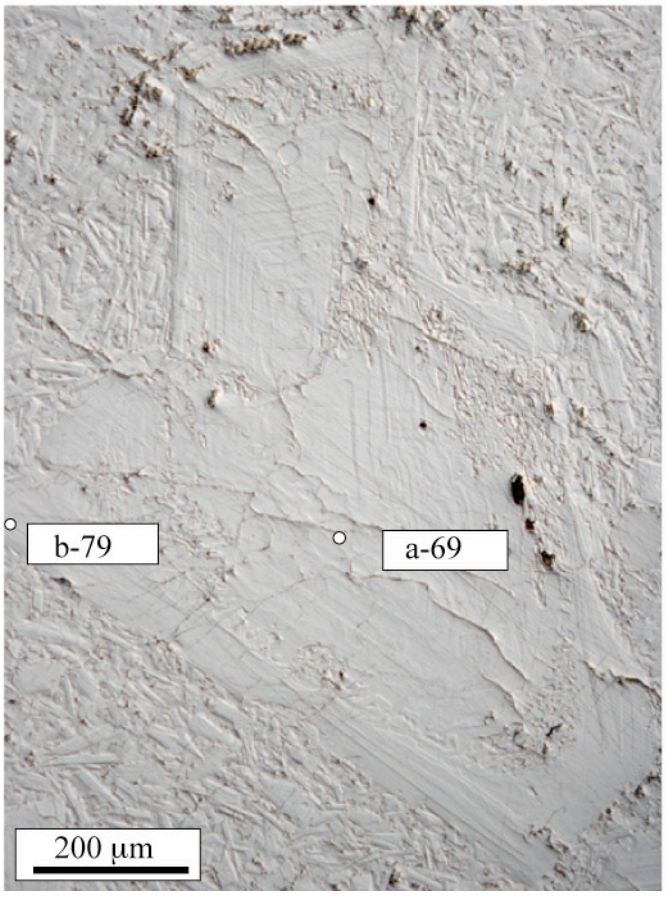

527-17, 527-18

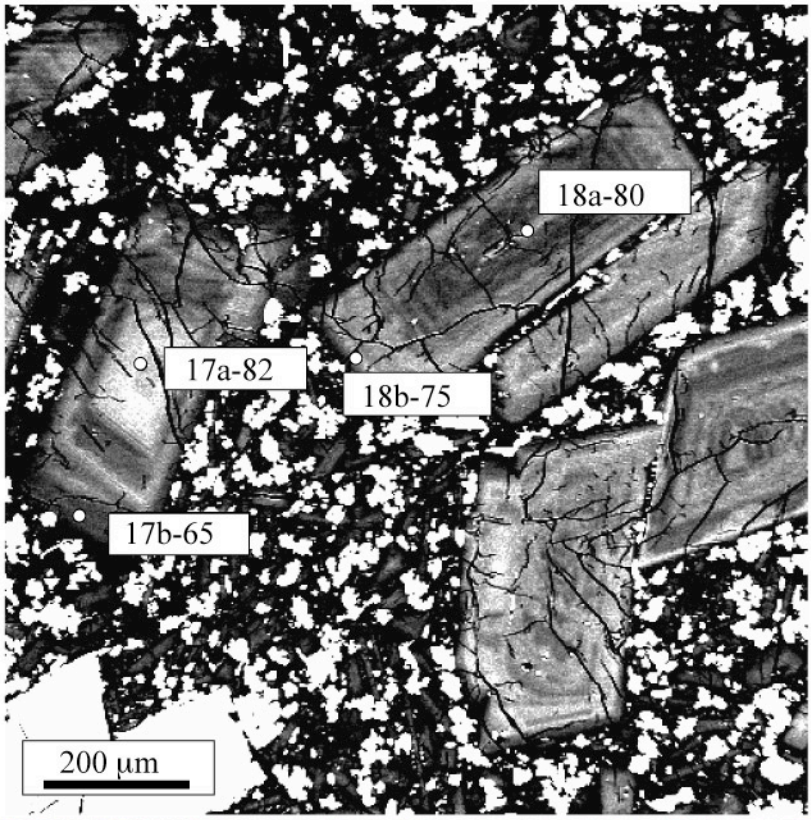
18a-80
17a-82
18b-75
17b-65
200 µm

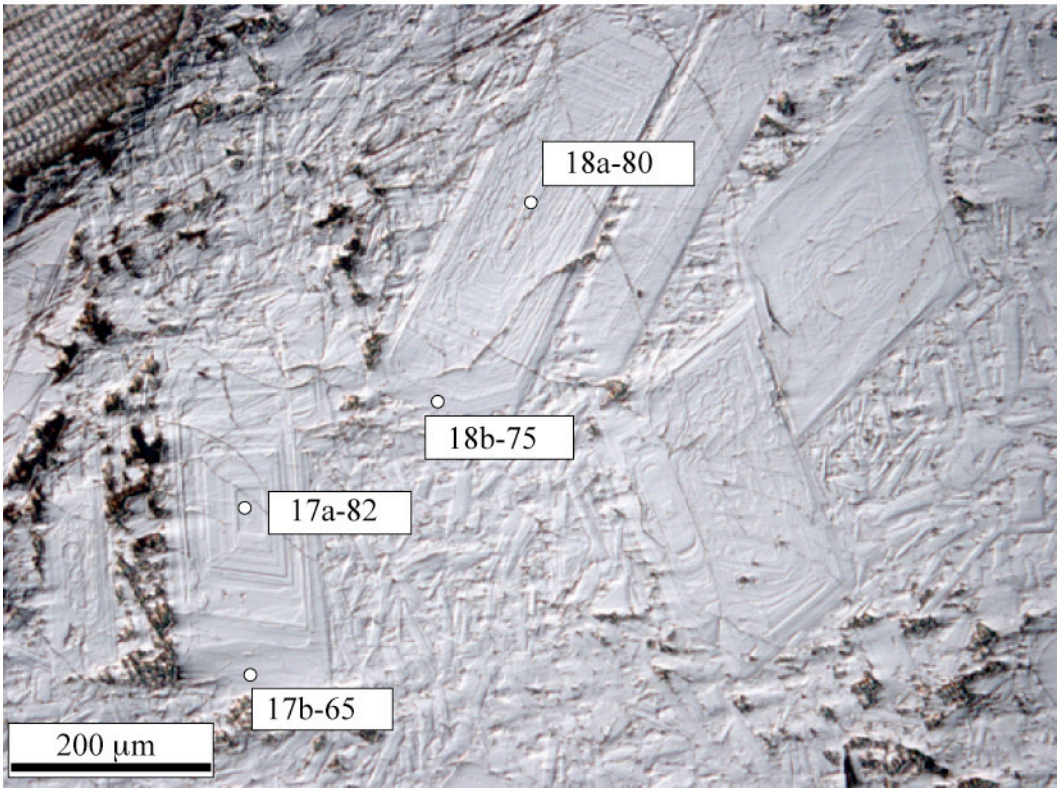
18a-80
18b-75
17a-82
17b-65
200 µm